POLITECNICO DI TORINO
Repository ISTITUZIONALE

Design of pilot channel tracking loop Systems for high sensitivity Galileo receivers

(Article begins on next page)

04 August 2020

taps EMLE detector with an EML chip spacing of 1 is an adequate PD as presented in Section 3.4.4.5, whereas a four taps VEMLE detector with an EML chip spacing of 0.5 and a Very Early Minus Late (VEML) chip spacing of 1 is used for Galileo E1 signals. As discussed in Section 3.4.4.4, the linear range of the 4 taps VEMLE discriminator using an early minus late chip spacing of 0.5 extends over $+/-0.5$ chips albeit with some undulations while the linear range of a simple EMLE discriminator using an early minus late chip spacing of unity extends over $+/-0.5$ chips.

3.5.3.5 Carrier and code tracking

Following the scheme of signal simulation described in Section 2.3.4, a carrier signal modulated by Galileo E1 and E5a OS signals is generated over 5 seconds with a CNR of 30 dB-Hz and a ramp Doppler frequency of -0.8 Hz/s rate and an initial value of 2 kHz. Subsequently, the simulated signal is fed into the carrier and code tracking loops made up by an ATAN2 carrier PD and an appropriate code PD, one of the aforementioned first order loop filters and a frequency NCO which is equivalent to a phase and rate NCO. The code PD is selected as either the standard EMLE PD for Galileo E5a or the 4 taps VEMLE PD as described in Section 3.4.4.4 for the Galileo E1 signal. No loop gain compensation is implemented.

As for the individual carrier tracking case, an initial frequency error of 3 Hz is set for the range of considered B_L values. Similarly, an initial code phase error of a few samples and an almost zero initial code rate error is applied while testing all PDI values. Again, the carrier and code tracking loops are governed by the Nyquist sampling bound $B_N < 1/(2T_I)$ as explained in Section 3.4.2.1. Subsequently, the noise equivalent bandwidth design parameter in the code tracking loop has been set to $B_N = 5$ Hz in general, with the exception of $T_I = 60$ ms case where $B_N = 3.33$ Hz to yield $B_L = 0.2$ one of the considered values in the theoretical analysis put forth in Sections 3.5.3.1 and 3.5.3.2. Conversely, the noise equivalent bandwidth design parameter in the carrier tracking loop has been bounded with the increase of the integration interval, such that $B_N = 10$ Hz is chosen for integration intervals less than 40 ms. On the other hand, PDI values of 60 80 and 100 ms were used with a $B_N = 8$, 6 and 5 Hz.
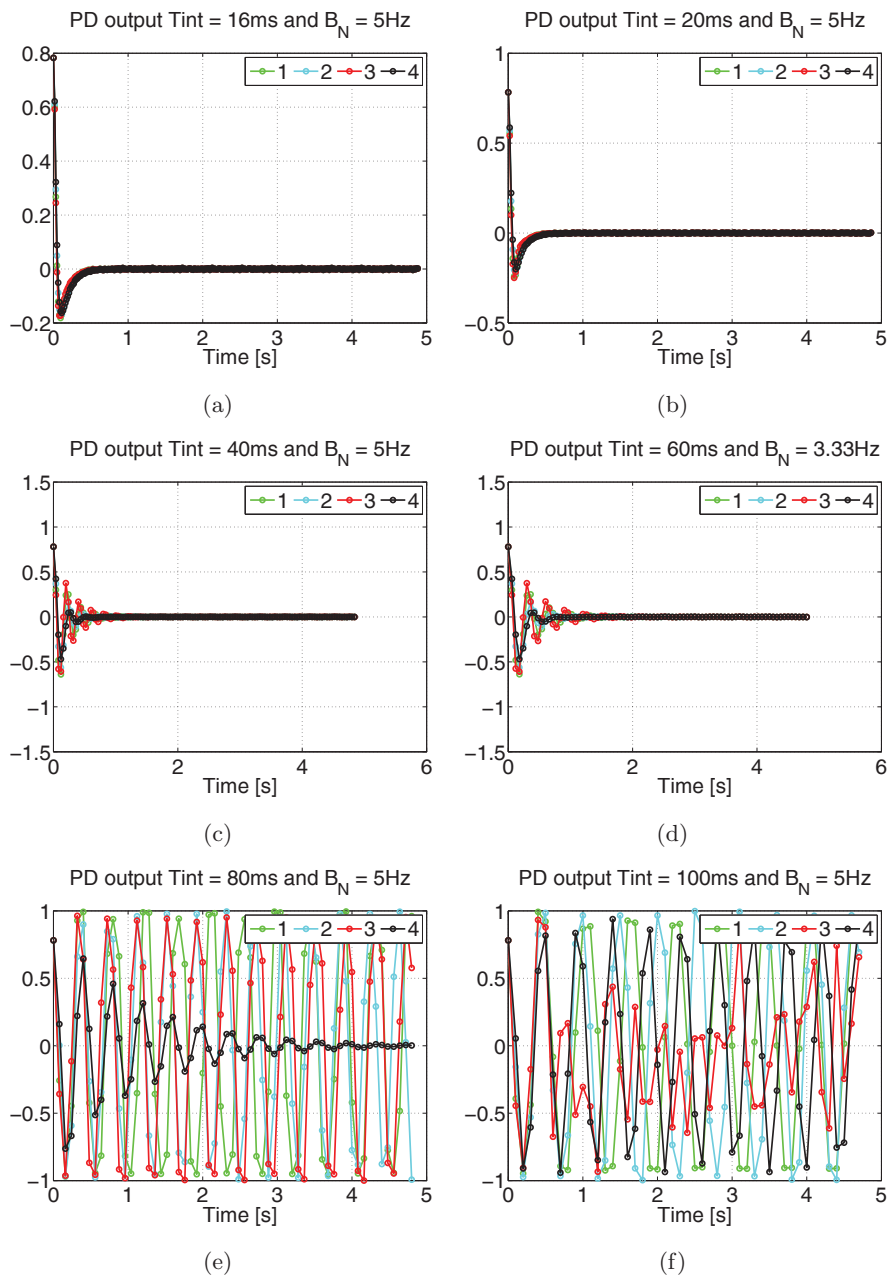
Figure 3.71: EMLE PD output in chips with a constant code rate input on Galileo E5a band - testing different loop filters to track the effect of a constant 2 kHz Doppler frequency on the Galileo E5a code rate with a CNR of 45 dB-Hz and using different B_N and PDI values yielding a range of B_L values a) $T_I = 16$ ms and $B_L = 0.08$ b) $T_I = 20$ ms and $B_L = 0.1$ c) $T_I = 40$ ms and $B_L = 0.2$ d) $T_I = 60$ ms and $B_L = 0.2$ e) $T_I = 80$ ms and $B_L = 0.4$ f) $T_I = 100$ ms and $B_L = 0.5$.

Figure 3.72: Loop filter constant code rate estimation on Galileo E5a band - testing different loop filters to track the effect of a constant 2 kHz Doppler frequency on the Galileo E5a code rate with a CNR of 45 dB-Hz and using different B_N and PDI values yielding a range of B_L values a) $T_I = 16$ ms and $B_L = 0.08$ b) $T_I = 20$ ms and $B_L = 0.1$ c) $T_I = 40$ ms and $B_L = 0.2$ d) $T_I = 60$ ms and $B_L = 0.2$ e) $T_I = 80$ ms and $B_L = 0.4$ f) $T_I = 100$ ms and $B_L = 0.5$.
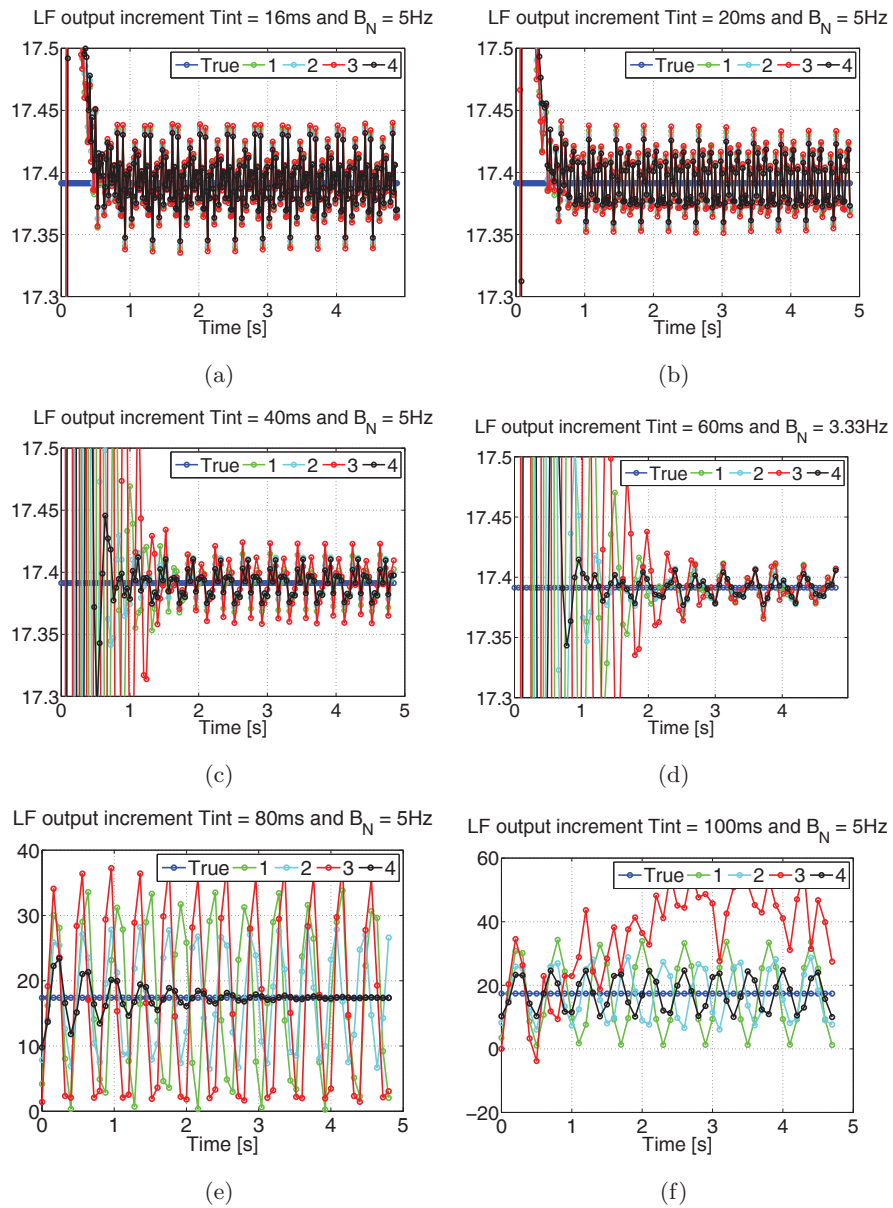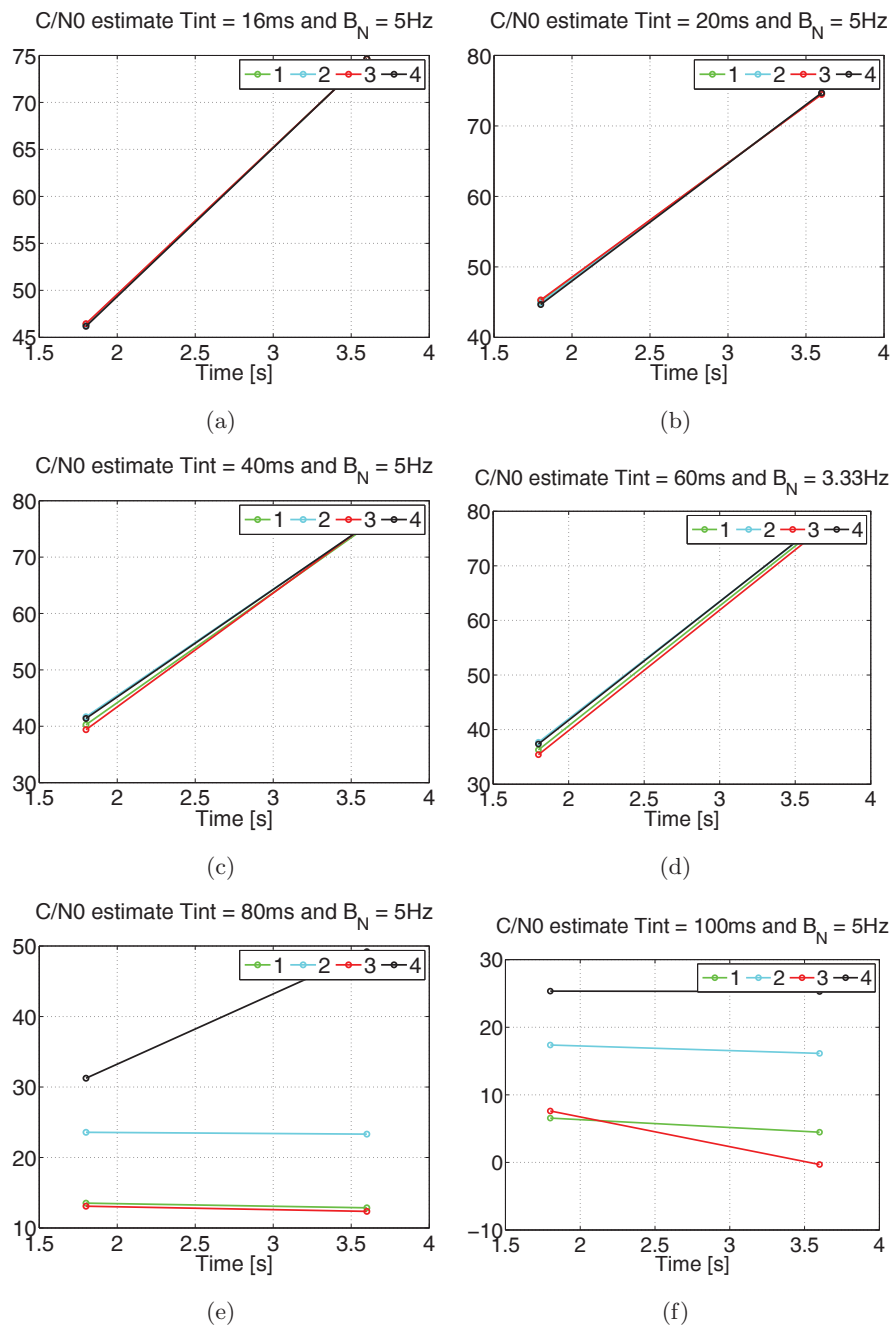
Figure 3.73: CNR estimate in dB-Hz with a constant code rate input on Galileo E5a band - testing different loop filters to track the effect of a constant 2 kHz Doppler frequency on the Galileo E5a code rate with a CNR of 45 dB-Hz and using different B_N and PDI values yielding a range of B_L values a) $T_I = 16$ ms and $B_L = 0.08$ b) $T_I = 20$ ms and $B_L = 0.1$ c) $T_I = 40$ ms and $B_L = 0.2$ d) $T_I = 60$ ms and $B_L = 0.2$ e) $T_I = 80$ ms and $B_L = 0.4$ f) $T_I = 100$ ms and $B_L = 0.5$.

Figure 3.74: EMLE PD output in chips with a ramp code rate input on Galileo E5a band - testing different loop filters to track the effect of a variable Doppler frequency on the Galileo E5a code rate with a CNR of 45 dB-Hz and using different B_N and PDI values yielding a range of B_L values a) $T_I = 16$ ms and $B_L = 0.08$ b) $T_I = 20$ ms and $B_L = 0.1$ c) $T_I = 40$ ms and $B_L = 0.2$ d) $T_I = 60$ ms and $B_L = 0.2$ e) $T_I = 80$ ms and $B_L = 0.4$ f) $T_I = 100$ ms and $B_L = 0.5$.
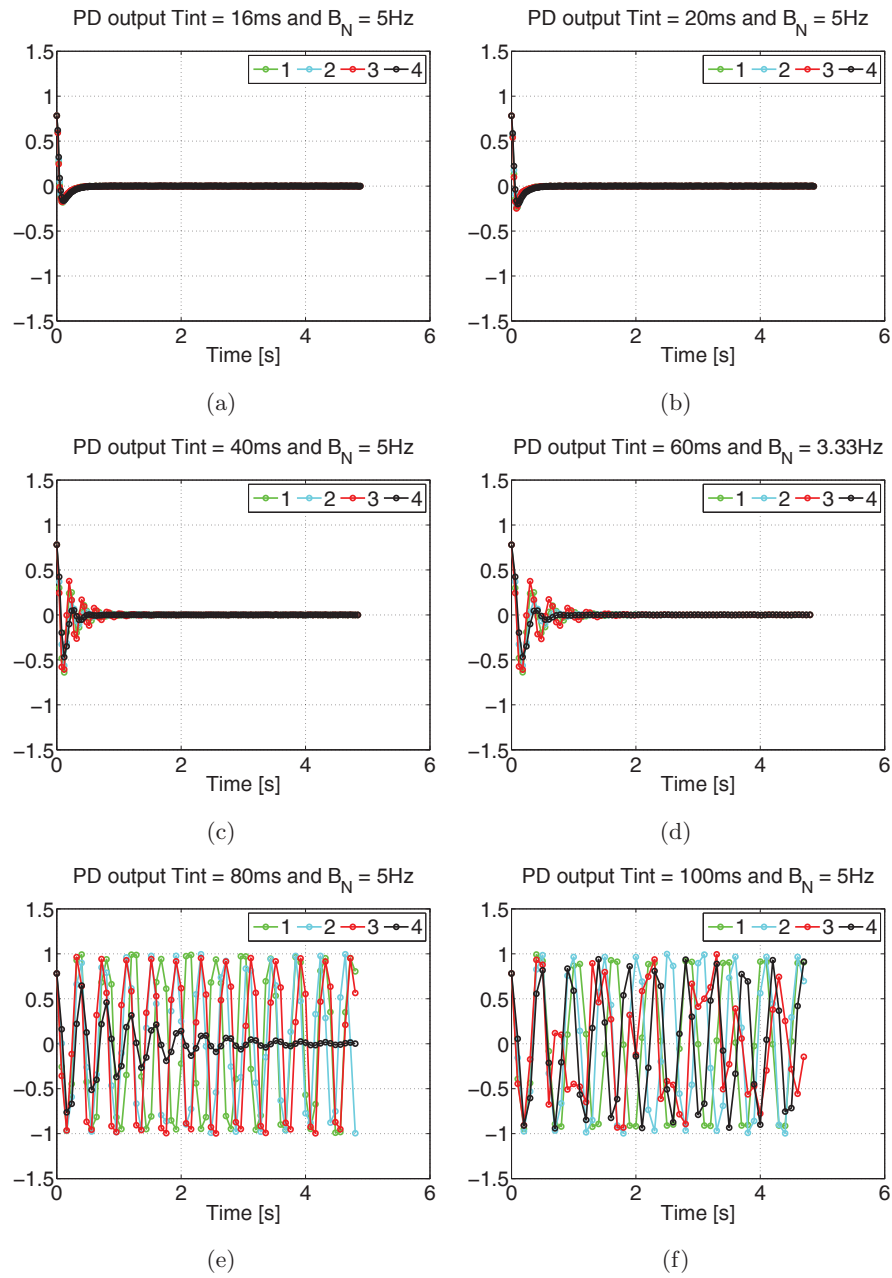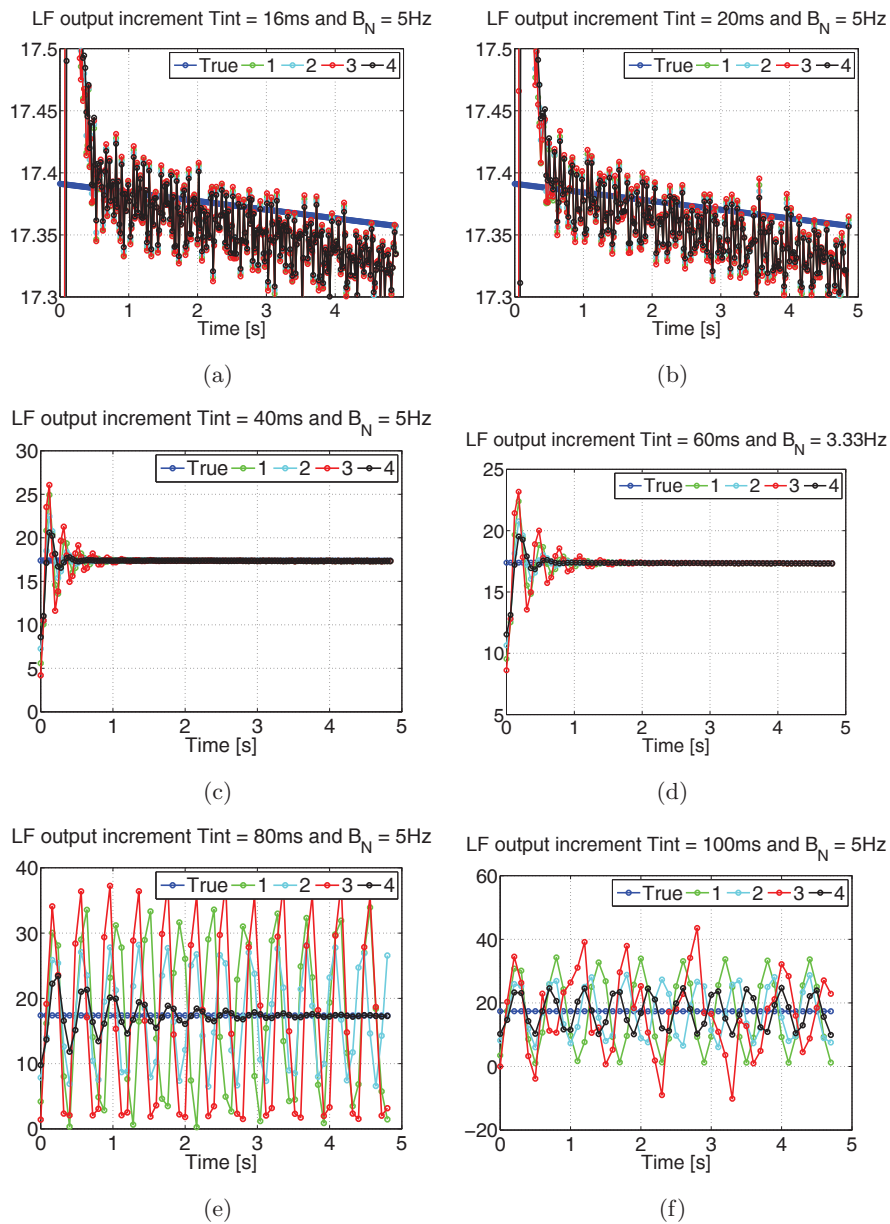
Figure 3.75: Loop filter ramp code rate estimation on Galileo E5a band - testing different loop filters to track the effect of a variable Doppler frequency on the Galileo E5a code rate with a CNR of 45 dB-Hz and using different B_N and PDI values yielding a range of B_L values a) $T_I = 16$ ms and $B_L = 0.08$ b) $T_I = 20$ ms and $B_L = 0.1$ c) $T_I = 40$ ms and $B_L = 0.2$ d) $T_I = 60$ ms and $B_L = 0.2$ e) $T_I = 80$ ms and $B_L = 0.4$ f) $T_I = 100$ ms and $B_L = 0.5$.

Figure 3.76: CNR estimate in dB-Hz with a ramp code rate input on Galileo E5a band - testing different loop filters to track the effect of a variable Doppler frequency on the Galileo E5a code rate with a CNR of 45 dB-Hz and using different B_N and PDI values yielding a range of B_L values a) $T_I = 16$ ms and $B_L = 0.08$ b) $T_I = 20$ ms and $B_L = 0.1$ c) $T_I = 40$ ms and $B_L = 0.2$ d) $T_I = 60$ ms and $B_L = 0.2$ e) $T_I = 80$ ms and $B_L = 0.4$ f) $T_I = 100$ ms and $B_L = 0.5$.

Figure 3.77: PLL PD estimated error with a ramp carrier frequency input signal modulated by a Galileo E1 OS signal - a CNR of 30 dB-Hz, testing different loop filters while using different B_N and PDI values yielding a range of B_L values a) $T_I = 16$ ms and $B_L = 0.16$ b) $T_I = 20$ ms and $B_L = 0.2$ c) $T_I = 40$ ms and $B_L = 0.4$ d) $T_I = 60$ ms and $B_L = 0.48$ e) $T_I = 80$ ms and $B_L = 0.48$ f) $T_I = 100$ ms and $B_L = 0.5$.
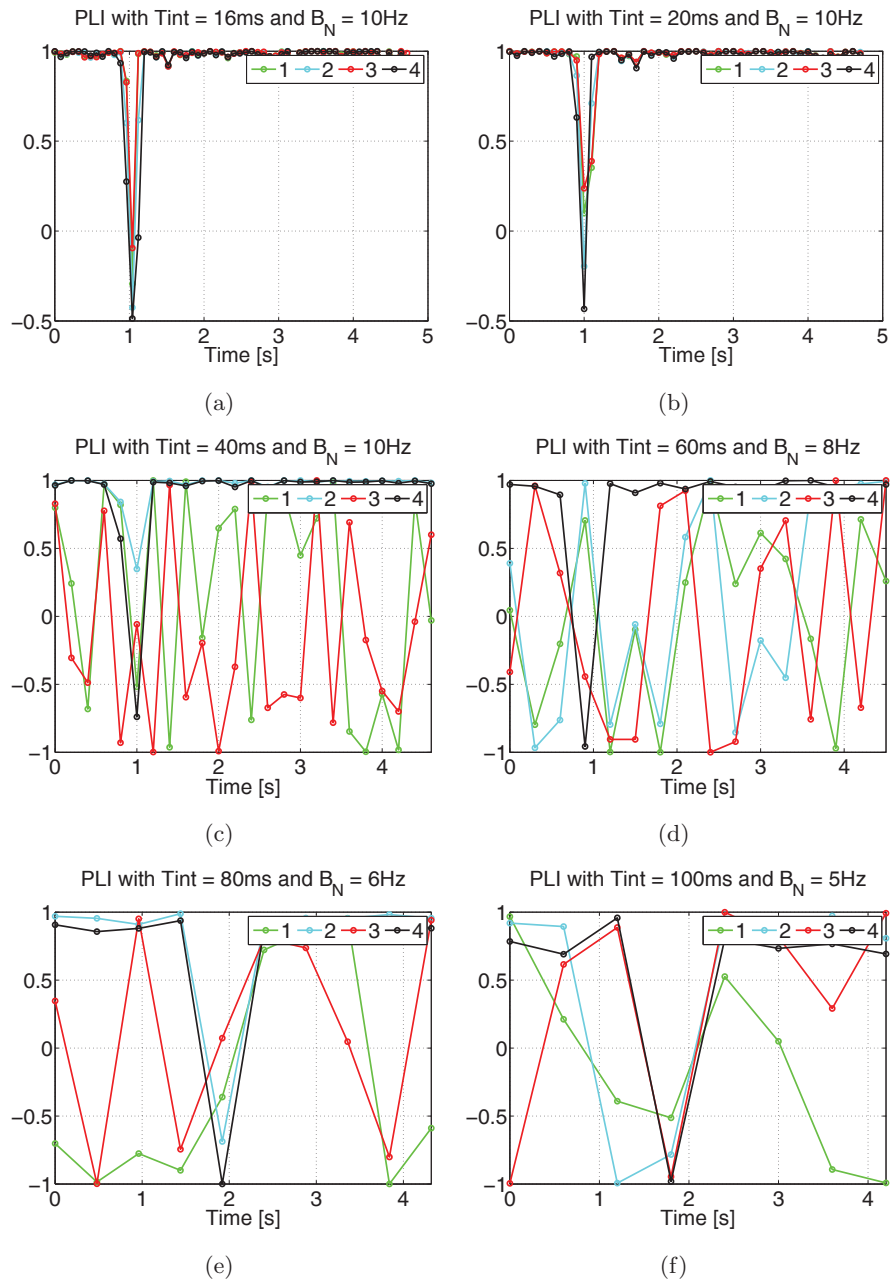
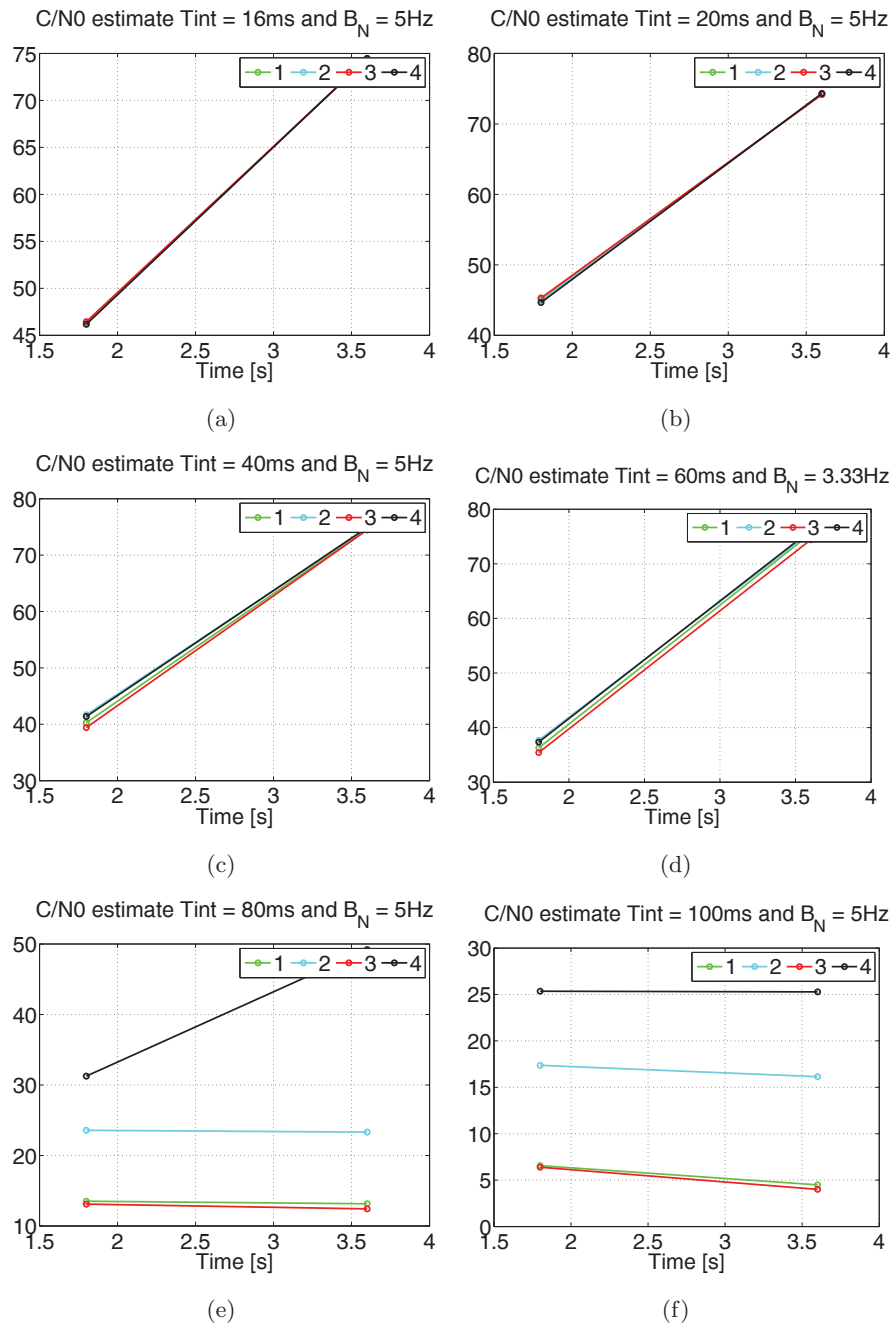**Figure 3.78: PLI with a ramp carrier frequency input signal modulated by a Galileo E1 OS signal** - a CNR of 30 dB-Hz, testing different loop filters while using different B_N and PDI values yielding a range of B_L values a) $T_I = 16$ ms and $B_L = 0.16$ b) $T_I = 20$ ms and $B_L = 0.2$ c) $T_I = 40$ ms and $B_L = 0.4$ d) $T_I = 60$ ms and $B_L = 0.48$ e) $T_I = 80$ ms and $B_L = 0.48$ f) $T_I = 100$ ms and $B_L = 0.5$.
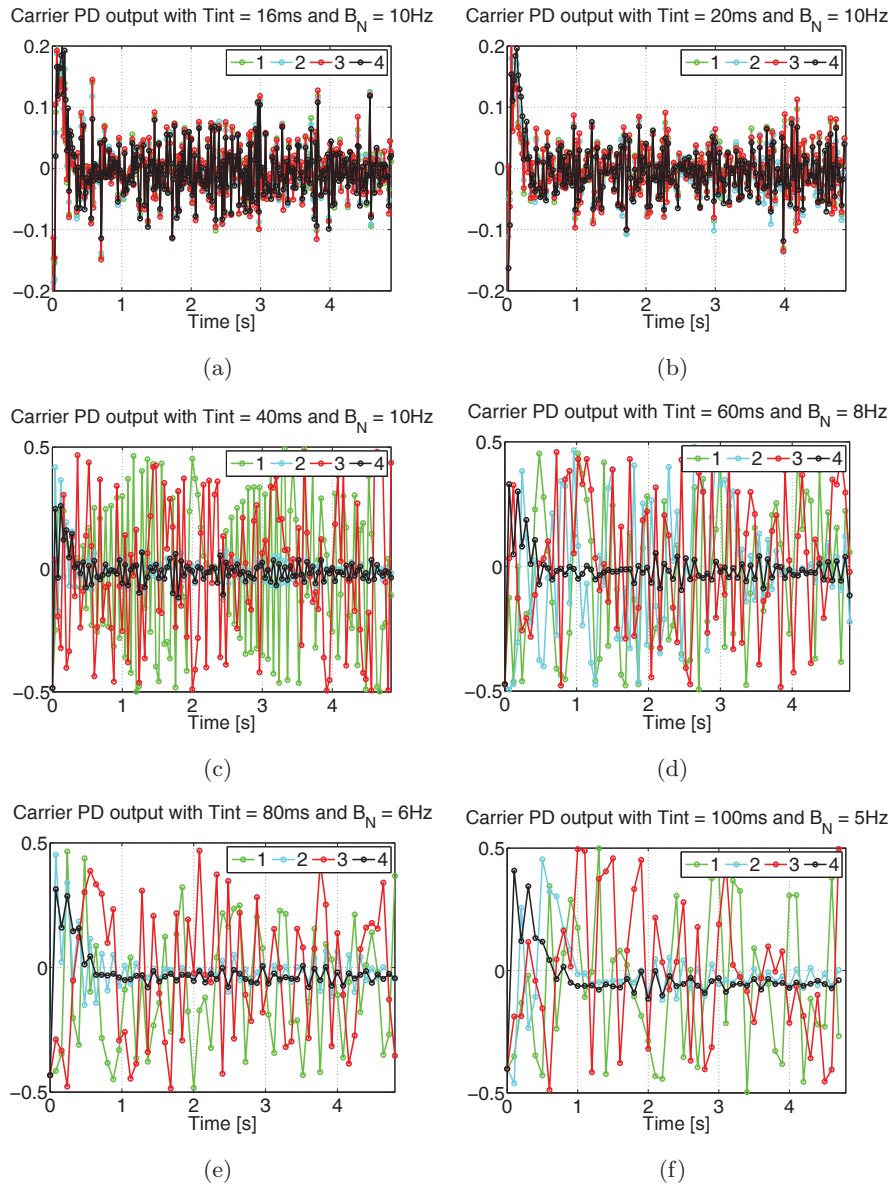
Figure 3.79: PLL Loop filter outputs with a ramp carrier frequency input signal modulated by a Galileo E1 OS signal - a CNR of 30 dB-Hz, testing different loop filters while using different B_N and PDI values yielding a range of B_L values a) $T_I = 16$ ms and $B_L = 0.16$ b) $T_I = 20$ ms and $B_L = 0.2$ c) $T_I = 40$ ms and $B_L = 0.4$ d) $T_I = 60$ ms and $B_L = 0.48$ e) $T_I = 80$ ms and $B_L = 0.48$ f) $T_I = 100$ ms and $B_L = 0.5$.

Figures 3.77 to 3.82 look into the Galileo E1, E5a PLL PD outputs, phase lock indicators and loop filter carrier frequency estimates. Figures 3.77 and 3.79 related to Galileo E1 signals show that for the loop normalized noise equivalent bandwidth B_L values less than 0.2, all four loop filters exhibit similar phase and frequency tracking performance. On the other hand, higher B_L values yield false or loss of tracking for methods 1 and 3, while method 2 and 4 show stable tracking for a B_L as high as 0.5 even though the case where method 2 is used with an integration time of 60 ms seems initially out of lock, it is able to go in lock after 3 seconds. It is interesting to compare the PLL tracking performance with Galileo E5a signals to that of Galileo E1 signals. In fact, methods 2 and 4 seem to endure cycle slips with Galileo E5a signals but eventually approach to lock to the correct frequency. The results agree with the theoretical analysis performed earlier where the Bode plots have shown that for methods 1 and 3, the closed loop system becomes an all pass filter for $B_L > 0.2$ while the low pass filter characteristics remain for methods 2 and 4. Root locus plots on the other hand have shown the progress of the nature of the loop response where the initially designed underdamped response moves towards critically damped and overdamped for methods 1 and 3 respectively, while complex conjugate poles characteristic of an underdamped response hold for high B_L values using methods 2 and 4.

Similarly, Figures 3.83 to 3.88 are the result of tracking the aforementioned simulated Galileo E1 and E5a signals and look into the DLL PD outputs, code lock indicators represented by the CNR and incremental loop filter code rate estimates. The same conclusions are drawn as before.
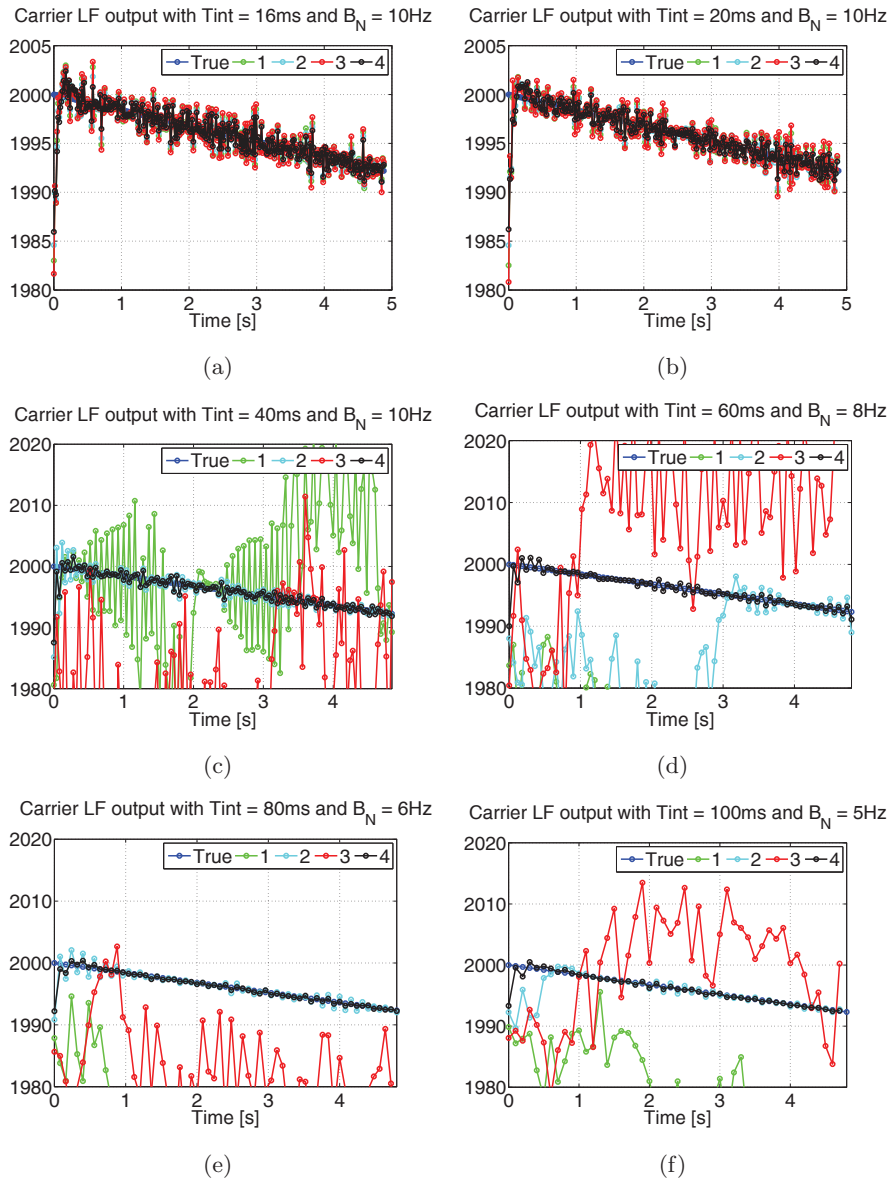
Figure 3.80: PLL PD estimated error with a ramp carrier frequency input signal modulated by a Galileo E5a OS signal - a CNR of 30 dB-Hz, testing different loop filters while using different B_N and PDI values yielding a range of B_L values a) $T_I = 16$ ms and $B_L = 0.16$ b) $T_I = 20$ ms and $B_L = 0.2$ c) $T_I = 40$ ms and $B_L = 0.4$ d) $T_I = 60$ ms and $B_L = 0.48$ e) $T_I = 80$ ms and $B_L = 0.48$ f) $T_I = 100$ ms and $B_L = 0.5$.

Figure 3.81: PLI with a ramp carrier frequency input signal modulated by a Galileo E5a OS signal - a CNR of 30 dB-Hz, testing different loop filters while using different B_N and PDI values yielding a range of B_L values a) $T_I = 16$ ms and $B_L = 0.16$ b) $T_I = 20$ ms and $B_L = 0.2$ c) $T_I = 40$ ms and $B_L = 0.4$ d) $T_I = 60$ ms and $B_L = 0.48$ e) $T_I = 80$ ms and $B_L = 0.48$ f) $T_I = 100$ ms and $B_L = 0.5$.
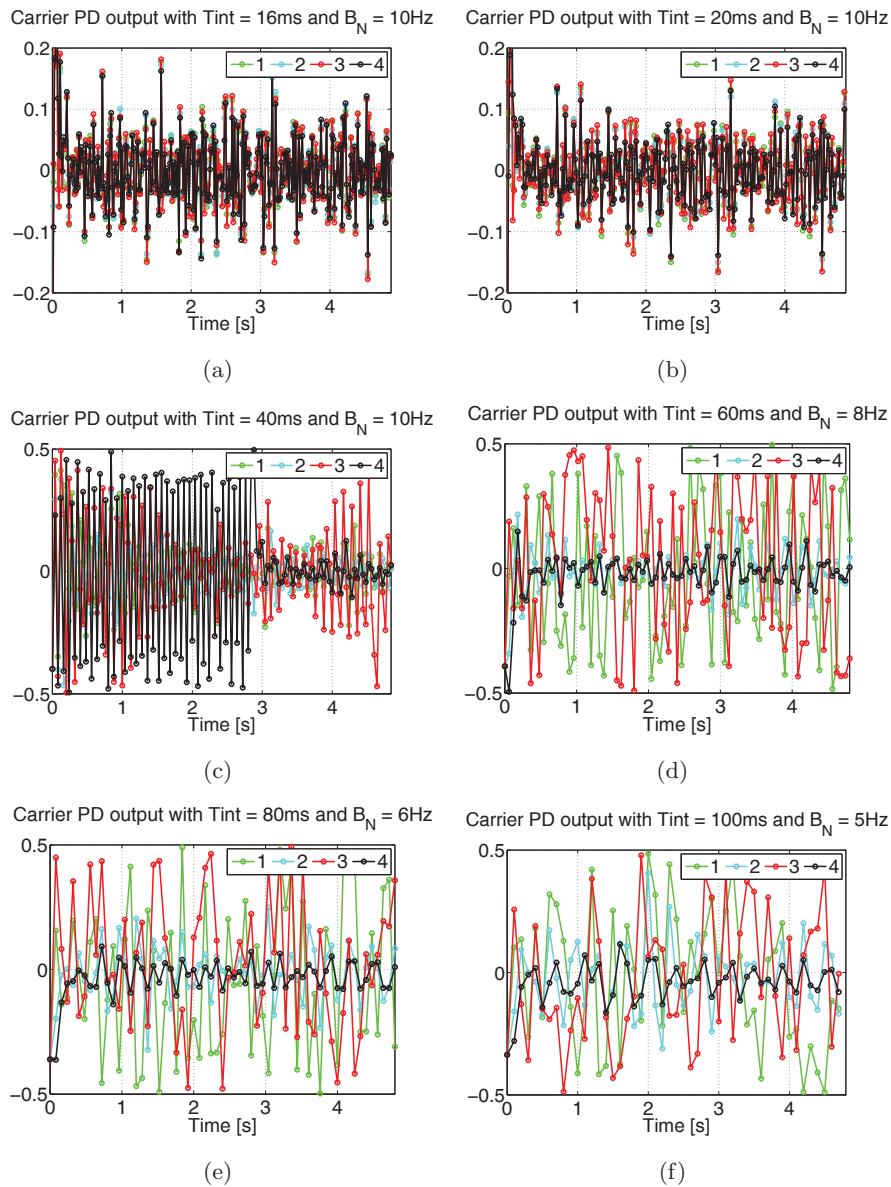
Figure 3.82: PLL Loop filter outputs with a ramp carrier frequency input signal modulated by a Galileo E5a OS signal - a CNR of 30 dB-Hz, testing different loop filters while using different B_N and PDI values yielding a range of B_L values a) $T_I = 16$ ms and $B_L = 0.16$ b) $T_I = 20$ ms and $B_L = 0.2$ c) $T_I = 40$ ms and $B_L = 0.4$ d) $T_I = 60$ ms and $B_L = 0.48$ e) $T_I = 80$ ms and $B_L = 0.48$ f) $T_I = 100$ ms and $B_L = 0.5$.

Figure 3.83: DLL Four taps EMLE PD output in chips with a ramp carrier frequency input signal modulated by a Galileo E1 OS signal - a CNR of 30 dB-Hz, testing different loop filters while using different B_N and PDI values yielding a range of B_L values a) $T_I = 16$ ms and $B_L = 0.08$ b) $T_I = 20$ ms and $B_L = 0.1$ c) $T_I = 40$ ms and $B_L = 0.2$ d) $T_I = 60$ ms and $B_L = 0.2$ e) $T_I = 80$ ms and $B_L = 0.4$ f) $T_I = 100$ ms and $B_L = 0.5$.
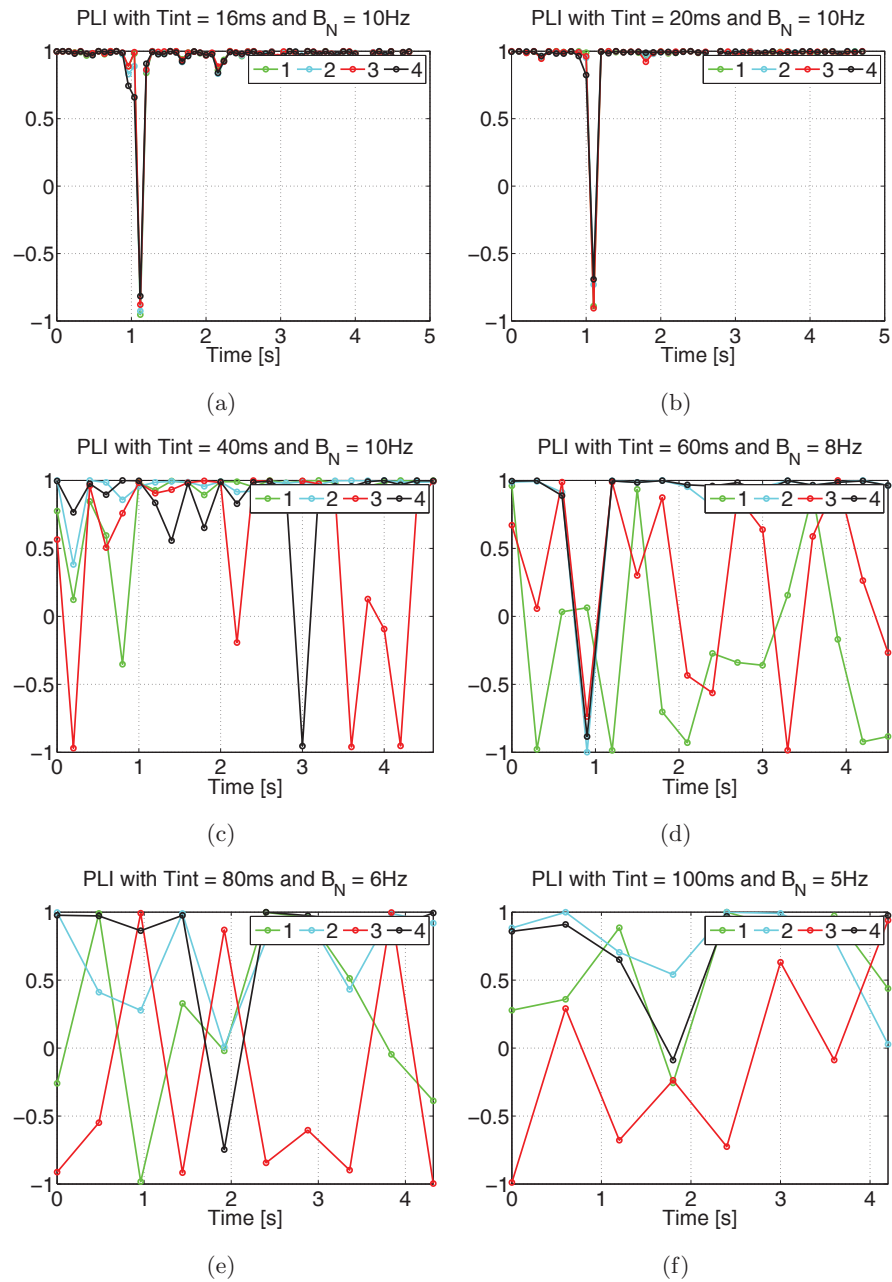
Figure 3.84: DLL Loop filter outputs with a ramp carrier frequency input signal modulated by a Galileo E1 OS signal - a CNR of 30 dB-Hz, testing different loop filters while using different B_N and PDI values yielding a range of B_L values a) $T_I = 16$ ms and $B_L = 0.08$ b) $T_I = 20$ ms and $B_L = 0.1$ c) $T_I = 40$ ms and $B_L = 0.2$ d) $T_I = 60$ ms and $B_L = 0.2$ e) $T_I = 80$ ms and $B_L = 0.4$ f) $T_I = 100$ ms and $B_L = 0.5$.
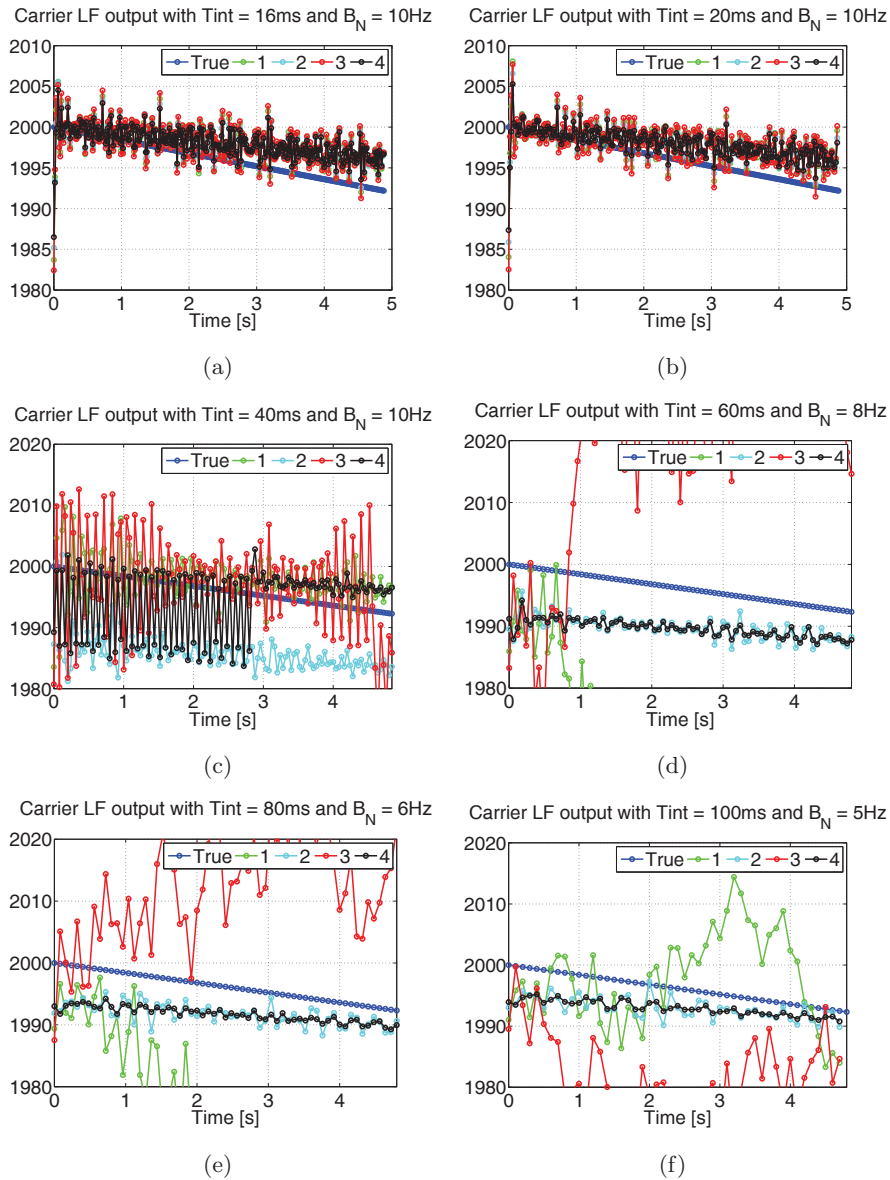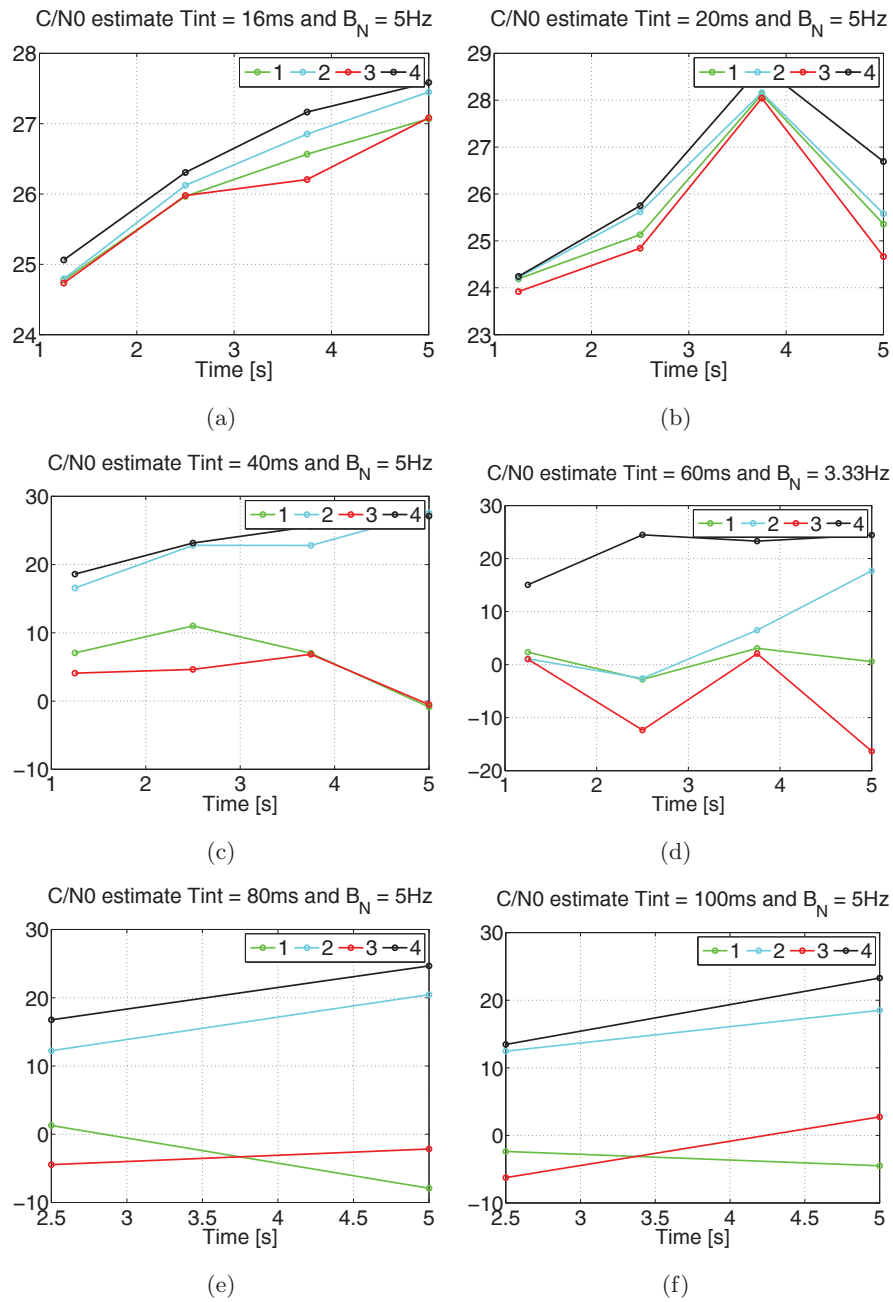
Figure 3.85: CNR estimate in dB-Hz with a ramp carrier frequency input signal modulated by a Galileo E1 OS signal - a CNR of 30 dB-Hz, testing different loop filters while using different B_N and PDI values yielding a range of B_L values a) $T_I = 16$ ms and $B_L = 0.08$ b) $T_I = 20$ ms and $B_L = 0.1$ c) $T_I = 40$ ms and $B_L = 0.2$ d) $T_I = 60$ ms and $B_L = 0.2$ e) $T_I = 80$ ms and $B_L = 0.4$ f) $T_I = 100$ ms and $B_L = 0.5$.
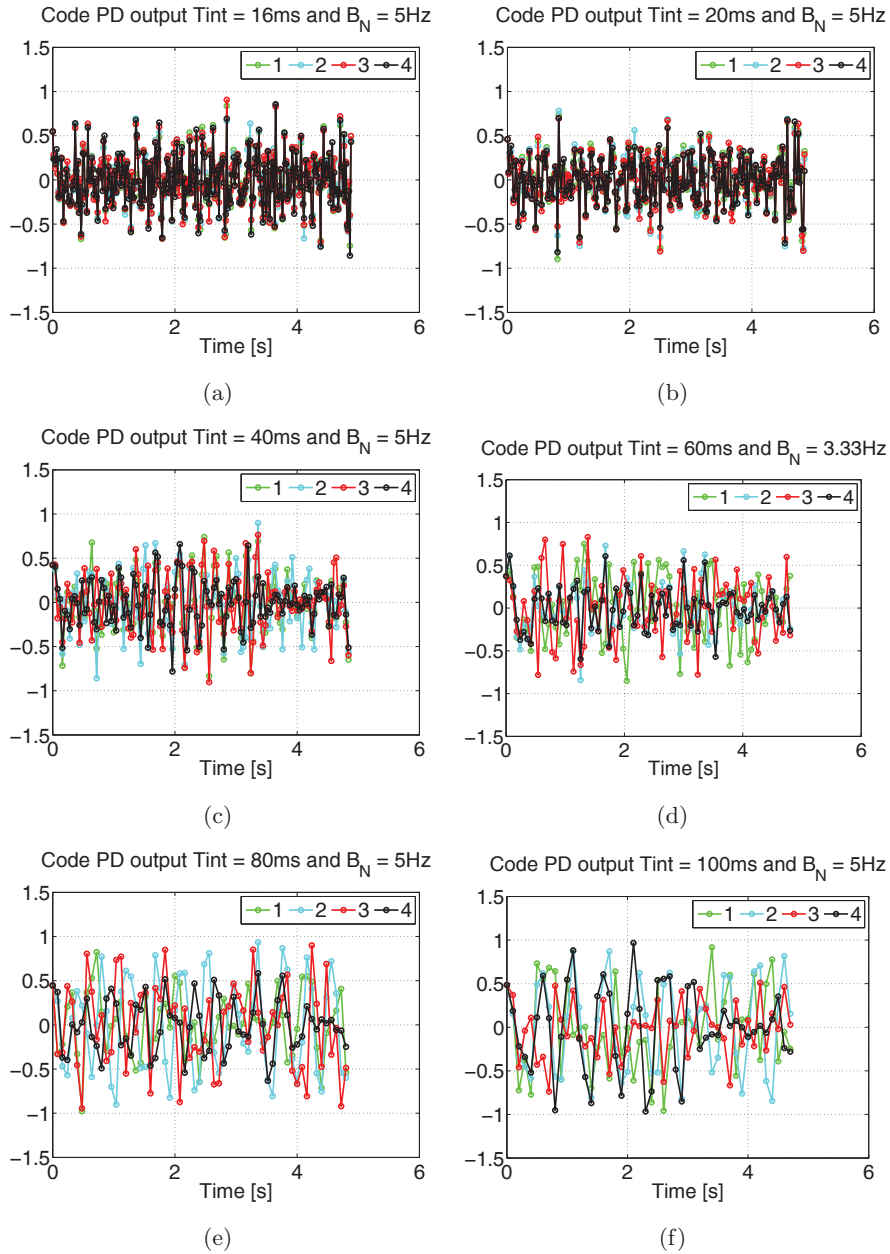
Figure 3.86: DLL Four taps VEMLE PD output in chips with a ramp carrier frequency input signal modulated by a Galileo E5a OS signal - a CNR of 30 dB-Hz, testing different loop filters while using different B_N and PDI values yielding a range of B_L values a) $T_I = 16$ ms and $B_L = 0.08$ b) $T_I = 20$ ms and $B_L = 0.1$ c) $T_I = 40$ ms and $B_L = 0.2$ d) $T_I = 60$ ms and $B_L = 0.2$ e) $T_I = 80$ ms and $B_L = 0.4$ f) $T_I = 100$ ms and $B_L = 0.5$.
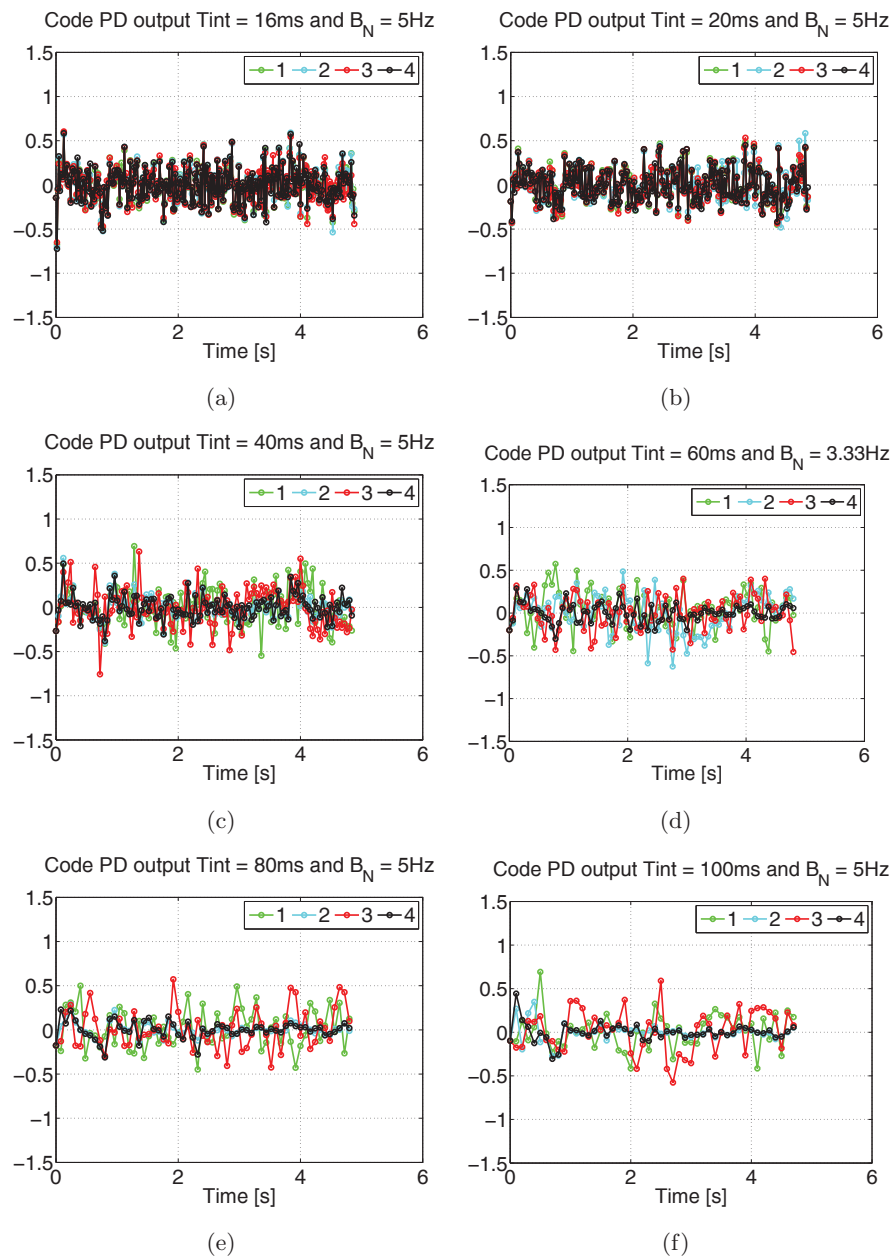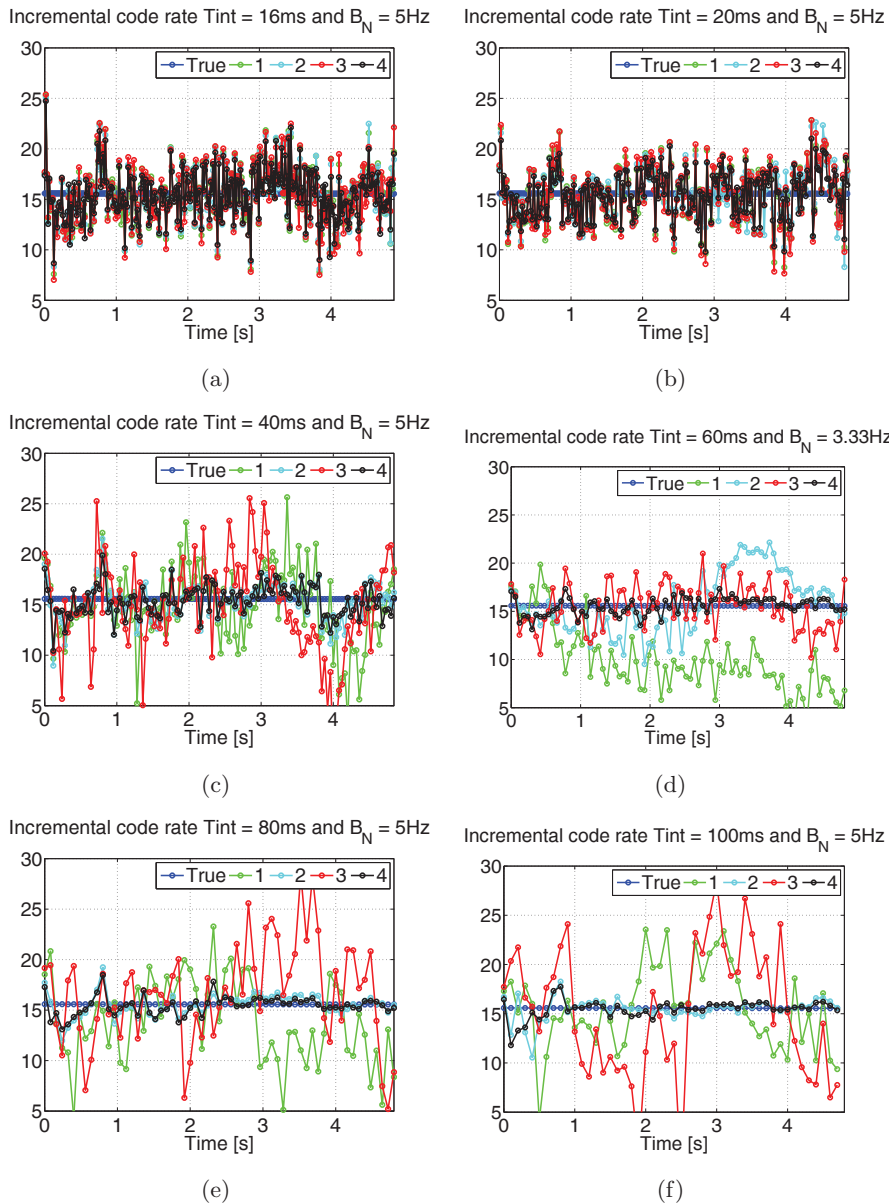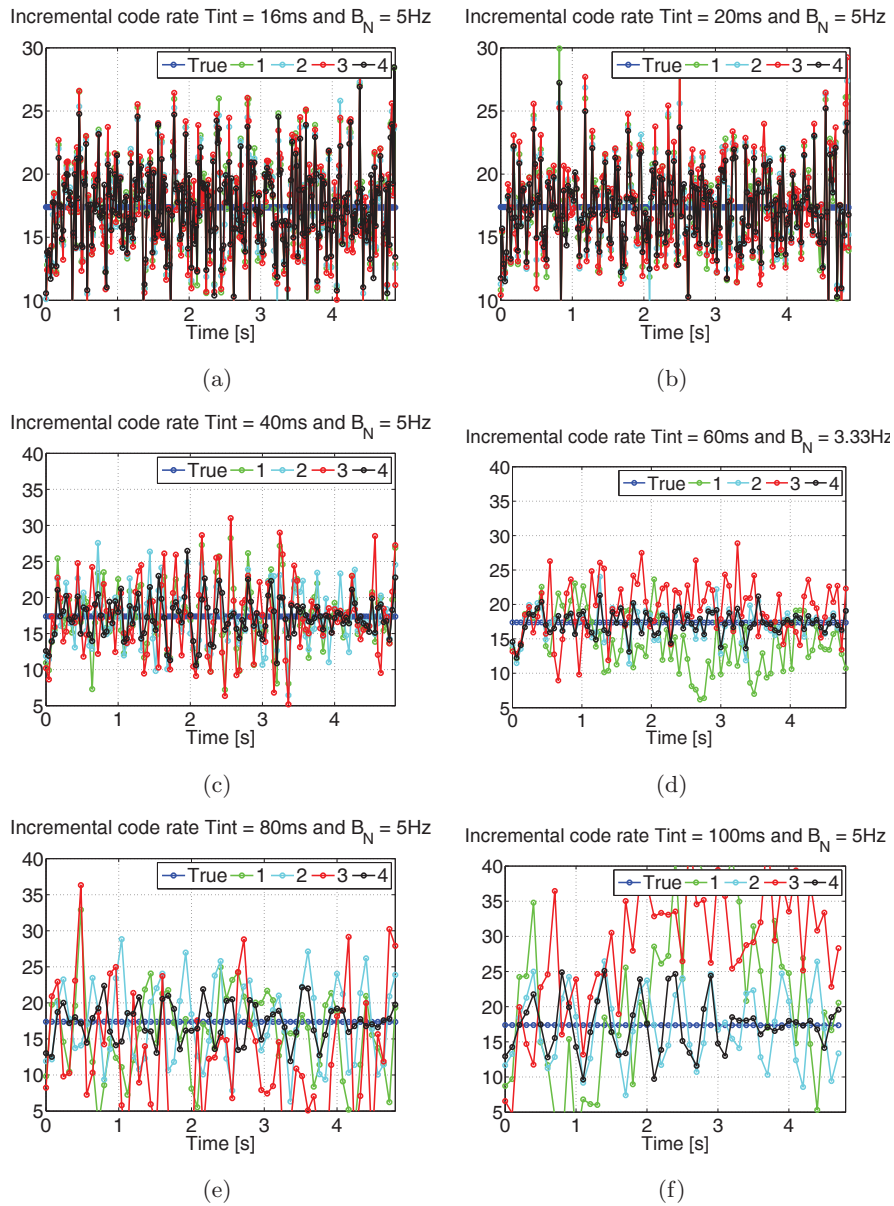
Figure 3.87: DLL Loop filter outputs with a ramp carrier frequency input signal modulated by a Galileo E5a OS signal - a CNR of 30 dB-Hz, testing different loop filters while using different B_N and PDI values yielding a range of B_L values a) $T_I = 16$ ms and $B_L = 0.08$ b) $T_I = 20$ ms and $B_L = 0.1$ c) $T_I = 40$ ms and $B_L = 0.2$ d) $T_I = 60$ ms and $B_L = 0.2$ e) $T_I = 80$ ms and $B_L = 0.4$ f) $T_I = 100$ ms and $B_L = 0.5$.

171

Figure 3.88: CNR estimate in dB-Hz with a ramp carrier frequency input signal modulated by a Galileo E5a OS signal - a CNR of 30 dB-Hz, testing different loop filters while using different B_N and PDI values yielding a range of B_L values a) $T_I = 16$ ms and $B_L = 0.08$ b) $T_I = 20$ ms and $B_L = 0.1$ c) $T_I = 40$ ms and $B_L = 0.2$ d) $T_I = 60$ ms and $B_L = 0.2$ e) $T_I = 80$ ms and $B_L = 0.4$ f) $T_I = 100$ ms and $B_L = 0.5$.

3.6 Bandlimiting effects
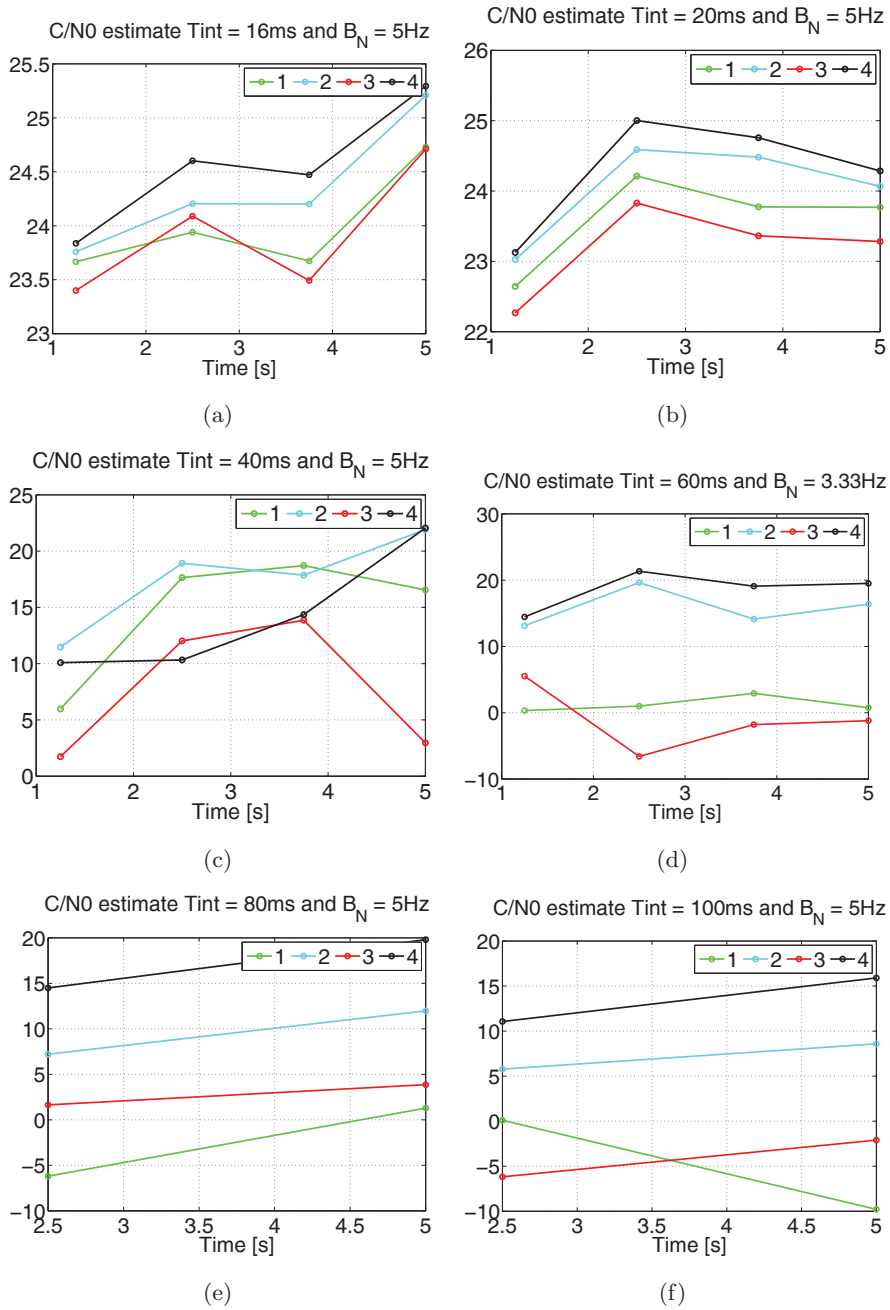
In practice, the front-end bandwidth is finite and depending on the applications and receiver limitations, it can be set to arbitrarily low values. For instance, the Galileo E1 OS signal is specified in the Galileo ICD [21] to have a reference bandwidth of 24.552 MHz. However, a theoretical bandwidth of 14.322 MHz $= 2 * (6.138 + 1.023)$ MHz, that accomodates the two BOC signals, BOC(6,1) and BOC(1,1), may cover a large percentage of the signal power spectrum. In the following, we will undertake the task of indicating the losses incurred by limited bandwidth receivers. The normalized PSD of a baseband signal using a BOC modulation, defined as BOC(m,n) is expressed as [46]:

$$G_s(f) = f_c \left(\frac{\sin\left(\frac{\pi f}{2f_{sc}}\right) \sin\left(\frac{\pi f}{f_c}\right)}{\pi f \cos\left(\frac{\pi f}{2f_{sc}}\right)} \right)^2 \tag{3.163}$$

where $f_{sc} = m \cdot 1.023$ MHz is the subcarrier frequency and $f_c = n \cdot 1.023$ MHz is the chip rate. The Galileo E1 OS signal is an MBOC(6,1,1/11) modulated signal, having a PSD $G_s(f)$ as defined in Section 2.2.1. On the other hand, the normalized PSD of a baseband signal using a BPSK modulation, defined as BPSK(m) is expressed as:

$$G_s(f) = f_c \left(\frac{\sin(\frac{\pi f}{f_c})}{\pi f} \right)^2 \tag{3.164}$$

Using this equation, the PSD of the Galileo E5a/b OS signals which are BPSK(10) signals can be computed. Figure 3.89 plots the PSD of the aforementioned Galileo E1 MBOC(6,1,1/11) and E5a/b OS BPSK(10) signals together with the reference BOC(1,1) and BPSK(1) signals.

3.6.1 Correlation loss

The overall power loss due to bandlimiting, also termed correlation loss [46], can be computed over a limiting double-sided complex bandwidth β as:

$$L_c = \int_{-\beta/2}^{\beta/2} G_s(f) df \tag{3.165}$$

The reason why L_c is called correlation loss, lies in the definition of the autocorrelation function which is the inverse Fourier transform of the PSD. Consequently, any change
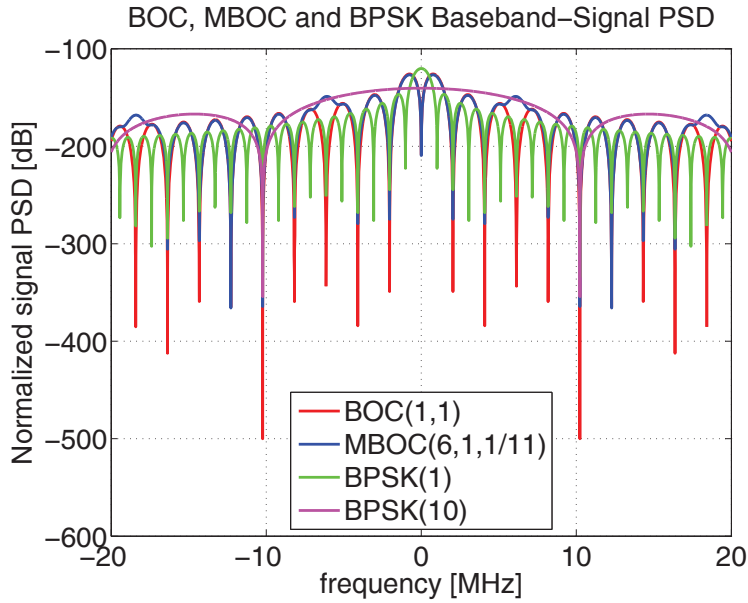
Figure 3.89: Theoretical PSD of the Galileo E1 and E5a/b OS signals - MBOC(6,1,1/11), BPSK(10), and two reference signals BOC(1,1) and BPSK(1)

in the PSD reflects in the shape of the autocorrelation function which is pivotal in the carrier and code tracking stage. It is thus imperative to assess the correlation loss in order to choose an appropriate front-end bandwidth. Figure 3.90 shows the behavior of the correlation loss as given by Equation 3.165 for BOC(1,1), BPSK(10) and MBOC(6,1,1/11) modulated signals. In case of MBOC signals as defined for the Galileo E1 OS signal, a correlation loss of 1.7 dB is incurred for using a 4 MHz bandwidth instead of 14.322 MHz while 1 dB loss corresponds to using 8 MHz bandwidth instead of 14.322 MHz. Beyond 14.322 MHz, the correlation losses for the MBOC signal are negligible (less than 0.5 dB). For Galileo E5a/b BPSK(10) signals, the correlation losses are negligible beyond 20 MHz (less than 1 dB). Table 3.8 summarizes the Galileo E1 and E5a/b OS signals bandlimiting results in terms of correlation loss in dB.

3.6.2 Impact on PLL tracking threshold

It is informative to now look at the impact of the correlation loss on the carrier phase tracking ability of digital loops. The phase tracking jitter or phase error standard deviation at the output of the carrier tracking loop or PLL depends on the phase

FE bandwidth [MHz]	E1 Correlation Loss [dB]	E5a/b Correlation Loss [dB]
4	2.2	8.7
8	1.5	3.7
16	0.5	1.2
20	0.4	1
30	0.3	0.8
∞	0	0

Table 3.8: Galileo E1 MBOC(6,1,1/11) and Galileo E5a/b BPSK(10) correlation loss due to finite front-end bandwidth

Figure 3.90: Correlation loss due to bandlimiting - of BOC(1,1), MBOC(6,1,1/11) and BPSK(10) modulated signals as a function of the double-sided complex front-end bandwidth expressed in dB.

detector or discriminator used in these loops. In case of carrier tracking loops, it is shown in [9] that the thermal noise tracking jitter at the PLL output using either ATAN or ATAN2 discriminator is well approximated by that resulting from the use of a DP discriminator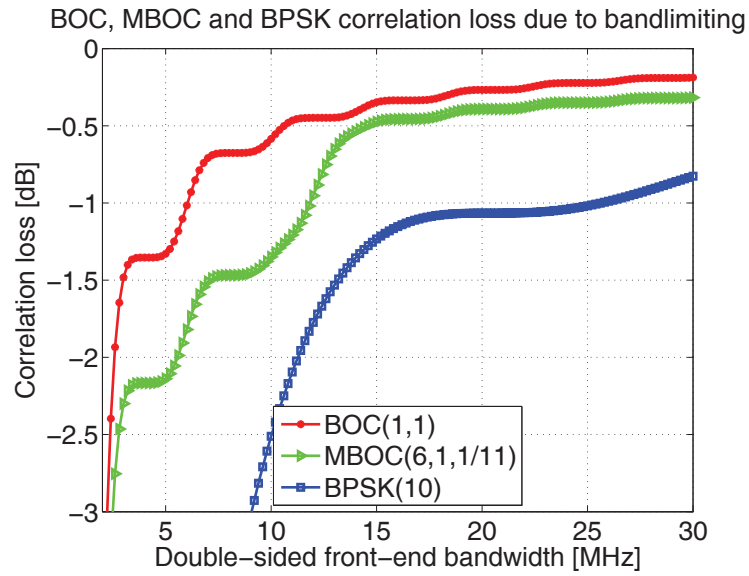 (a noise equivalent loop bandwidth B_N of 10 Hz is assumed). The tracking jitter expression takes into account the bandlimiting effects as well, and is given by:

$$\sigma_{\phi,DP}^2 = \frac{B_N(1 - 0.5B_N T_I)}{L_c C/N_0} \left(1 + \frac{1}{2L_c C/N_0 T_I}\right) \qquad (3.166)$$

The coherent discriminator for a PLL has a more simplified expression for the tracking error variance due to the absence of the squaring loss:

$$\sigma_{\phi,Coh}^2 = \frac{B_N(1 - 0.5B_N T_I)}{L_c C/N_0} \qquad (3.167)$$

It is straightforward to note that the tracking jitter as computed from 3.166 and 3.167 increases with decreasing CNR values but depending on the chosen FE bandwidth, and for the same CNR this jitter slightly decreases or remains the same as plotted in Figures 3.91 and 3.92. Consequently, the chosen bandwidth may or may not have an impact on decreasing the probability of losing lock which is normally considered to occur when the total tracking jitter exceeds 15 degrees [47]. More precisely, the tracking threshold depends on the two-sided phase discriminator linear tracking region L_ϕ and the loss of lock condition entails that [9, 47]:

$$\sigma_\phi + \frac{\theta_e}{3} \le \frac{L_\phi}{6} \qquad (3.168)$$

where θ_e is the dynamic stress error of the receiver. Considering a static receiver, and using the aforementioned inequality, Table 3.9 summarizes the different tracking jitter thresholds for different discriminators.

3.6.2.1 Galileo E1 OS signal

Due to the aforementioned considerations, it is possible to plot the thermal noise carrier phase jitter alone by ignoring the other components of the total tracking jitter σ_ϕ. Figures 3.91 and 3.92 depict the behavior of the thermal noise carrier phase jitter for Galileo E1 OS signals. It is worth noting that considering a 16 MHz bandwidth instead of 4 MHz brings an additional margin of 1 dB-Hz weaker signal tracking for CNR lower

Discriminator	Angular threshold [degrees]
DD	20
DP	15
Rat	10
Atan	30
Coh	30
Atan2	60

Table 3.9: PLL tracking jitter thresholds in angular degrees according to various PLL discriminators

Figure 3.91: Galileo E1 Tracking jitter at PLL output using an ATAN2 discriminator for a range of CNR values - a loop bandwidth of 10 Hz and an integration time of 20 ms.

Figure 3.92: Galileo E1 Tracking jitter at PLL output using a COH discriminator for a range of CNR values - a loop bandwidth of 10 Hz and an integration time of 20 ms.

than 25 dB-Hz. On the other hand, the choice of 24 MHz bandwidth instead of a 16 MHz bandwidth yields no significant improvement even for low CNR.

Moreover, for a certain CNR value of 25 dB-Hz, the tracking jitter can differ by as high as a unit degree when choosing a FE bandwidth of 16 MHz instead of 4 MHz as shown in Figure 3.93. This difference is almost the same for an integration time of either 20 ms or 80 ms as shown in Figure 3.94, but the latter shows an overall lower tracking jitter due to better noise averaging.

We can conclude by saying that the bandlimiting impact is degrading when the CNR and the choice of bandwidth are both low. For an overall good performance, a good choice of the bandwidth for Galileo E1 OS signal, CBOC(6,1,1/11) is greater than 16 MHz. However, if the situation is grasped firmly such that the dynamic stress error and the oscillator noise do not pose a major threat in terms of high tracking jitter, the additional 1-5 degrees margin of weak signal tracking can be ignored. In this case only, the bandlimiting effect does not introduce any loss in terms of tracking performance.

Figure 3.93: E1 weak signal PLL tracking jitter as a function of FE bandwidth using an integration time of 20 ms - with a C/N_0 of 25 dB-Hz, a loop bandwidth of 10 Hz considering ATAN2 and COH discriminators.
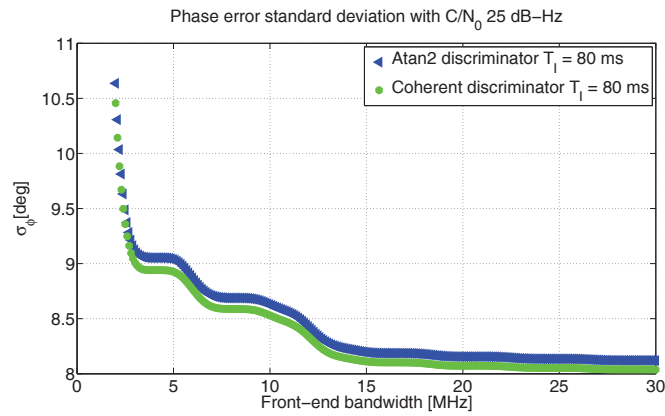
Figure 3.94: E1 weak signal PLL tracking jitter as a function of FE bandwidth using an integration time of 80 ms - with a C/N_0 of 25 dB-Hz, a loop bandwidth of 10 Hz considering ATAN2 and COH discriminators.

179

3.6.2.2   Galileo E5a/b OS signal

Similarly to the Galileo E1 OS signal case, let us consider the thermal noise jitter alone by ignoring the other components of the total tracking jitter σ_ϕ. Figures 3.95 and 3.96 show that considering the Galileo OS E5a signal and the choice of a 30 MHz bandwidth instead of 25 or even 20 MHz brings a very small additional margin of 0.1 dB-Hz weaker signal tracking for CNR lower than 25 dB-Hz.
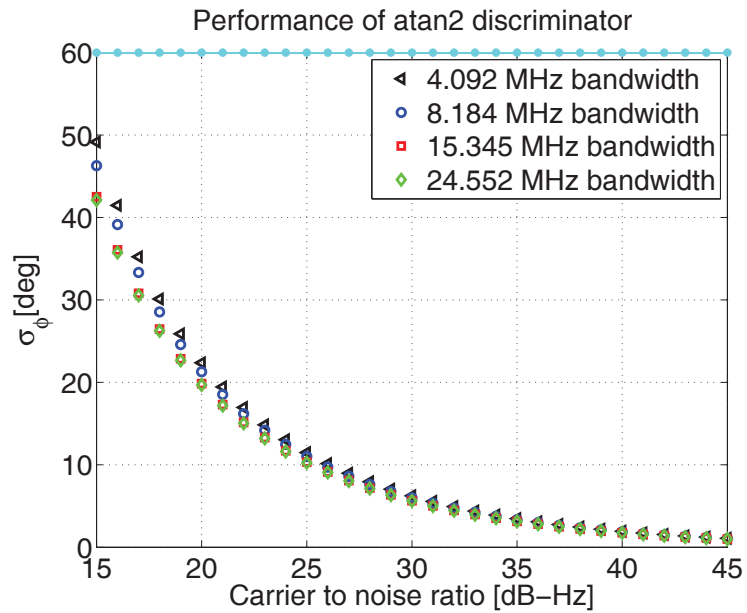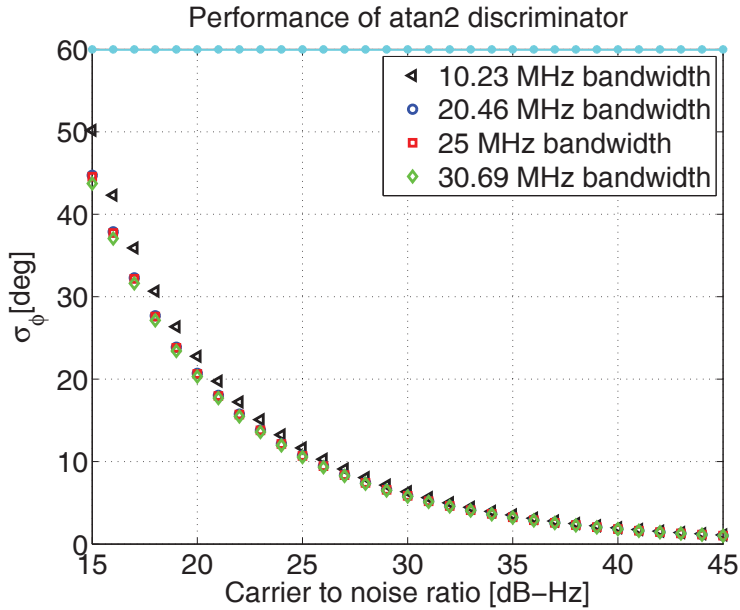

Figure 3.95: Galileo E5a Tracking jitter at PLL output using an ATAN2 discriminator for a range of CNR values - a loop bandwidth of 10 Hz and an integration time of 20 ms.

Moreover, for a certain situation characterized by a CNR of 25 dB-Hz, the tracking jitter as shown in Figure 3.97 differs by as much as 1 degree when choosing a FE bandwidth of 10 MHz instead of 20 MHz but lower than 0.2 degree when using 20 MHz instead of 30 MHz. This difference is almost the same for an integration time of either 20 ms or 80 ms as shown in Figure 3.98, but the latter case shows an overall lower tracking jitter due to better noise averaging.

We can conclude by saying that the bandlimiting impact is degrading when the CNR and the choice of bandwidth are both low. For an overall good performance, a good choice of the bandwidth for Galileo E5a/b OS signal is set greater than 20 MHz.
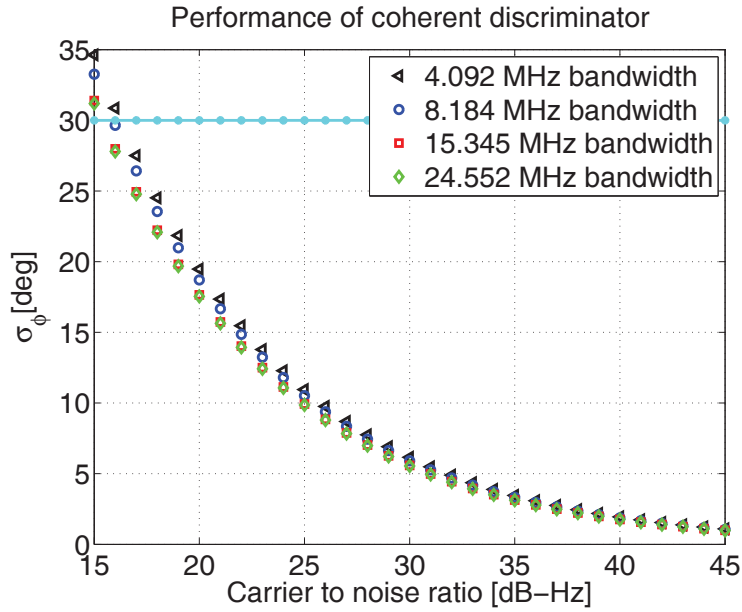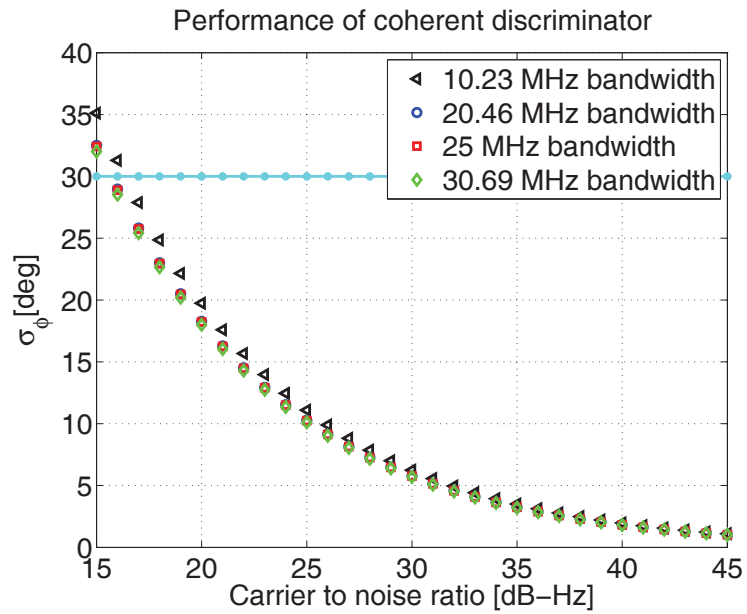
Figure 3.96: Galileo E5a Tracking jitter at PLL output using a COH discriminator for a range of CNR values - a loop bandwidth of 10 Hz and an integration time of 20 ms.
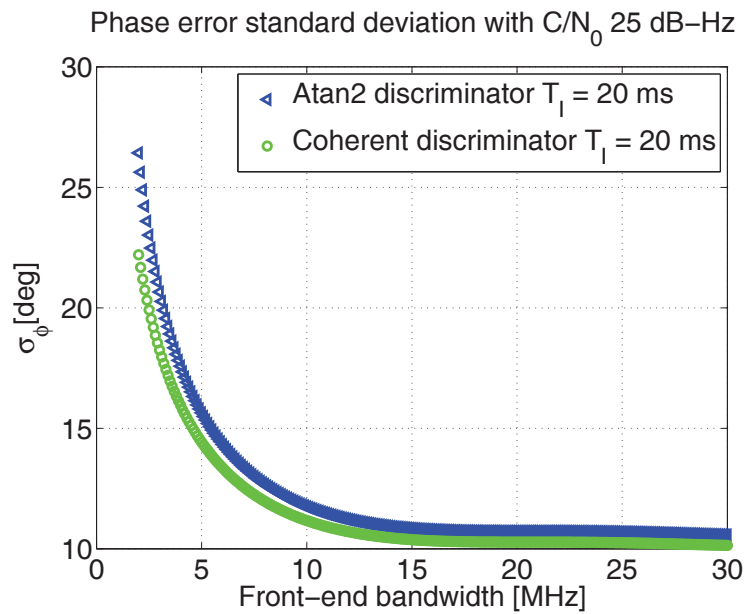
Figure 3.97: E5a weak signal PLL tracking jitter as a function of FE bandwidth using an integration time of 20 ms - with a C/N_0 of 25 dB-Hz, a loop bandwidth of 10 Hz considering ATAN2 and COH discriminators.
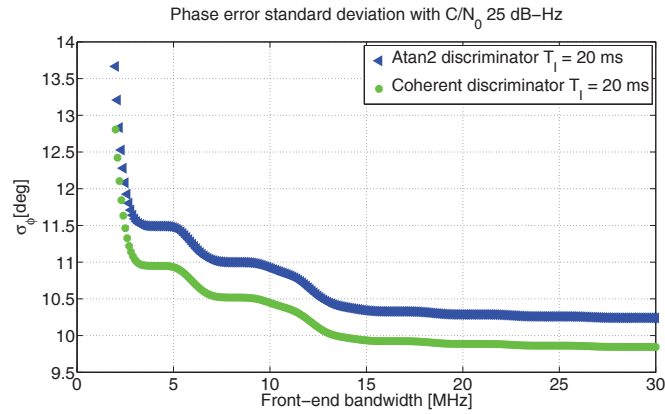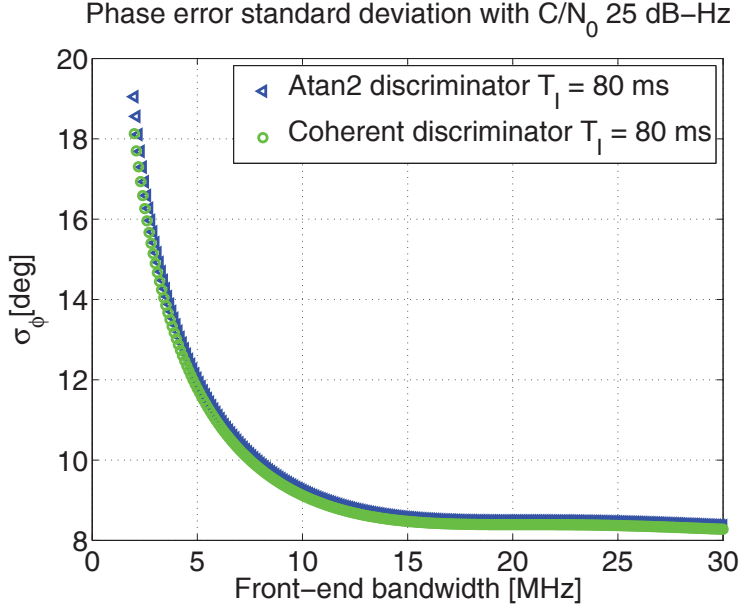
Figure 3.98: E5a weak signal PLL tracking jitter as a function of FE bandwidth using an integration time of 80 ms - with a C/N_0 of 25 dB-Hz, a loop bandwidth of 10 Hz considering ATAN2 and COH discriminators.

3.6.3   Impact on DLL tracking threshold

Switching our attention to the code or subcarrier tracking loop DLL/SLL, it is also worth noting what is the impact of the correlation loss or in a general sense, bandlimiting effect on the code delay tracking ability of digital loops. The code delay tracking jitter at the output of the DLL or SLL depends on the PD or discriminator used in the DLL/SLL loops. Considering the bandlimiting effects, it is shown in [48] that the thermal noise tracking jitter at the DLL/SLL output using a coherent EML discriminator is:

$$\sigma^2_{\tau,EML} = \frac{B_N(1 - 0.5B_N T_I) \int_{-\beta/2}^{\beta/2} G_s(f) \sin^2(\pi f d_s) df}{C/N_0 \left(\int_{-\beta/2}^{\beta/2} f G_s(f) \sin(\pi f d_s) df \right)^2} \tag{3.169}$$

where d_s is the early minus late correlator spacing and B_N is the code tracking loop noise equivalent bandwidth. Similarly, the expression of the thermal noise tracking jitter at the DLL/SLL output using a noncoherent EMLP discriminator is derived in [49]. The result is an additional weighting factor which accounts for the squaring loss

182

due to the noncoherent processing:

$$\sigma^2_{\tau,EMLP} = \sigma^2_{\tau,EML} \left(1 + \frac{\int_{-\beta/2}^{\beta/2} G_s(f) \cos^2(\pi f d_s) df}{C/N_0 T_I \int_{-\beta/2}^{\beta/2} G_s(f) \cos(\pi f d_s) df} \right) \tag{3.170}$$

On the other hand, the noncoherent DP discriminator yields a different weighting factor as shown by [9]:

$$\sigma^2_{\tau,DP} = \sigma^2_{\tau,EML} \left(1 + \frac{1}{C/N_0 T_I \int_{-\beta/2}^{\beta/2} G_s(f) df} \right) \tag{3.171}$$

As in the PLL, the rule of thumb for DLL/SLL tracking threshold beyond which the loop is assumed to go out of lock is defined in terms of the 3-sigma of all errors and the linear region of the discriminator or PD. In theory, the linear region of the PD is half the early late correlator spacing $\pm d_s/2$ and so considering the thermal noise jitter contribution on its own, the tracking threshold condition is:

$$3\sigma_\tau \leq \frac{d_s}{2} \tag{3.172}$$

3.6.3.1 Galileo E1 OS signal

Due to the aforementioned equations, it is possible to plot the theoretical thermal noise code delay tracking jitter alone by ignoring the other components of the total tracking jitter σ_τ. In the following, in both cases of Galileo E1 and E5a/b OS signals, an integration time of 20 ms has been assumed unless otherwise noted, a correlator spacing of 0.1 chip together with a code tracking loop noise equivalent bandwidth $B_N = 5$ Hz. Figure 3.99 depicts the behavior of the Galileo E1 OS signals thermal noise code delay tracking jitter testing the DP discriminator as well as the coherent and noncoherent EML and EMLP discriminators. On the other hand, Figures 3.100 and 3.101 show the tracking performance with the same parameters but for different front-end bandwidths. It is worth noting that considering a 16 MHz bandwidth instead of 4 MHz brings an additional margin of 8 dB-Hz weaker signal tracking. On the other hand, the choice of 24 MHz bandwidth instead of a 16 MHz bandwidth yields no significant improvement even for low CNR.

Looking at the thermal noise code delay tracking jitter as a function of the FE bandwidth for a low CNR value equal to 25 dB-Hz as shown in Figure 3.102, it can be
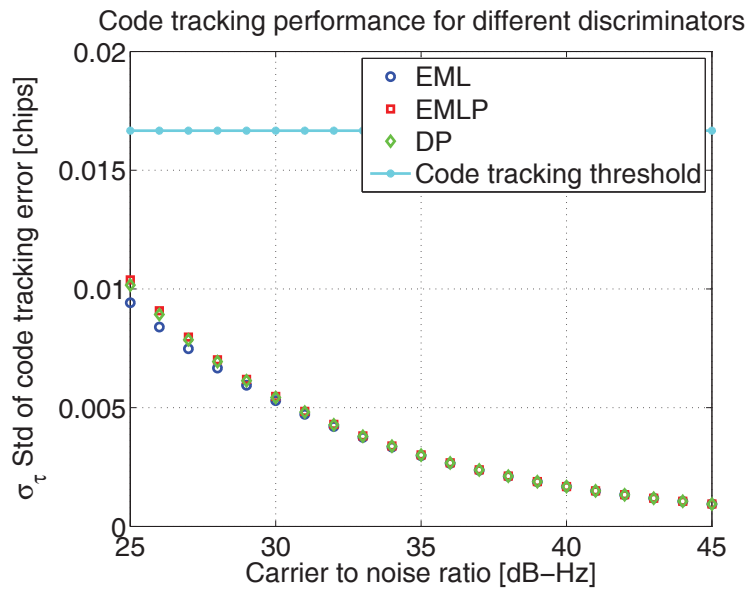
Figure 3.99: Comparison of Galileo E1 DLL tracking jitter performance as a function of CNR with different PD - using a correlator spacing of 0.1 chip and a front-end bandwidth of 24.552 MHz.

Figure 3.100: Comparison of Galileo E1 DLL tracking jitter performance as a function of CNR using coherent EML discriminator - for different front-end bandwidths.

Figure 3.101: Comparison of Galileo E1 DLL tracking jitter performance as a function of CNR using noncoherent EMLP discriminator - for different front-end bandwidths.

noticed that using an integration time of 20 ms and selecting a 16 MHz FE bandwidth instead of 4 MHz brings the standard deviation of the code tracking error down by 0.07 chips or 20 meters. It is also important to note that the usual 4 MHz bandwidth is not enough to respect the rule of thumb code tracking threshold. Increasing the integration time to 80 ms as shown in Figure 3.103, results in a lower overall code tracking jitter and selecting a 16 MHz FE bandwidth vs 4 MHz brings the code tracking error down by 0.015 chips or 4 meters. Increasing the FE bandwidth beyond 16 MHz does not bring any significant change.

In conclusion, it has been shown that for Galileo E1 OS signals, selecting a minimum of 16 MHz bandwidth instead of a 4 MHz bandwidth, provides an additional 8 dB-Hz weaker signal tracking. Moreover, selecting this wider bandwidth ensures that the rule of thumb code tracking threshold condition is met for very low CNR signals with an appropriately selected integration time. In fact, increasing the integration time lowers the standard deviation of the code tracking error, but does not guarantee tracking robustness if the FE bandwidth is not wide enough.

Figure 3.102: E1 weak signal DLL tracking jitter as a function of FE bandwidth using an integration time of 20 ms - with a C/N_0 of 25 dB-Hz considering a noncoherent EMLP discriminator.
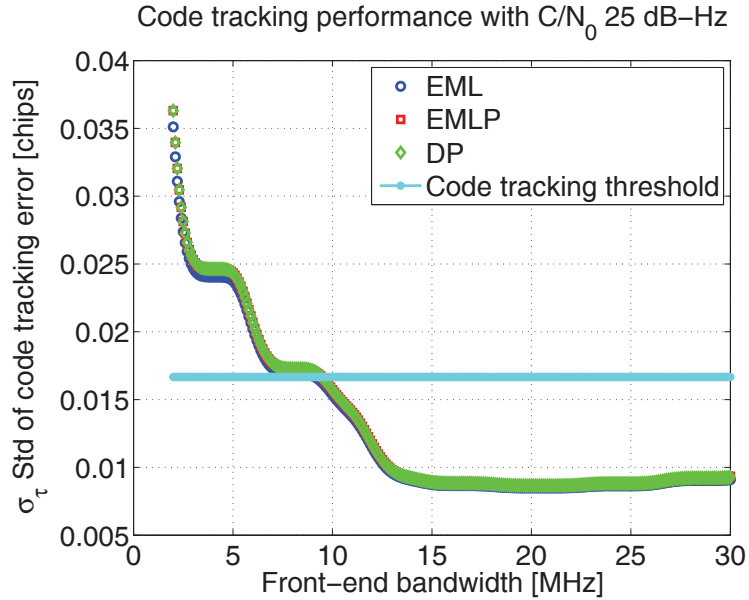
Figure 3.103: E1 weak signal DLL tracking jitter as a function of FE bandwidth using an integration time of 80 ms - with a C/N_0 of 25 dB-Hz considering a noncoherent EMLP discriminator.

3.6.3.2 Galileo E5a/b OS signal

Similarly to the Galileo E1 OS signal, the thermal noise code delay tracking jitter is analyzed on its own ignoring the other components of the total tracking jitter σ_τ. Figure 3.104 depicts the behavior of the Galileo E5a/b OS signals thermal noise code delay tracking jitter testing the DP discriminator as well as the coherent and noncoherent EML and EMLP discriminators. On the other hand, Figures 3.105 and 3.106 show the tracking performance with the same parameters but for different front-end bandwidths. It is worth noting that considering a 20 MHz bandwidth instead of 30 MHz brings an additional margin of 1 dB-Hz weaker signal tracking. On the other hand, the choice of 25 MHz bandwidth instead of a 20 MHz bandwidth yields no significant improvement even for low CNR.
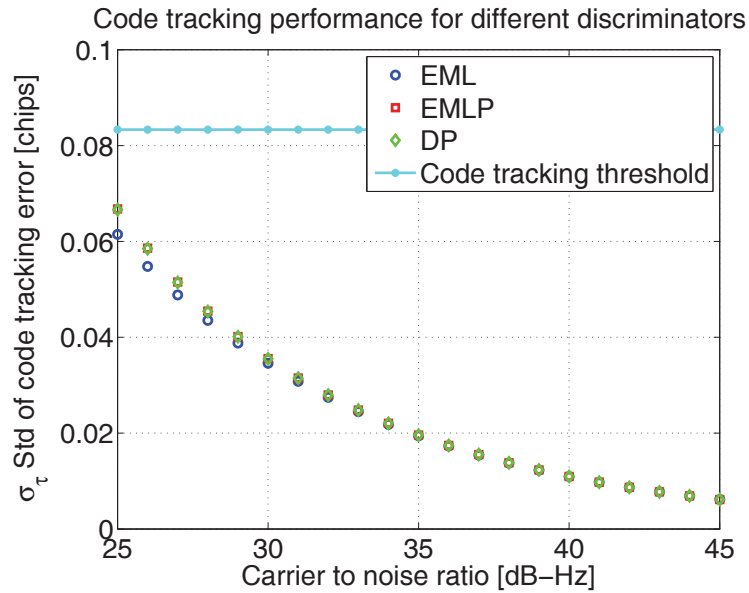
Figure 3.104: Comparison of Galileo E5a DLL tracking jitter performance as a function of CNR with different PD - using a front-end bandwidth of 24.552 MHz.

Looking at the thermal noise code delay jitter as a function of the FE bandwidth for a low CNR value equal to 25 dB-Hz as shown in Figure 3.107, it can be noticed that using an integration time of 20 ms and selecting a FE bandwidth of 20 MHz instead of 25 or even 30 MHz does not quite improve the standard deviation of the code tracking error. Increasing the integration time to 80 ms as shown in Figure 3.108, results in a lower
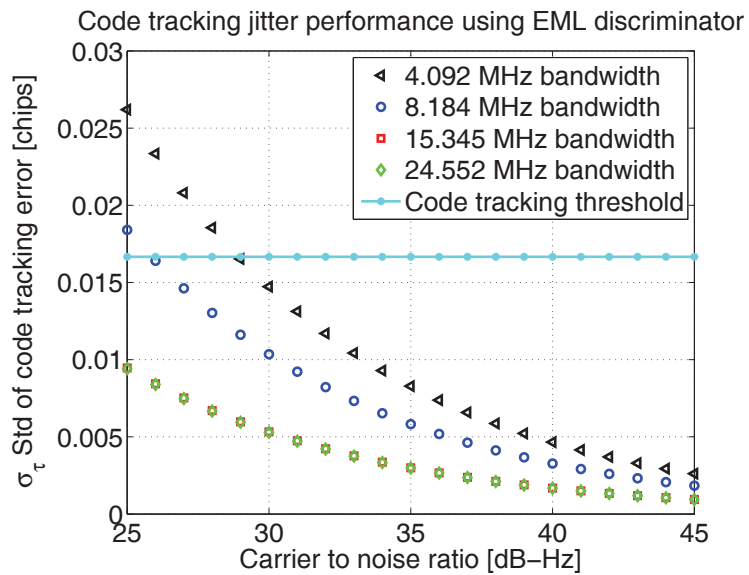
187
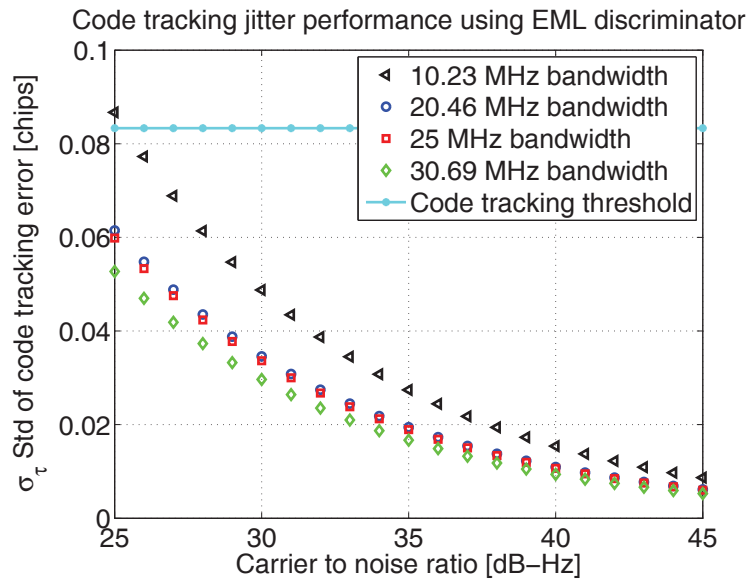
Figure 3.105: Comparison of Galileo E5a DLL tracking jitter performance as a function of CNR using coherent EML discriminator - for different front-end bandwidths.
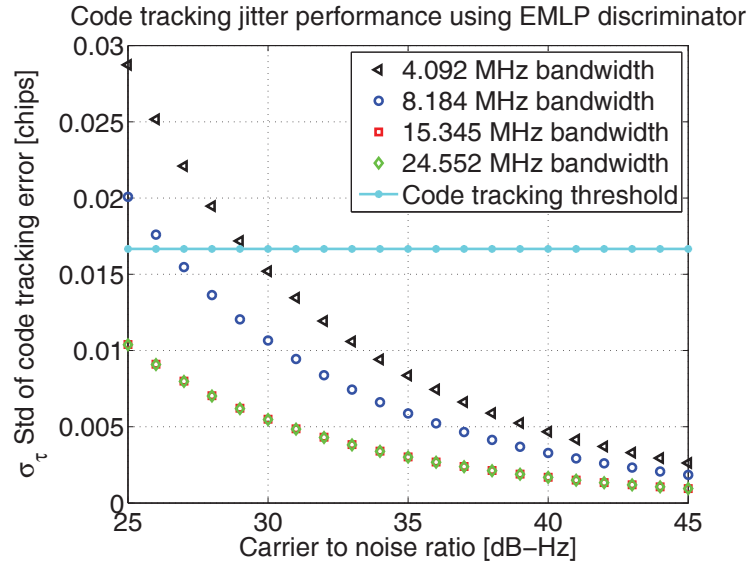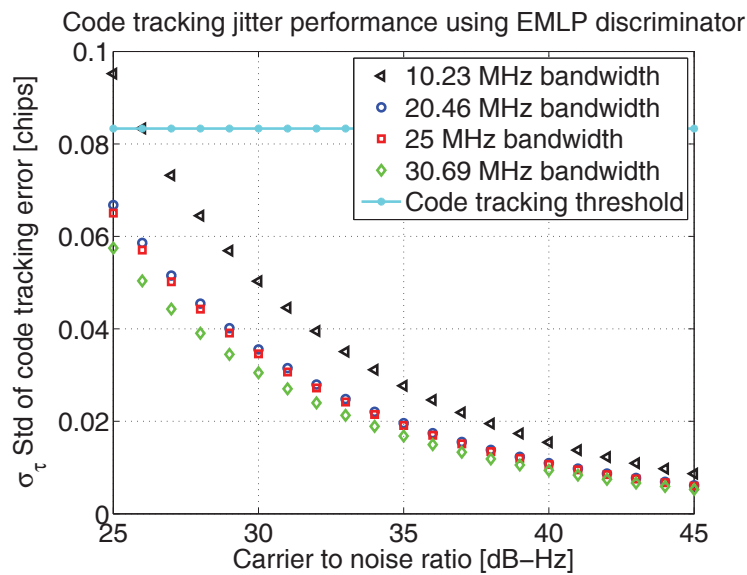

Figure 3.106: Comparison of Galileo E5a DLL tracking jitter performance as a function of CNR using noncoherent EMLP discriminator - for different front-end bandwidths.

188

overall code tracking jitter but still no significant change between a FE bandwidth of 20 MHz instead of 25 MHz or even 30 MHz.
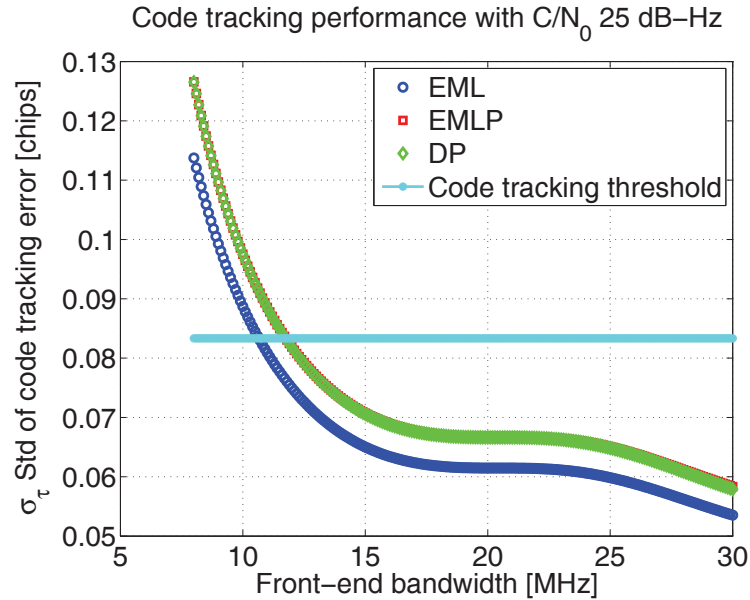
Figure 3.107: E5a weak signal DLL tracking jitter as a function of FE band-width using an integration time of 20 ms - with a C/N_0 of 25 dB-Hz considering a noncoherent EMLP discriminator.

In conclusion, it has been shown that for Galileo E5a/b OS signals, a minimum bandwidth of 20 MHz does not suffer from bandlimiting effects. Moreover, selecting this minimum bandwidth wider than 10.23 MHz ensures that the rule of thumb code tracking threshold condition is met for very low CNR signals with an appropriately selected integration time. In fact, increasing the integration time lowers the standard deviation of the code tracking error, but does not guarantee tracking robustness if the FE bandwidth is not wide enough.
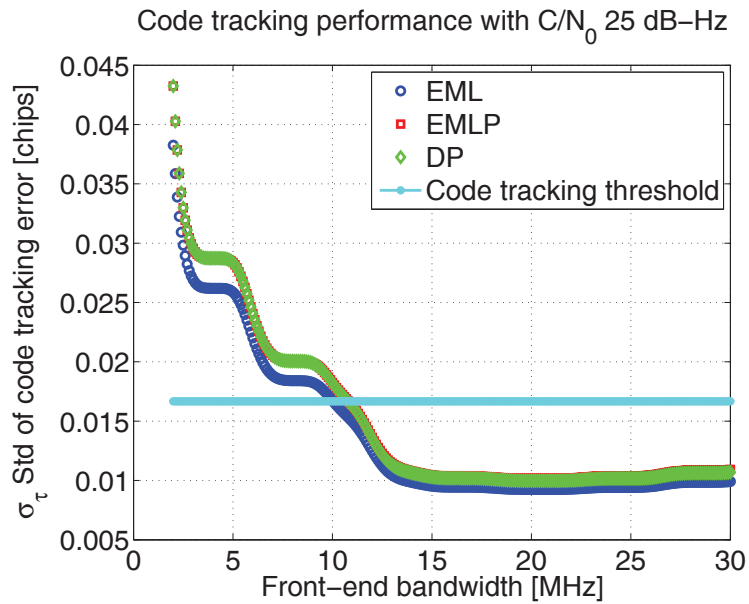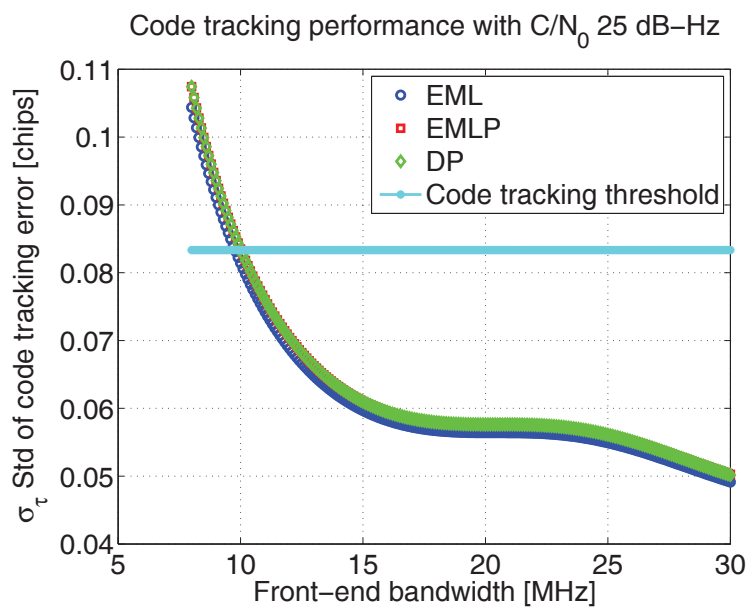
Figure 3.108: E5a weak signal DLL tracking jitter as a function of FE bandwidth using an integration time of 80 ms - with a C/N_0 of 25 dB-Hz considering a noncoherent EMLP discriminator.

Chapter 4

Applications

As more and more awareness is gained in space weather and ionosphere disturbances impact on our Earth's technical infrastructure, more interest is shed on studying the underlying physical phenomena related to the Sun's activity and consequently ionosphere scintillation. In that respect, there are many goals to be achieved on the ground, mainly to curb the potentially damaging effects of technical equipment such as electric grids or even avoid outages of GNSS which the economy and world order is increasingly dependent upon. Moreover, with the advent of new GNSS systems going towards a multi-constellation GNSS, such as Galileo and Beidou, the possibility of exploiting the availability of a big number of satellites for the end of a global ionosphere scintillation monitoring system is becoming more realistic and very much appealing.

Radio frequency signals undergo amplitude/phase/ frequency scintillation as they pass through the ionosphere region as a result of solar winds erupted from the Sun characterized by turbulent ionized gases called plasma. These ionized gases are dispersive, meaning that they have a different impact on different frequencies. Radio signals at the lower frequencies suffer more from the plasma irregularities. GNSS receivers are offering an effective tool to monitor the state of these irregularities in the sky as by recovering signals transmitted on different frequency bands from one or more of its spacecrafts. This can be achieved by monitoring the power of the recovered signal after performing carrier/code tracking and examining the resulting detrended carrier phase fluctuations. The objective of this chapter is to evaluate the performance of the tracking algorithms described in Chapter 3 using both simulation and real scintillation

GNSS data.

Tracking GNSS signals is very useful in another application involving scatterometry and reflectometry. In fact, the underlying passive potential of GNSS signals encompasses water surface identification and aircraft altimetry evaluation. This is possible thanks to the high reflectivity of L-band frequency GNSS signals on water, ice and snow covered surfaces. This high reflectivity on certain surfaces compensates for the otherwise low signal intensity and allows the detection of reflected signal components. GNSS reflectometry belongs to the class of bistatic radar systems where transmitter and receiver reside at different locations and signals pass through a reflecting surface. Code phase and carrier phase based time delay measurements between the direct path and reflected signals, are used to determine an amateur aircraft's height with respect to the reflecting surface and cm level height estimates are obtained. On the other hand, specular reflection points are computed, and a comparison of the reflected power to the direct received power is shown to yield a good water surface identification performance.

4.1 Ionosphere scintillated signals tracking

In this section, the objective is to investigate the ionosphere scintillation impact on the Galileo E1 and E5 OS signals through the comparison of CNR, amplitude and phase scintillation indices. Galileo signal simulation as well as code acquisition and tracking routines described in Chapter 2 and 3 are implemented and run in a customized Galileo simulation tool and software receiver written in Matlab ®. The scintillation indices are obtained by processing correlator and phase measurement outputs of this customized Galileo software receiver on one side, and a Septentrio PolaRxS PRO ®receiver on the other. The collection of GNSS data is carried out in an equatorial region in Ascension Islands where ionosphere scintillation is known to be a common event.

4.1.1 Tracking methodology of customized Galileo software receiver

Throughout this work, pilot channels deprived of a navigation message were considered, and thus the PLL makes use of a coherent extended arctangent discriminator to accept a wider carrier phase error. Due to the threat of ambiguous code tracking when dealing with BOC modulated signals as in the case of Galileo E1 OS signal, the

unambiguous VEMLE code phase detector is used in a two-step DLL. Galileo E5a/b signals are treated like binary phase shift keying BPSK signals when separate frequency bands are considered, and so typical BPSK DLL tracking is applied. To harness the superior tracking capability offered by BOC signals, it has been proven in Section 3.6 that a wideband front-end greater than 16 MHz is needed to capture the entire tracking capability of Galileo E1 signals. To that end, baseband complex signals are simulated and recorded with an intermediate frequency of 0 Hz and a sampling frequency of 25 Msamples/s. It is expected that Galileo wideband signals exhibit superior tracking permeability during scintillation events.

After performing acquisition and successfully solving for the secondary code delay as described in Section 2.4.1, the receiver moves to the tracking stage where an integration time of 4 ms and 1 ms are used for Galileo E1 and E5a OS signals respectively for the time being. The in-phase and quadra-phase correlator outputs are stored to estimate the CNR using the power ratio method as described in Section 2.3.3. The amplitude scintillation index is computed over an averaging interval of 60 seconds whereas the phase scintillation index over 30 seconds following the methodology presented in Section 2.3.6.

4.1.2 Tracking outputs of Galileo simulated signals

A sample Galileo E1 signal is simulated setting the input parameters to some arbitrary values, i.e. f_D = 2 kHz, A_D = -0.2 Hz/s, a code delay of 20560 chips (5 secondary chips and 100 primary chips), a CNR of 45 dB-Hz over a time duration T_g = 2 seconds. Applying the tracking scheme described in the previous section yields the results shown in Figure 4.1, where the true and estimated carrier frequency are shown during each integration interval. The total phase error is also plotted with the steady state 95 percentile yielding +/- 1.25 degrees. In addition, the DDLL tracking outputs are shown where the estimated code frequency error 95 percentile lies between +/- 1 degree. The code phase steady state error 95 percentile lies between +/- 0.1 samples. It is worth noting that the higher jitter in code phase/frequency estimation error at the beginning is due to the early coarse tracking algorithm and the transition to fine tracking results in a much lower tracking jitter. A similar tracking test with E5a/b signals is performed where carrier/code frequency and phase errors are shown in Figure 4.2.
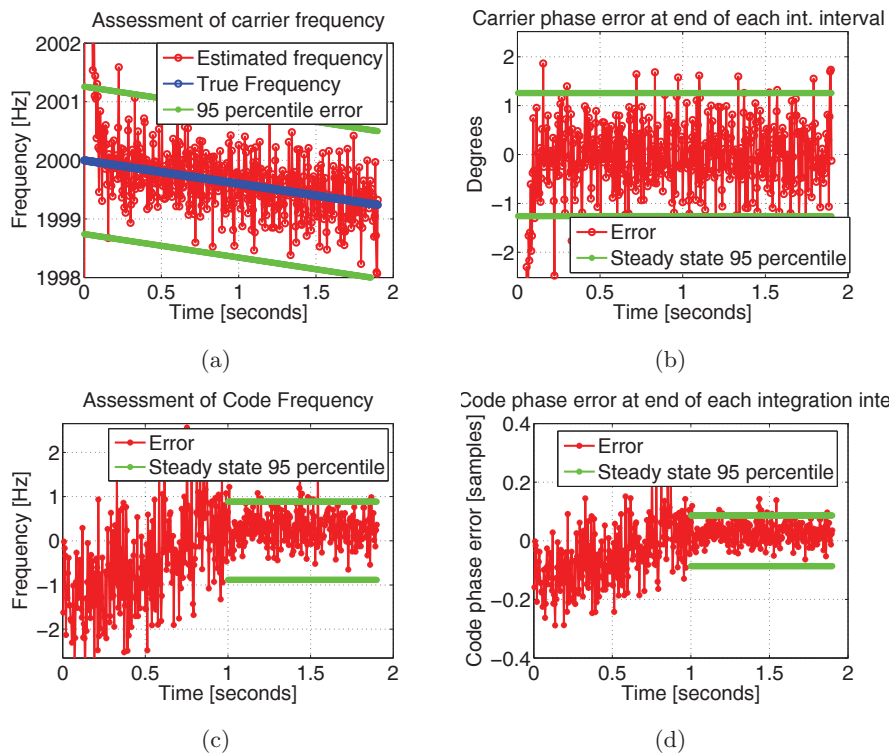
Figure 4.1: Tracking performance of simulated Galileo E1 OS signal - a) Assessment of carrier frequency b) Carrier phase error at end of each integration interval c) Assessment of code frequency d) Code phase error at end of each integration interval
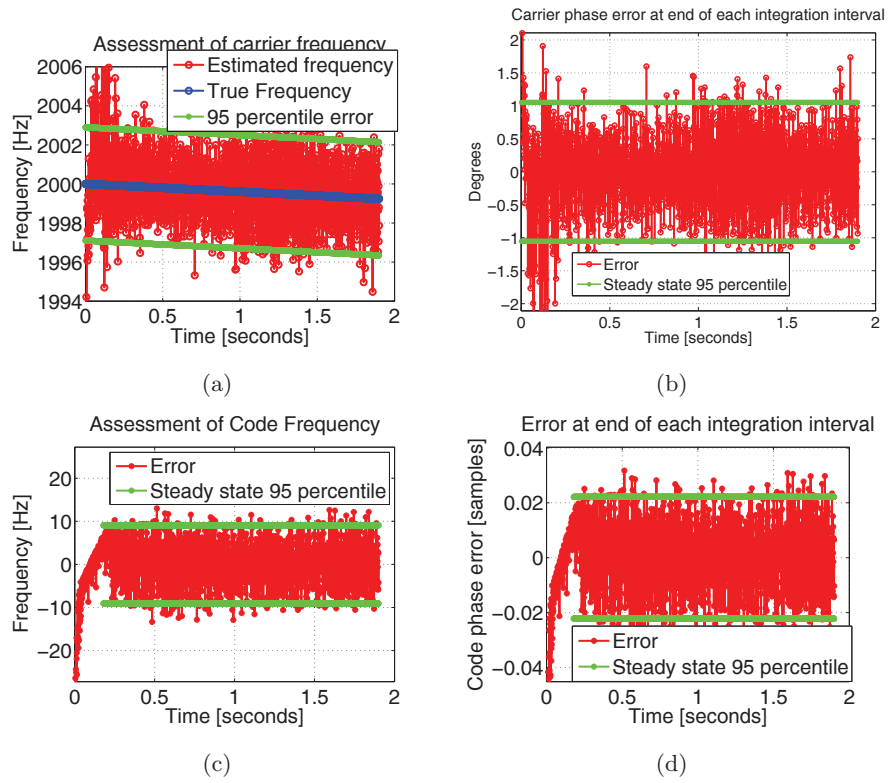
Figure 4.2: Tracking performance of simulated Galileo E5a OS signal - a) Assessment of carrier frequency b) Carrier phase error at end of each integration interval c) Assessment of code frequency d) Code phase error at end of each integration interval

4.1.3 Tracking of simulated ionosphere scintillation on Galileo E1 and E5a OS signals

In order to assess tracking performance over ionosphere scintillation signals, similar Galileo E1 and E5a OS signals are generated where the scintillation amplitude and phase time history is incorporated in the original signal as described in Section 2.3.5. The S_4 index is set to 0.8 and the channel decorrelation time τ_0 0.8 seconds. Moreover, the scintillation indices are derived using the tracking outputs, mainly the correlation values and the ADR as described in Section 2.3.6.

Figure 4.3 shows that a good estimate of the S_4 index (0.55-0.7 compared to 0.8) is reached at every minute for both frequency bands. An accurate estimate of 0.8 is not possible because of the statistical nature of the input signal due to both noise and scintillation history. The impact of the tracking loop itself is also not to be discarded [50]. The S_4 estimate discrepancy between the E1 and E5a frequency bands ranges between 0.02 and 0.1. On the other hand, a τ_0 value of 0.8 results in a $\sigma_{\Delta\phi}$ estimate in the range of 0.4 to 1 radians. The theoretical $\sigma_{\Delta\phi}$ range between 0.4 and 0.7 radians is computed using the standard deviation of the scintillation phase time history for every 30 seconds and a good estimate is evaluated on both frequency bands (almost the same) with an error in the range of 0-0.5 rad. The first two minutes $\sigma_{\Delta\phi}$ outputs are discarded due to the ADR detrending filter transient.

4.1.4 Tracking of real ionosphere scintillation affected Galileo E1 and E5a OS signals

Experimental GNSS data has been collected on the 7th to 10th of March 2013 at Ascension Island which is located in the Equatorial region at a longitude of 14.4° W and latitude of 7.9° S. The data collection has been performed using flexible and reconfigurable Universal Software Radio Peripheral (USRP) devices, the USRP N210 acting as an RF front-end. A common antenna, the Novatel GPS-703-GGG wideband antenna is shared among five different USRPs acting on different frequency bands to collect GPS, Galileo E1 and E5, GLONASS, and Beidou data. In fact, an 8 way splitter delivers the same data to five USRP N210 and a Septentrio PolaRxS which houses an oven controlled crystal oscillator (OCXO) characterized by low noise on the phase measurements. The OCXO timing signal is distributed to the various USRPs through an 8
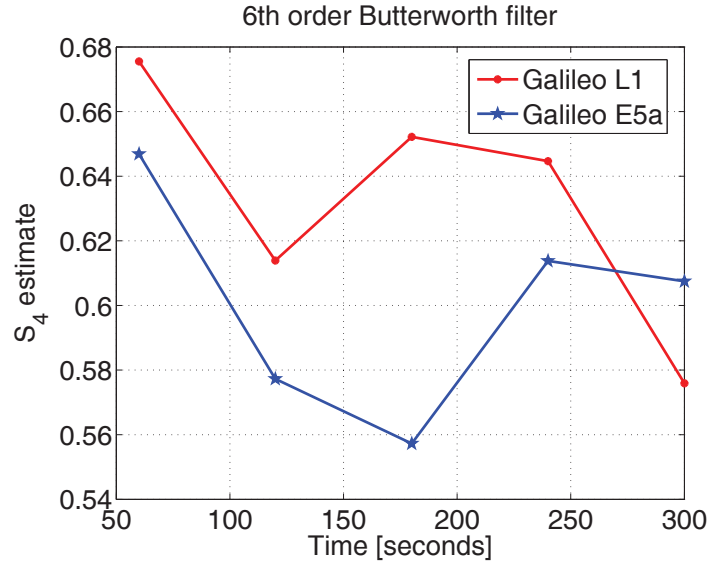
(a) Amplitude scintillation index
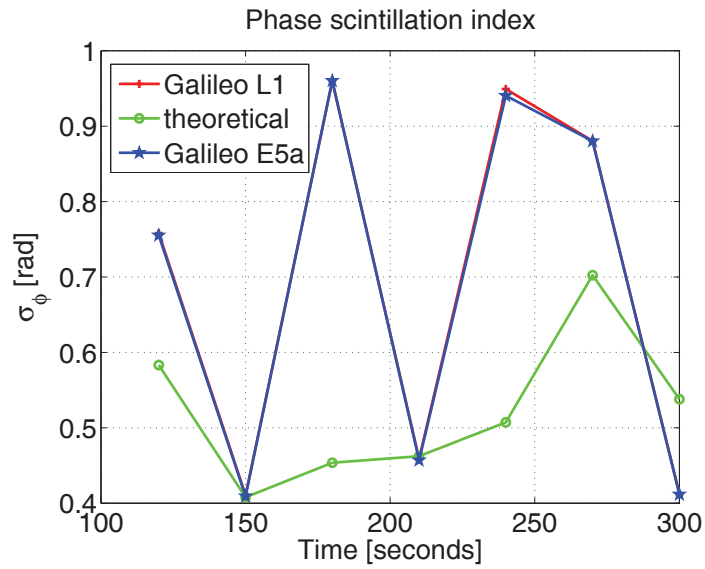
(b) Phase scintillation index

Figure 4.3: Estimated scintillation indices of a simulated scintillation signal - with an S_4 intensity of 0.8 and a τ_0 value of 0.8 on top of Galileo E1 and E5a OS simulated signals

way passive splitter. The USRP N210 sampling frequency is set to 25 Msamples/s and delivers a complex signal such that the effective sampling frequency is 50 Msamples/s. The Septentrio tracking outputs (I/Q correlator values and ADR) are saved and used to generate the S_4 and $\sigma_{\Delta\phi}$ indices as well as the CNR values for a later comparison with those obtained using the tracking outputs of a customized receiver as designed and described in the previous chapters.

It is shown in Figure 4.4 that considering the same SV with PRN 19 and processing two Galileo frequency bands E1 and E5a, the comparison between these outputs is fairly satisfying. It can be seen from Figures 4.4 a) and b) that the amplitude scintillation is stronger on the lower frequency E5a band rather than E1; similarly Figures 4.4 c) and d) show that the phase scintillation is stronger on the E5a band, and Figures 4.4 e) and f) underline the possibility of losing lock after going to very low CNR values. Similar plots can be obtained for SV with PRN 20, where the scintillation is found to be of significantly lower intensity. In fact, this can be seen in Figure 4.5 where a proportional relationship is found between the scintillation indices S_4 and $\sigma_{\Delta\phi}$ on two frequency bands, the E1 and E5a bands and for different visible satellites.

It is worth mentioning that during the data collection on March 10 2013, SV 19 was following a path going from west to east with an elevation in the range of 30-40 degrees. This can be seen in Figure 4.6 and 4.7 where a skyplot of the Galileo SVs is color coded according to the ionosphere scintillation indices S_4 and $\sigma_{\Delta\phi}$ as detected on the E1 frequency band. Similarly SV 20 was following a path going from west to east, passing almost through the same point in space as SV 19 with a delay of 2.5 hours, but from then on with a steadily decreasing elevation angle from 50 to 15 degrees. These are the key situations where the scintillation phenomenon can be studied with a time resolution determined by the GNSS satellites path. Unfortunately, the Galileo SV with PRN 11 became visible during only a short period of time, with an elevation angle less than 15 degrees, and so had to be neglected. Finally Galileo SV with PRN 12 had an interesting path starting from an invisible state to an increasing elevation from the horizon to a maximum of 40 degrees always in the west part of the sky and even passing almost through the same point in space as SV 19 with a delay of 2 hours. It can be thus concluded that in the same region of space the scintillation intensity becomes considerably higher further later in time, after comparing the performance of PRN 19
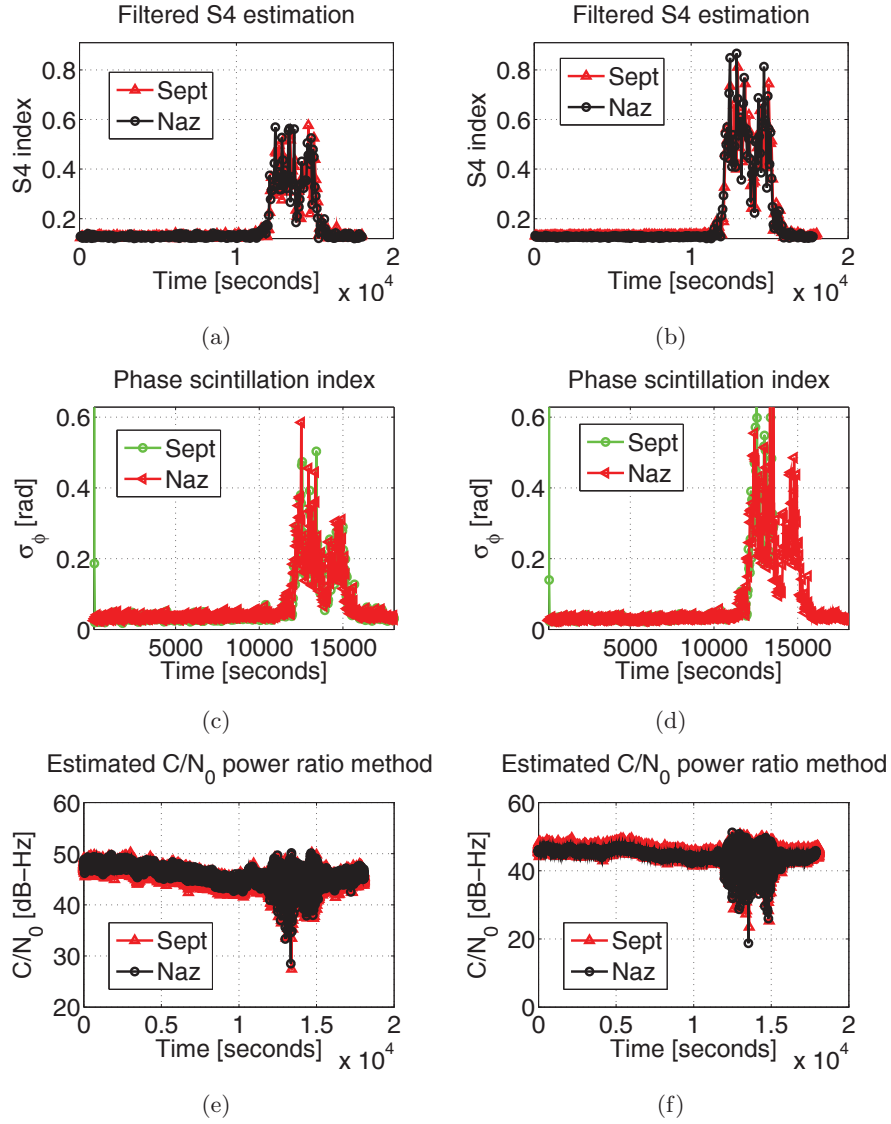
Figure 4.4: Estimated scintillation indices and CNR of real Galileo E1 and E5a frequency bands for PRN 19 - a) Amplitude scintillation index on E1 b) Amplitude scintillation index on E5a c) Phase scintillation index on E1 d) Phase scintillation index on E5a e) CNR estimate on E1 f) CNR estimate on E5a.
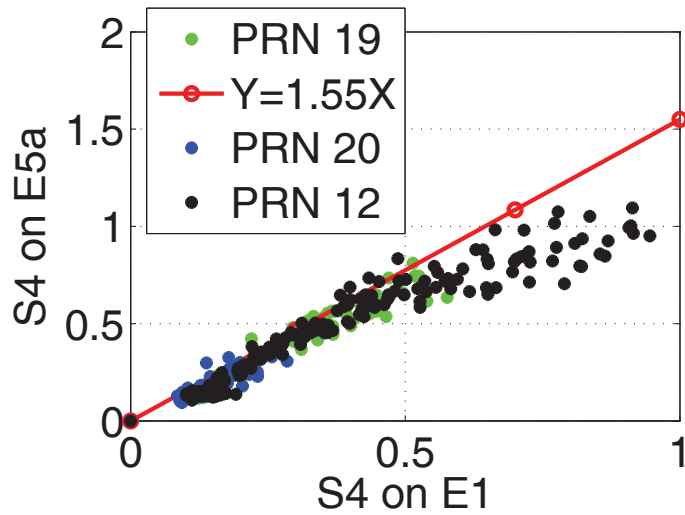
(a) Amplitude scintillation relationship on two Galileo frequency bands
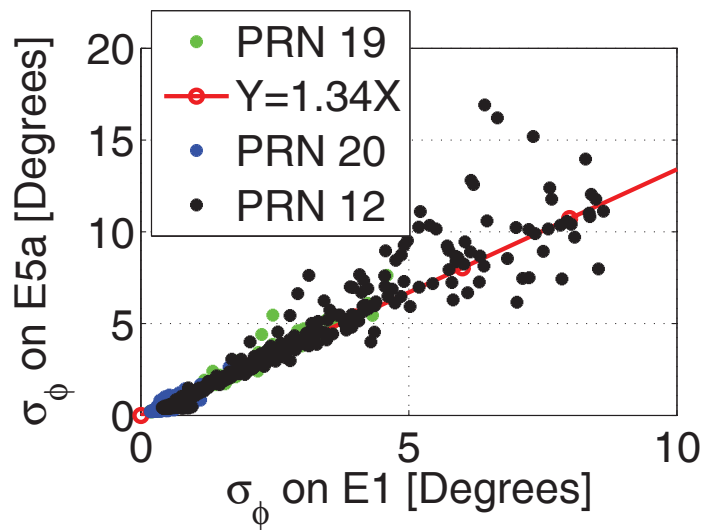
(b) Phase scintillation relationship on two Galileo frequency bands

Figure 4.5: Comparison of estimated scintillation indices on two Galileo frequency bands and three Galileo satellites - on March 7 2013 in Ascension Island using a customized Galileo receiver.

vs PRN 12 as can be seen in Figures 4.5 as well as the skyplots shown in Figures 4.6 and 4.7. The black color in these plots indicates instances where tracking has been interrupted to avoid wrong estimation of scintillatin indices.
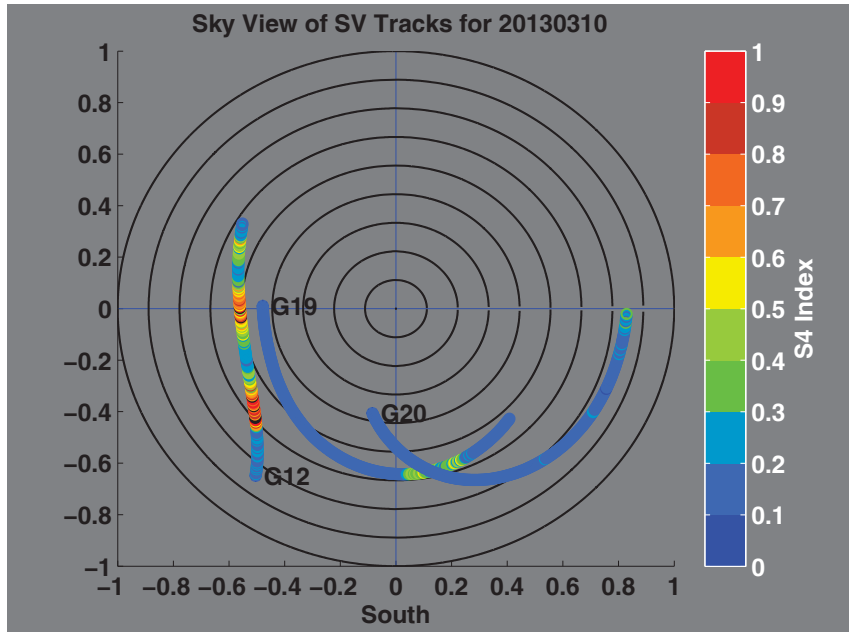
Figure 4.6: Ascension Island skyplot of Galileo satellites showing amplitude scintillation index - during the night of March 10 2013.

4.1.5 Conclusion

Space weather effects, mainly amplitude and phase scintillation impact has been shown on recently collected UHF Galileo OS signals tracking as these signals passed through the ionosphere and reached Ascension Island, an equatorial region. It has been seen that the recently launched four Galileo satellites add further observability to the existent block of GNSS satellites in view of a better time resolution in ionosphere scintillation monitoring. Exploiting the full wide-bandwidth offered by the E1 and E5a Galileo signals, carrier/code tracking has been tested on simulated signals with and without amplitude/phase scintillation and performed on real Galileo signals as well. Scintillation indices on three Galileo visible satellites during data collection have been computed and compared to the indices generated by the tracking outputs of a professional Septentrio
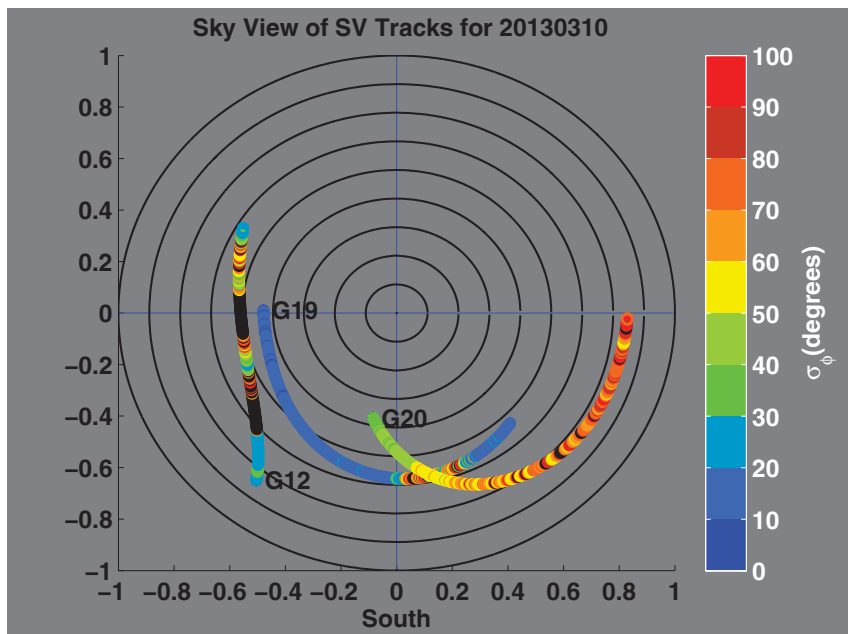
Figure 4.7: Ascension Island skyplot of Galileo satellites showing phase scintillation index - during the night of March 10 2013.

PolaRxS PRO scintillation receiver. Finally, the empirical relationships of the scintillation indices between different frequency bands have been verified with real Galileo signals on the E1 and E5a bands.

4.2 Carrier phase measurements in dynamic conditions

GNSS (GPS, Galileo, GLONASS) reflectometry belongs to the class of bistatic radar systems which can be used as a tool for Earth remote sensing purposes. In a bistatic configuration, transmitter and receiver reside at different locations. The receiver passively uses emitted signals of sources of opportunity. Beside the direct line-of-sight signals, a GNSS reflectometry receiver can potentially use all GNSS signals that are reflected from the Earth's surface. As the GNSS signals are transmitted continuously, the receiver is allowed to perform continuous measurements of the reflecting surface. Part of the transmitted GNSS signal is absorbed by the reflecting surface while the rest is usually scattered in different directions including the receiver's direction where signals are captured with a certain power, and phase shift. In fact, the reflected signal

arrives at the receiver with a certain time delay compared to the direct signal.

This time delay herein, is estimated to carry out two purposes: a surface characterization below a flying aircraft and an altimetry study of the aircraft itself. The aircraft is equipped with two GNSS receivers, a Right Hand Circularly Polarized (RHCP) antenna for direct signal reception and a Left Hand Circularly Polarized (LHCP) antenna for reflected signal reception. In fact, as the roughness of a reflecting sea surface scatters the energy pattern of the reflected signal, significant surface characterization can be derived from the temporal waveform development of the received reflected signal. Observations of this kind belong to the field of GNSS scatterometry [51, 52, 53].

Moreover, the time delay between direct and reflected received signals determines the height of the receiver with respect to the specular reflection point (the point visited by the shortest reflected path). This is possible thanks to simple geometric considerations which yield the receiver height as a function of time delay due to different signal paths and the satellite elevation angle with respect to the receiver horizontal plane. Observations of this kind belong to the field of GNSS altimetry [54, 55].

The precision of altitude estimation can further be driven down to cm level if GNSS carrier phase measurements are implemented [56]. To that end, mixed least square estimation is performed using both code and carrier phase measurements on a single frequency to compute float type ambiguities inherent in carrier phase measurements. Integer ambiguities are then estimated using the lambda method [57] and finally the integer ambiguities are used to compute the fixed height at each instant using exclusively carrier phase measurements. Software receivers are essential tools in this type of application, because they are able to process GNSS signals in real time. Moreover, they are able to store in memory the raw samples at the output of the RF front-end for post mission analysis.

In this work, a bistatic GPS receiver is used to mainly identify inland waters such as lakes, rivers and rice fields immersed in water, but also to precisely estimate the altitude of an aircraft flying over these water surfaces. The innovative aspects of this work reside in the ability of carrying out altimetry measurements in dynamic conditions

as well as in the usage of a low cost front end to perform the experiment. In fact most of the altimetry studies reported in the literature have been done in static conditions and with a very expensive equipment [58, 59].

4.2.1 Experiment description and considerations

The set-up design, shown in Figure 4.8, has a primary task which consists in combining the RF signal received from a zenith looking RHCP antenna to that received from a nadir looking LHCP antenna. The combined RF signal is then sent to a low cost, commercial front end, that converts the signal in digital format and downsamples it to an operating IF. The combiner's task is to merge into a common stream of samples, both direct and reflected signals. Traditional set-up approaches (as the one reported in [60]), on the other hand, use a common clock to sample both the direct and the reflected signals that are split on separate channels. With this approach, the two signals can be easily processed separately (without losing synchronization) but it requires a common clock for the two RF channels and a custom design of the RF part which is expensive. Instead, adopting the simple approach shown in Fig. 4.8, the design of the RF part is trivial pushing the challenge to the software receiver side by implementing ad-hoc algorithms for the detection and analysis of the reflected signals, as they are mixed with the direct ones.

The low cost front end is carried on board of a small aircraft and a laptop running a fully GPS software receiver has been used to perform a data collection during the flight. The flight route was planned to pass over lakes, rivers and rice fields in the Piedmont region in Italy. An offline post processing analysis has been carried out on the data stored during the flight. Two different analyses have been conducted. The first is focused on the detection of water surfaces, while the latter consists in measuring the aircraft's altitude.

Given the limited position accuracy offered by code phase measurements, carrier phase measurements are harnessed in this paper to reach a better position and height accuracy. In fact, code and carrier phase measurements are typically affected by a noise variance of the order of m and cm respectively. To that end, the Precise Point Positioning (PPP) technique is implemented operating on a single receiver's carrier phase measurements to obtain centimeter level accuracy height. The challenge for PPP consists in cancelling
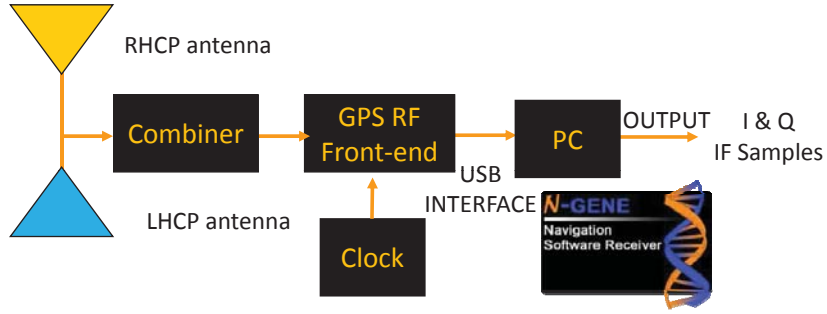
Figure 4.8: Data collection setup

out propagation and timing errors without performing double differences as can be done in relative positioning where normally an additional receiver acts as the reference point. The basic model of the true range r in meters between satellite and local receiver using code and carrier phase measurements ρ and ϕ, is expressed by Equations (4.1) and (4.2), where errors due to the ionosphere I, troposphere T, receiver clock bias δt_u, satellite clock bias δt_s and multipath and receiver noise on code and phase measurements ϵ_ρ and ϵ_ϕ are considered [61]:

$$\rho = r + I + T + c(\delta t_u - \delta t^s) + \epsilon_\rho, \tag{4.1}$$

$$\phi = \lambda^{-1}[r - I + T] + \frac{c}{\lambda}(\delta t_u - \delta t^s) + N + \epsilon_\phi. \tag{4.2}$$

and λ is the signal wavelength whereas c is the speed of light. It can be assumed that ionospheric, tropospheric, receiver and satellite clock biases are almost fully cancelled in such a reflectometry experiment where direct and reflected signals go through the same initial path as they are transmitted from the satellites. Carrying out simple geometrical analysis, at each instant of time, it is easy to express $\Delta\rho$ and $\Delta\phi$ single difference measurements between direct and reflected signals in terms of the time delay $\Delta\tau$ between direct and reflected signals as well as the receiver height over the reflecting surface as shown in [62].

$$\Delta\rho = c\Delta\tau = 2h \cdot \sin(\psi) + \epsilon_\rho \tag{4.3}$$

where ψ is the satellite elevation angle with respect to the horizontal plane at the receiver. The carrier phase measurement, on the other hand, measures the delay between

the direct and reflected signals up to an integer number of cycles N.

$$\Delta\phi = 2h \cdot \sin(\psi) + N \cdot \lambda + \epsilon_\phi \qquad (4.4)$$

It is worth mentioning that the time delay is easily computed exploiting the properties of GNSS signals, that is by computing the time delay between the correlation peaks of direct and reflected signals. In addition, estimating the height using Equations (4.3) and (4.4) in a least squares sense raises several simplifying assumptions. It is thus assumed that satellite elevation angle is already estimated with a good quality, that the receiver noise and multipath propagation error due to many reflection points are not significant. And finally, that the error introduced by the bias effects in the measured time delay is not that significant. These biases are due to possibly multiple reflection points, not just the specular reflection point, especially when the relative height above the reflection point is very high. After solving the system in the least squares sense, the height and float carrier ambiguities are estimated. To obtain integer ambiguities, the lambda method is applied and the carrier ambiguities are then fixed. Using these fixed values, the system composed of Equations (4.3) and (4.4) is again solved in the least square sense. However, only carrier phase measurements are incorporated in the system to estimate the height of the receiver over the reflecting surface at each time instant. Code phase measurements are excluded in this final step and the height estimation relies solely on carrier phase measurements.

4.2.2 Surface characterization results

As previously mentioned, the front end makes a collection of combined direct and reflected signals. It is intuitive therefore that the first task of the acquisition block is to detect the two peaks corresponding to each one of them. For scattering purposes, the next step is to track the peak corresponding to the reflected signal only, and then evaluate the carrier to noise ratio. It is concluded that the aircraft is flying over inland waters whenever the carrier to noise ratio of the reflected signal is significantly higher than the usual value when the reflecting surface is ground.

To assess the reliability of this technique, specular reflection points for each satellite in view are computed in post-processing using the method described in [63]. The specular reflection points of two satellites in view are then plotted on a map as shown in Fig. 4.9. Fig. 4.10 shows the reflected signal power as a function of time for these two satellites.
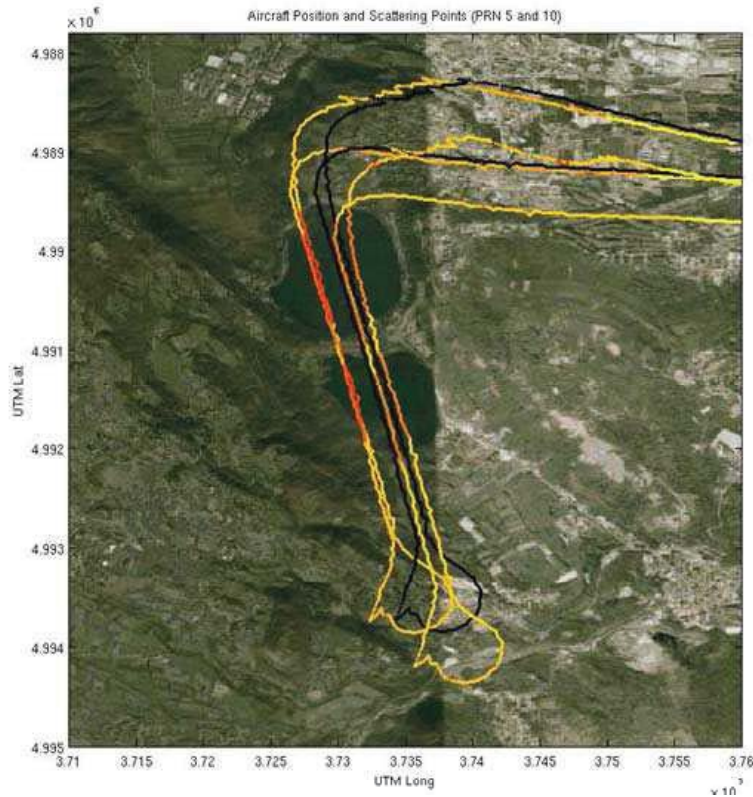
Figure 4.9: Flight route specular reflection points for two satellites.

In this way, water surfaces are identified by looking at the power level. Moreover, the power magnitude of the reflected signal was superimposed on the reflection points along the flight route as shown in Fig. 4.9. Significant high reflected power is mapped to orange/red colors while poor reflections were mapped to yellow. It can be clearly seen from Fig. 4.9 that red colors indicating the presence of water surfaces conform to the reality shown on the map. It is worth noting that we were able to identify very narrow water surfaces like rivers and canals. Moreover, in case of rice crop detection, we were able to detect the size of the rice field with a precision of less than one meter.

4.2.3   Altimetry estimation results

The second analysis regarding altimetry used both the direct and reflected signals combined together with the measurement of the delay between the two signals; it is
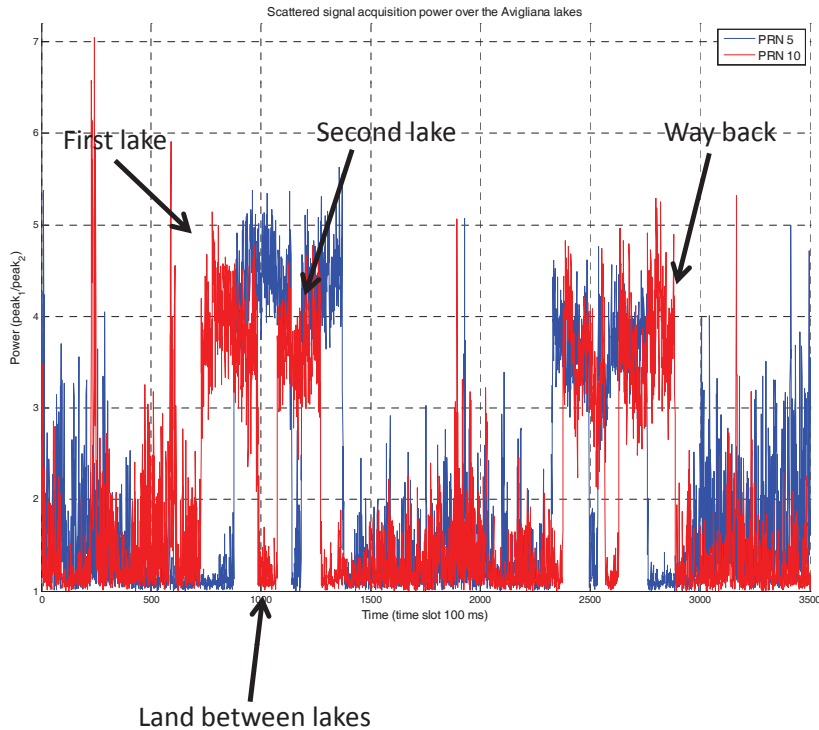
Figure 4.10: Water surface identification looking at the estimated CNR during acquisition of two GPS satellites, PRN 5 and 10.

expected that a better computation of the delay between direct and reflected signals, yields a more precise estimation of the aircraft's height above the reflecting surface. For this purpose, single frequency single difference carrier phase measurements were used and we were able to have cm level precision in the estimation of the altitude as plotted in Fig. 4.11. Such measurements were performed only when the reflected signal power was high enough and the aircraft was moving at a constant speed. This was to ensure correct tracking, avoiding the presence of cycle slips. Together with the carrier phase measurements height estimation, Fig. 4.11 also shows height estimates using single difference code phase measurements and a smoothed version or a moving average of height estimates using the direct signal code phase measurements. Comparing the latter to the estimated height using carrier phase measurements, the mean height estimation discrepancy is less than 2 meters. Moreover, the height standard deviation due to
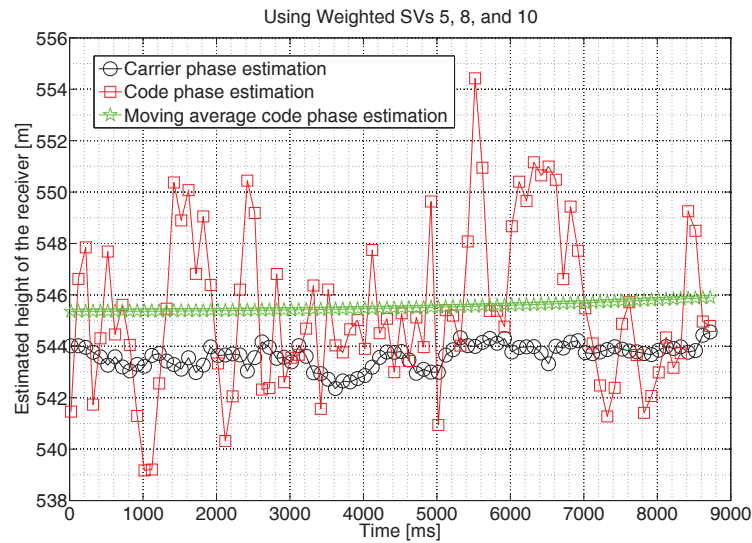
Figure 4.11: Comparison of aircraft altitude estimation over 9 seconds either using single differenced code phase, carrier phase or moving average undifferenced code phase measurements.

carrier phase measurements is less than 50 cm. This can be roughly considered a good result, however good altimetry reference measurements should be collected to assess the true nature of the errors incorporated in these height estimates using carrier phase measurements.

4.2.4 Conclusion

The preliminary results of this reflectometry and scatterometry study show fairly good performance in terms of water surface detection and aircraft height estimation exploiting direct and reflected signals off a water surface. These results are highly encouraging given that only single frequency measurements are used without any reference receiver. Further tests and analysis have to be carried out to accurately assess the system performance as well as improve height estimates using carrier phase measurements.

Chapter 5

Summary and conclusions

This research has focused on the design of pilot channel scalar tracking loop systems for high sensitivity Galileo receivers. First, an introduction of GNSS systems and the frequency plan of the multi-constellation GNSS signals is put forward. The motivation behind this work is unveiled in the need to provide LBS in indoor environments, as well as to detect ionosphere scintillation and eventually be immune towards this phenomena. A description of Galileo OS signals is then provided together with an implementation of a software simulation tool generating Galileo OS signals affected by ionosphere scintillation. Extra features of this tool permit the control of the output signal properties. The design, performance assessment and implementation of the tracking loops is carried out and tested on simulated and real Galileo signals.

Scalar tracking loops (control loops) are discrete sampling systems which require a full design in the digital domain. This is crucial in challenging signal conditions where an inevitable increase of the integration interval results in either pushing the classically designed closed loop poles towards instability or yielding an undesired type of loop response. The enhanced tracking performance brought about by optimum loop filters designed in the digital domain have been verified both theoretically and experimentally where integration intervals as high as 100 ms have yielded stable tracking performance.

The designed pilot channel scalar tracking loop is tested on simulated Galileo signals with or without scintillation using short integration intervals as well and the tracking performance is assessed. A carrier tracking frequency error of around ± 1 Hz and ± 3

is reached with Galileo E1 and E5a OS signals respectively, while a carrier tracking phase error of ± 1 degree is accomplished on both frequency bands. The code tracking frequency error, on the other hand, ranges between ± 1 Hz and ± 10 Hz for these frequency bands due to a ten times larger chipping rate on E5a signals with respect to E1 signals. Similarly, the code tracking phase error ranges between ± 0.2 samples and ± 0.02 samples for E1 and E5a signals respectively. The reason behind the 10 fold decrease is the same as that presented for the code frequency except that the effect is inversely proportional.

Including ionosphere scintillation on the simulated signals and applying the developed pilot channel tracking loop design yields close agreement of estimated scintillation indices with the true values. A tracking performance comparison between the developed tracking loop engine and a professional receiver is carried out as well, where similar results are achieved. Complete loss of tracking have not been fully analyzed in our customized receiver where successful tracking is proceeded even if going through intermittent cycle slips.

Future work will concentrate on testing the designed pilot channel scalar tracking loop with scintillation affected signals using extended integration intervals. In an effort to maintain phase lock during severe scintillation events, the afore-mentioned work will be performed both on simulated and real Galileo signals affected by equatorial scintillation. Moreover, it will be interesting to assess the performance enhancement in terms of positioning accuracy during scintillation events, due to the special measures and designs brought forth on the pilot channel tracking loop system.

Appendix A

Technique for MAT analysis using serial search and performance assessment of P2P acquisition engines

In this appendix, particular interest is expressed in the potential search space aidings received by a network of peers. To that end, the focus is on the serial TC criterion in light of the P2P context and an analysis of the MAT is performed under weak and strong signal conditions. A similar study is carried out in [13] where additional search strategies are considered as the MAX/TC criterion and the MAX search, with or without verification. The P2P paradigm consists in the exploitation of inherent communication links between nodes or peers equipped with GNSS receivers, to share and disseminate valuable GNSS information in the context of a cooperative localization. A new technical tool in the form of acquisition time and MAT diagrams is introduced which mainly serves in deriving and analyzing the MAT effectively and intuitively. In addition, an analysis is carried out with the aim of identifying the terms that contribute to the MAT, realizing that the starting cell from which the search process initiates can have an impact on the performance of the MAT. In fact, two factors are considered in the P2P acquisition engine, mainly the reduction of the search space as well as the search order. In general, the search order is assumed to be following either a uniform Probability Density Function (PDF) of starting from any cell, or a worst-

case PDF where the correct cell is scanned in the last position. A Gaussian probability distribution order is analyzed herein, taking into account the potential aiding in terms of Doppler frequency and code delay that synchronized P2P networks are able to provide. A new zig-zag search order based on P2P aidings is analyzed and an expression of the MAT contributing term due to the starting cell and zig-zag search strategy is derived. Furthermore, an example case is studied to compare uniform and Gaussian search orders with a reduced search space in the P2P context.

A.1 Acquisition and probabilities

A.1.1 Acquisition systems

An acquisition engine is mainly a cross-correlation engine coupled with a decision system. In the cross-correlation engine, the received SIS is multiplied by a locally generated signal using an estimated code delay $\hat{\tau}$ and Doppler frequency $\hat{f}_D$. The Cross-Ambiguity Function (CAF) is a two-dimensional function in terms of a combination $(\hat{\tau}, \hat{f}_D)$ and is equal to the cross-correlation evaluation for every possible cell. The total number of cells makes up the search space. This search space is reduced in certain conditions, as in a warm or hot start but even in Assisted-GNSS (A-GNSS) and P2P systems. P2P networks inherently are equipped with communication and synchronization capabilities that consent in highly accurate aiding in terms of both code delay and Doppler frequency so as to considerably reduce the search space. The serial acquisition engine will obtain most of the attention here, as the aiding provided by a P2P network is usually accurate enough to scan a few cells depending on a number of parameters. In a serial search, it is assumed that the CAF is evaluated or scanned in a starting cell and compared to an acquisition threshold (detection process). If the signal is declared present in the cell, the search process is stopped. If the signal is declared absent in that cell, the search continues by moving to the next cell, evaluating the CAF on that cell and applying the detection process cell after cell. The MAT is computed assuming that the search continues indefinitely until the signal is declared present in a particular cell. In such a setting, the concept of probability of detection and false alarm is fundamental in evaluating any acquisition time. Cell probabilities of detection and false alarm are the major players in the expression of the MAT of a serial search strategy,

however, system probabilities have a more significant behaviour in terms of the overall acquisition system.

A.1.2 Cell and system probabilities

In an acquisition system, it is important to distinguish between cell and system probabilities before conducting any study dealing with the MAT. Indeed, according to the search and detection strategy, system probabilities, cell probabilities or even both are used in the expression of the MAT. In the following, the probabilities relative to the whole detection system would be denoted by a subscript in uppercase letters i.e. the system probability of false alarm P_{FA}, detection P_D, missed detection P_{MD} and correct rejection P_{CR}, whereas those relative to a single cell would be identified by a subscript in lower case letters.

A.1.2.1 Cell probabilities

In assessing the MAT, as far as probabilities are concerned, the cell probabilities are exclusively significant in a context of a serial search. In this case, two hypotheses can be defined over each cell:

- Hypothesis H_0: the chosen cell is a wrong cell named H_0 cell or node, i.e. it does not correspond to the right code delay and Doppler frequency alignment of the received SIS and so

$$\mathrm{P_{fa} + P_{cr} = 1, | \, H_0.} \tag{A.1}$$

- Hypothesis H_1: the chosen cell named H_1 cell or node does correspond to the right code delay and Doppler frequency alignment of the received SIS and so

$$\mathrm{P_d + P_{md} = 1, | \, H_1.} \tag{A.2}$$

In case of a coherent integration, and a CAF envelope evaluated as $R = I^2 + Q^2$ (non-normalized summation of the in-phase and quadrature phase signal at the output of the correlators), the cell probabilities assume the following expressions [64]:

$$P_{fa}(B) = \exp\left(-\frac{B}{2\sigma^2}\right), \tag{A.3}$$

where B is the acquisition threshold over the search space, and σ^2 is the bandlimited noise variance given by:

$$\sigma^2 = \frac{N_0 B_{IF}}{2} H_c, \tag{A.4}$$

where B_{IF} is the IF bandwidth, $N_0/2$ is the noise spectral density and H_c is the number of samples in an integration interval T_i, i.e. $H_c = f_s T_i$ where f_s is the sampling frequency. The probability of detection, on the other hand, is expressed as [64]:

$$P_d(B) = Q_1 \left(\frac{\alpha}{\sigma}; \frac{\sqrt{B}}{\sigma} \right), \tag{A.5}$$

where $Q_1(\cdot, \cdot)$ is Marcum's Q-function and α is a parameter related to C the signal's amplitude and is given by:

$$\alpha = \frac{\sqrt{2C}}{2} H_c. \tag{A.6}$$

A.1.2.2 System probabilities

On the other hand, system probabilities are used while assessing the MAT in a context of maximum or hybrid maximum search. In this case, two hypotheses are defined, mainly:

- Hypothesis H_2: the PRN code that is being tested is actually present in the received signal, and so the probability rule is:

$$\mathrm{P_{FA}^p} + \mathrm{P_{MD}} + \mathrm{P_D} = 1, | \, \mathrm{H_2}, \tag{A.7}$$

where P_{FA}^p is the system probability of false alarm in presence of the PRN code in question. This probability is also called system probability of error P_E and represents the case where a positive affirmation of the presence of the signal is declared in a wrong cell.

- Hypothesis H_3: the PRN code that is being tested is absent in the received signal, and the system probability rule becomes:

$$\mathrm{P_{FA}^a} + \mathrm{P_{CR}} = 1, | \, \mathrm{H_3}, \tag{A.8}$$

where P_{FA}^a is the system probability of false alarm in absence of the PRN code in question.
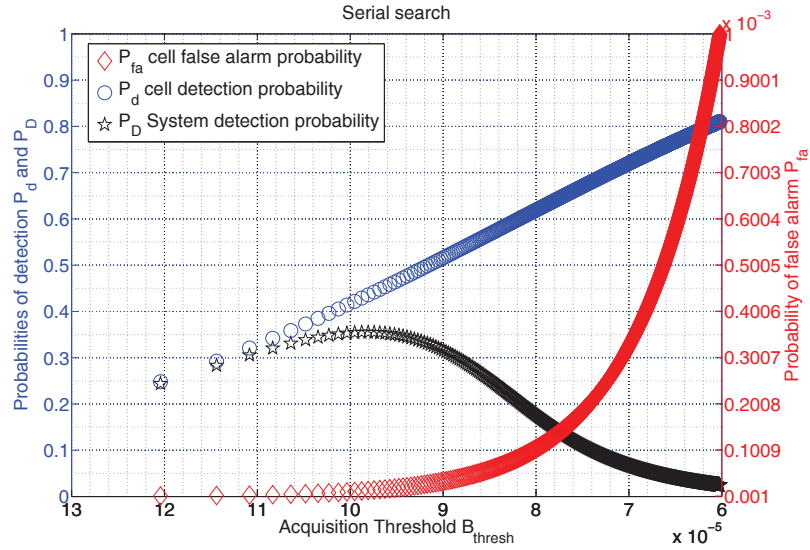
Figure A.1: Cell and system probabilities vs acquisition threshold B for a C/N_0 equal to 40 dB-Hz

In conclusion, system probabilities are more appropriate to describe the detection situation in a wider sense and as such the system P_D is used in the following analysis in conjunction with the MAT. In fact, even if the MAT of a serial search depends on cell probabilities P_{fa} and P_d, it is the system P_D that summarizes the behaviour of both cell probabilities as can be seen in Figure A.1.

A.2 Analysis of the MAT

In this section, the MAT is introduced considering the serial search TC scheme. A generic review is undertaken describing the principal method for MAT computation found in literature which is mainly based on the Probability Generating Function (PGF). A new intuitive method is devised based on time and probability-weighted acquisition time diagrams also called MAT diagrams in order to derive MAT expressions for different search orders (uniform probability, worst-case and Gaussian probability search order). Moreover, new acquisition engines, specially tailored for a P2P architecture are designed taking into considering the P2P aiding which simultaneously reduces the search space and assigns a scanning order over the cells in consideration.

A. TECHNIQUE FOR MAT ANALYSIS USING SERIAL SEARCH AND PERFORMANCE ASSESSMENT OF P2P ACQUISITION ENGINES

A.2.1 Standard acquisition engines

Standard acquisition engines using standard acquisition algorithms are considered herein. Standard, in the sense that the whole possible search space is considered with no particular hint on the scanning order of the cells or even the starting cell. Moreover, a coherent integration is used to compute the search space, and the acquisition threshold is derived as a function of the desired cell P_{fa} in order to test if the scanned cell holds the signal.

A.2.1.1 Probability generating functions

The standard serial single-dwell time search strategy consists in starting from a specific cell in the search space and serially examining the remaining cells in some arbitrary direction and order until the H_1 cell is found, the cell which contains the right PRN code with the correct Doppler frequency and code delay. In the literature, the procedure to determine the MAT for a specific scenario is to draw the decision flow graph as shown in Figure A.2, define the gain functions that consent the transition from one node to another, and finally derive the system PGF $P_{ACQ}(z)$ [28]. The MAT is then given by the flow graph technique described in [28] as:

$$E[T_A] = \left| \frac{d}{dz} P_{ACQ}(z) \right|_{z=1}. \tag{A.9}$$

The black dots in Figure A.2 called "nodes" hereafter represent the cells of the search space where there are N_c cells in total. Node (N_c) or node H_1 is designed differently from other nodes, noting that it holds the H_1 state corresponding to the H_1 hypothesis. It can be shown that the PGF corresponding to the flow graph in Figure A.2 is equal to:

$$P_{ACQ}(z) = \frac{H_D(z)}{1 - H_M(z)H_0^{N_c-1}(z)} \sum_{i=1}^{N_c} \pi_i H_0^{N_c-i}(z), \tag{A.10}$$

where the gain functions are defined as $H_D(z) = P_d \cdot z^{T_c}$ leading from node H_1 to node Acquisition (ACQ), $H_M(z) = (1 - P_d) \cdot z^{T_c}$ leading from node H_1 to an H_0 node, and $H_0(z) = (1 - P_{fa}) \cdot z^{T_c} + P_{fa} \cdot z^{T_c+T_p}$ leading from every H_0 node to the successive node where T_c and T_p are the single cell scanning time and the penalty time respectively. Moreover, π_i is the probability to start the search from cell i. Two alternatives are
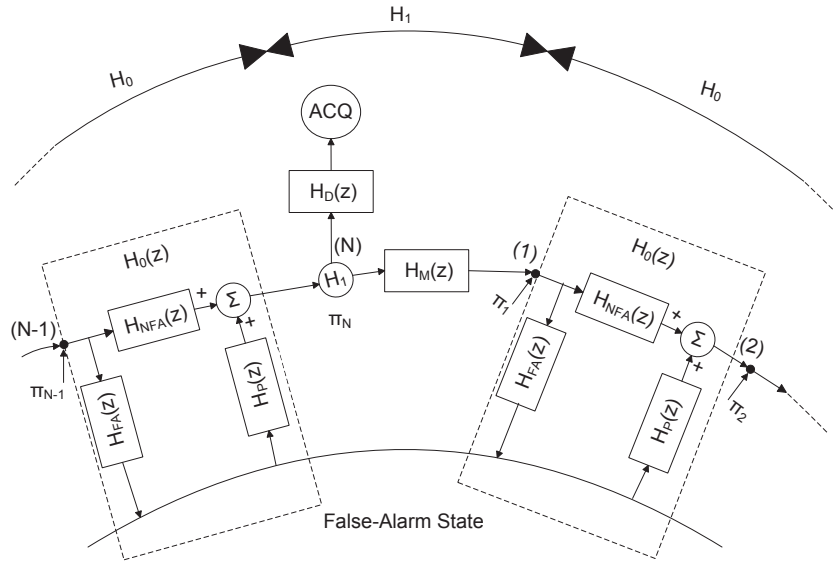
Figure A.2: Acquisition flow graph or state diagram of a standard serial approach.

considered in general, uniform probability where the probability to start from a specific cell is the same for all cells, i.e. $\pi_i = 1/N_c \ \forall i$ and worst-case probability, i.e. scanning the H_1 cell in the last position, i.e. $\pi_{N_c} = 1$ and $\pi_i = 0 \ \forall i$ [29].

A.2.1.2 Mean acquisition time diagrams

In this section, a new technique to derive the expression of the MAT is described. This technique is based on acquisition time and mean acquisition time diagrams also called probability-weighted acquisition time diagrams. The acquisition time diagram as shown in Figure A.3 describes the time it takes to move from the starting cell N_0 to the acquisition state taking into consideration every possible path. Every cell is represented by a square box with its number inside. The cells are assumed to be scanned in a clockwise direction with an increasing cell number order, until the N_c cell or H_1 cell is reached. A generic H_0 cell with a number i is shown to spend a time duration T_0 to move to the next H_0 cell with a number $i + 1$. A more detailed block diagram of the phenomenon is shown in Figure A.4 where both a false acquisition and a correct acquisition (signal is declared absent in an H_0 cell) spend T_c seconds. This
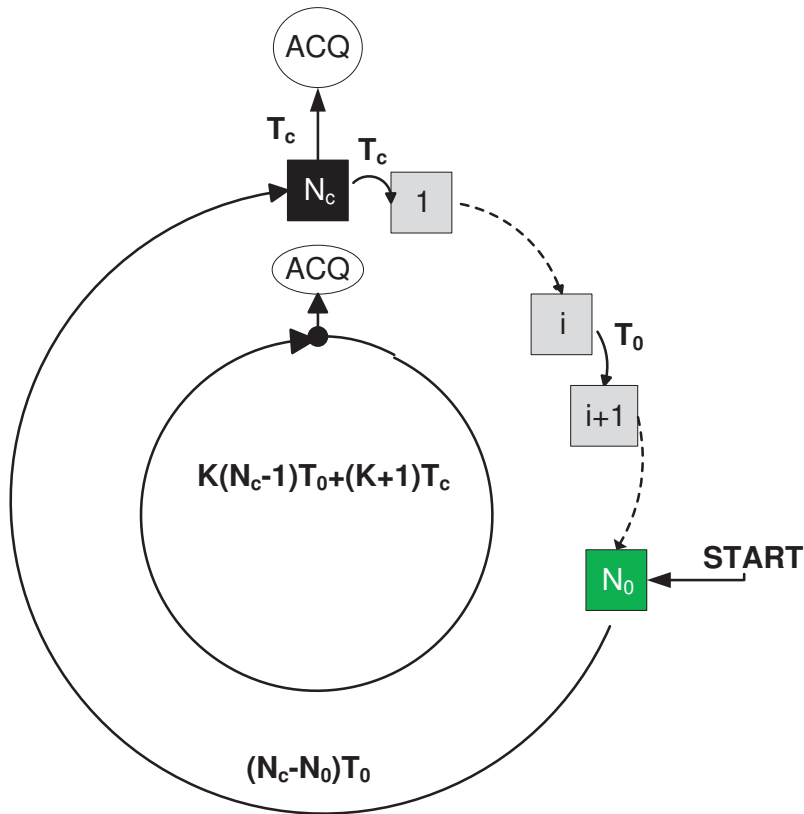
Figure A.3: Acquisition time diagram showing the time necessary to move from one cell to another across all possible paths.
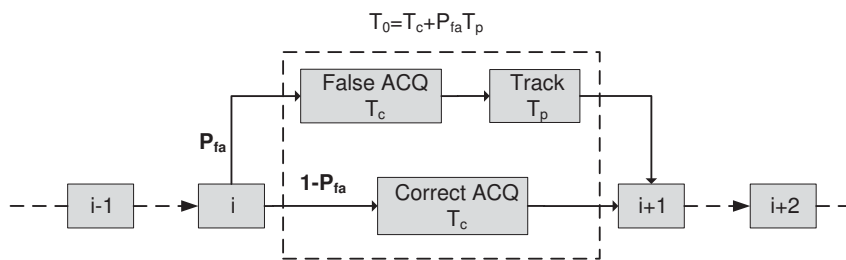
Figure A.4: Block scheme of a serial detector over two successive H_0 cells showing the false alarm and penalty time contribution to T_0.

is the time needed to test a single cell and is a function of the integration time T_i. Moreover, after a false acquisition, the system goes through a penalty time T_p in the tracking stage which is usually taken to be the tracking transient time (around 500 ms) of a successful tracking operation. In fact, the tracking block, after waiting for T_p seconds, realizes that it is not able to track the signal and moves to the next cell $i+1$. The transition time of going from an H_0 cell to a subsequent cell is T_0 seconds:

$$T_0 = T_c + P_{fa}T_p. \tag{A.11}$$

Starting from a specific H_0 cell N_0, the time spent to arrive to the H_1 cell, is represented in Figure A.5 by the outer incomplete circle as $(N_c - N_0)T_0$. Moreover, once the H_1 cell is reached, it is possible to scan the whole search space again (a complete lap) with a probability $1 - P_d$. This is represented more generically by the interior concentric circle, showing the possibility of undergoing K complete laps, i.e. $K(N_c - 1)T_0 + (K+1)T_c$ seconds before going to the acquisition state.

A.2.1.3 Deriving the MAT

The MAT becomes very intuitive looking into the MAT diagram Figure A.5, as it is only the summation of all possible paths weighted by their respective probabilities. Assuming that the start cell number N_0 can be anything between $1 \cdots N_c$ with a certain probability π_i, a summation term S is introduced which sums over all the probabilities of starting from a specific cell:

$$S = \sum_{i=1}^{N_c} \pi_i(N_c - i)T_0. \tag{A.12}$$

The MAT for a standard serial detector can thus be written in its general form as:

$$\begin{aligned}
\bar{T}_A &= S + \sum_{k=0}^{\infty} \left[k(N_c - 1)T_0 + (k+1)T_c \right] (1 - P_d)^k P_d \\
&= S + \frac{1 - P_d}{P_d}(N_c - 1)T_0 + \frac{T_c}{P_d},
\end{aligned} \tag{A.13}$$

which is obtained after noticing the presence of a simple and modified power series $\sum_{i=0}^{\infty} x^i = \frac{1}{1-x}$ and $\sum_{i=0}^{\infty} ix^i = \frac{x}{(1-x)^2}$ with $|x| < 1$.
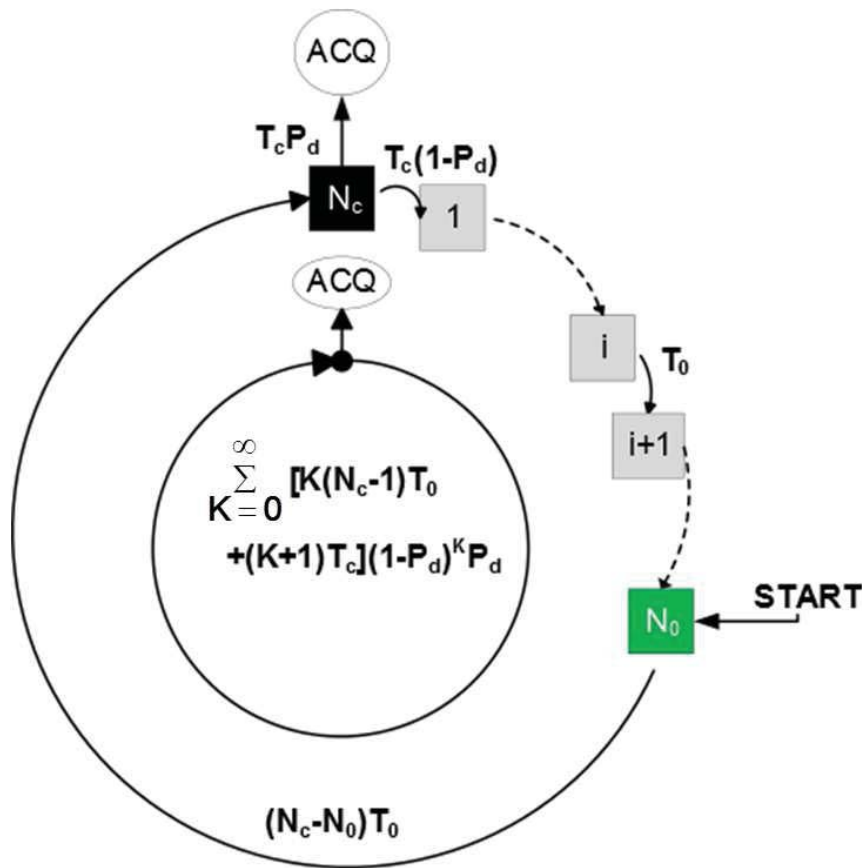
Figure A.5: Mean acquisition time diagram or probability-weighted acquisition time diagram weighting the possible paths by the corresponding probabilities, mainly P_d and $P_{md} = 1 - P_d$.

Table A.1: MAT for serial search approach

Strategy	MAT
Serial **Worst-case**	$\dfrac{1}{P_d}[T_c + (N_c - 1)(T_c + T_p P_{fa})]$
Serial **Uniform**	$\dfrac{1}{P_d}\left\{T_c + \left(\dfrac{N_c - 1}{2}\right)(2 - P_d)(T_c + T_p P_{fa})\right\}$

Equation (A.13) holds the summation term S and a constant term (constant with respect to the starting cell strategy) which is due to full laps undergone by the search process plus going to the acquisition state "ACQ". The summation term S, on the other hand, depends on the starting cell and is fundamental for studying specific starting cell probabilities as will be shown in the following. Obviously, the worst-case start cell number is 1, and the corresponding MAT can be written in the form of (A.13) with S:

$$S = (N_c - 1)T_0. \tag{A.14}$$

It is fairly easy to derive the expression of the MAT in Table B.1 corresponding to the worst-case search order by substituting (A.14) into (A.13). For a uniform probability search order, the MAT can be rewritten in the same form as in (A.13), replacing π_i by $1/N_c$ in the S factor and using the sum identity $\displaystyle\sum_{i=1}^{N_c} i = \dfrac{N_c(N_c + 1)}{2}$ such that:

$$S = \frac{1}{N_c}\sum_{i=1}^{N_c}(N_c - i)T_0 = \frac{N_c - 1}{2}T_0. \tag{A.15}$$

This is fairly reasonable as the summation term is a function of the mean of the total number of cells N_c. The expression of the MAT in Table B.1 corresponding to the uniform probability search order can be obtained after substituting (A.15) in (A.13).

A.2.2   P2P acquisition engines

The study of the MAT in P2P acquisition engines involves new acquisition approaches which exploit the aiding coming from nearby peers. The accuracy of the aiding depends on the topology and synchronization quality of the P2P network [65]. The benefit conveyed by P2P acquisition engines, stems from two factors. One is the reduced search space due to the aiding information in terms of code delay and Doppler frequency and the second is the specific order with which cells are analyzed i.e. cells most likely to hold the signal, "candidate cells", are scanned following a specific order according to the information made available by aiding peers. In this study, the first factor is analyzed by testing $L \leq N_c$ candidate cells until successful acquisition. Similar to the standalone GNSS acquisition engines, the worst-case and uniform probability search strategies indicating the cell from which to start the search are considered. Moreover, the second factor is analyzed by considering a new search order based on a Gaussian probability of finding the signal in a specific cell.

A.2.2.1   L candidate cells with uniform and worst-case search order

The serial L candidate cells search strategy exploits the reduced search space due to P2P aiding. Indeed, it is very much like the standard serial search strategy with the exception that the L candidate cells for the P2P aquisition engine are much less than the N_c total cells in the standard acquisition engine. In this case, the MAT as defined in (A.13) becomes:

$$\bar{T}_A{}^{P2P} = S + \frac{1 - P_d}{P_d}(L-1)T_0 + \frac{T_c}{P_d}, \tag{A.16}$$

where

$$S = \sum_{i=1}^{L} \pi_i (L - i) T_0. \tag{A.17}$$

Numerical figures of a possible number of candidate cells in function of the Doppler step and the code delay step are documented in [65]. It can be seen that for a time and frequency synchronized network to less than a μs and less than a tenth of Hertz, the discrepancy between pairs of receivers in the P2P architecture is of the order of a few μs and a few Hz. This translates into a few chips and most likely a single Doppler step. The number of candidate cells would then be easily derived assuming a certain code delay step and a certain Doppler frequency step which defines the resolution of

Table A.2: Search space resolution and dimensions for a 40 dB-Hz signal.

ACQ type	Δf [Hz]	R_f [Hz]	N_f	Δ_τ [µs]	R_τ [µs]	N_τ	N_c or L
Standard	667	10 000	15	1/2	1023	2046	30690
P2P	667	20	1	1/2	6	12	12

Table A.3: Search space resolution and dimensions for a 30 dB-Hz signal.

ACQ type	Δf [Hz]	R_f [Hz]	N_f	Δ_τ [µs]	R_τ [µs]	N_τ	N_c or L
Standard	56	10 000	180	1/2	1023	2046	368280
P2P	56	20	1	1/2	6	12	12

the search space. The code delay step is usually taken to be half a chip whereas the Doppler frequency step depends on the integration time given by [47]:

$$\Delta f = 2/(3T_i). \tag{A.18}$$

The P2P MAT as shown in (A.16) is a very similar expression as that found for the standard case in (A.13) with a slight difference: L cells are considered in total instead of N_c. Cell probabilities of detection and false alarm remain exactly the same as they depend on three parameters, B the acquisition threshold, α the signal amplitude and σ related to the noise variance, the last two of which are function of H_c, the number of samples in a single integration interval which remains the same. Consequently, the expression of the P2P MAT is similar to that introduced in Table B.1, except that N_c is replaced by a hopefully much smaller L. N_c and L are the result of the chosen resolution of the search space (A.18), as well as its uncertainty region (R_f in the frequency domain and R_τ in the code delay domain) as shown in Tables A.2 and A.3. Moreover, the chosen resolution of the search space is a consequence of the coherent integration time T_i, which in turn is determined by the C/N_0 of the received signal. The number of considered cells N_c or L is given by the product of the number of code delay bins N_τ and the number of Doppler frequency bins N_f, that is $N_c = N_\tau \cdot N_f$. For standard as well as P2P acquisition engines, the C/N_0 is taken to be either equal to 30 or 40 dB-Hz. Accordingly, the integration time T_i is set to 12 and 1 ms respectively such that the maximum system P_D is around 0.4 in both cases.

A. TECHNIQUE FOR MAT ANALYSIS USING SERIAL SEARCH AND PERFORMANCE ASSESSMENT OF P2P ACQUISITION ENGINES

The values of N_c and L found in Tables A.2 and A.3 are used in the expressions found in Table B.1 to obtain the plots in Figures A.6 and A.7. These plots correspond to 30 and 40 dB-Hz signals, where the system P_D is superimposed on the MAT curves of a P2P aided serial search with uniform or worst-case search order, for all possible values of the acquisition threshold B (P_{fa} is a function of B given by (A.3)). Moreover, Figures A.8 and A.9 superimpose the same curves relative to a standard acquisition engine, showing the performance increase in terms of MAT, due to the P2P aiding where $L = 12$ candidate cells are considered instead of the standard $N_c = 30690$ or $N_c = 368280$ cells of a standard acquisition engine in a cold start. It is interesting to note that the optimum acquisition threshold satisfying a minimum MAT does not correspond to the maximum system P_D as the latter does not include neither T_c nor T_p the penalty time. It can be seen that the MAT relative to the P2P acquisition engine is increased by an order of magnitude going from a strong to weak signal (40 to 30 dB-Hz) while the MAT of a standard acquisition engine is increased by two orders of magnitude in these conditions. This is assuming that the accuracy of the P2P aiding remains the same for both conditions, which is a valid assumption. In fact, the P2P aiding does not depend on the aided receiver's carrier-to-noise ratio, but rather on the aiding peers positioning accuracy and the overall network synchronization accuracy.

In conclusion, it is shown that the benefit of using a P2P acquisition engine instead of a standard one, is more clearly seen when operating on a weak signal (30 dB-Hz) rather than a strong one (40 dB-Hz). This is somehow expected as the search space size increases together with the coherent integration time which is due to a low carrier-to-noise ratio. Consequently, a good reduction of the search space coming from P2P aiding leaves the number of cells intact even if the coherent integration time increases. In this case, the performance increase in terms of MAT due to P2P aiding, differs by an order of magnitude looking at both cases of carrier-to-noise ratio.

A.2.2.2   L candidate cells with Gaussian probability distribution order

Apart from search space reduction, one of the benefits of P2P networks is the search order information. In fact, the accuracy of aiding can be exploited to determine the search order by noticing that the suggested cell by the P2P network can be considered to follow a Gaussian PDF with a mean value equal to $c_e \in \{1, 2, ..., N_c\}$ and a standard
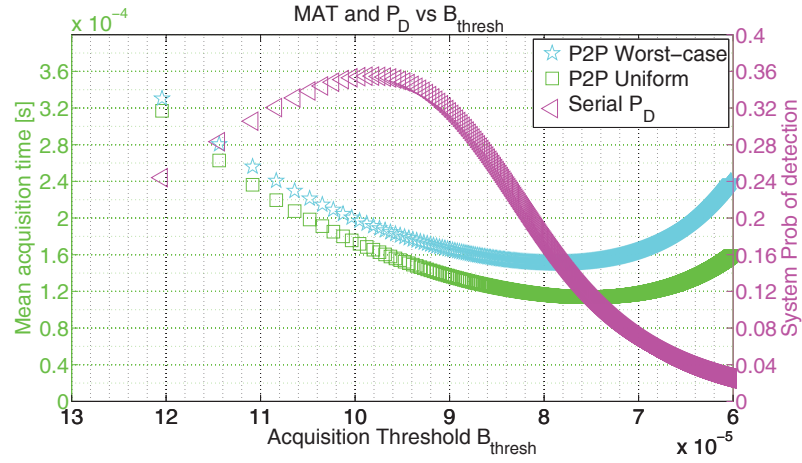
Figure A.6: MAT and P_D vs acquisition threshold for a P2P acquisition engine using a serial search in both cases of uniform probability and worst case search order with a C/N_0 of 40 dB-Hz.
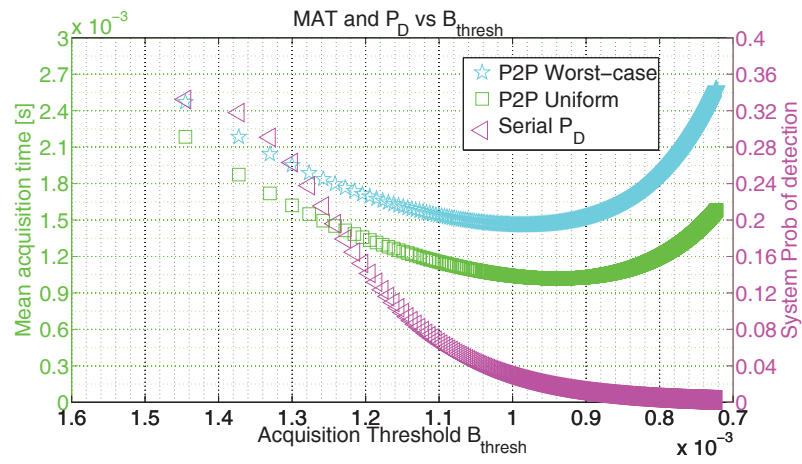
Figure A.7: MAT and P_D vs acquisition threshold for a P2P acquisition engine using a serial search in both cases of uniform probability and worst case search order with a C/N_0 of 30 dB-Hz.
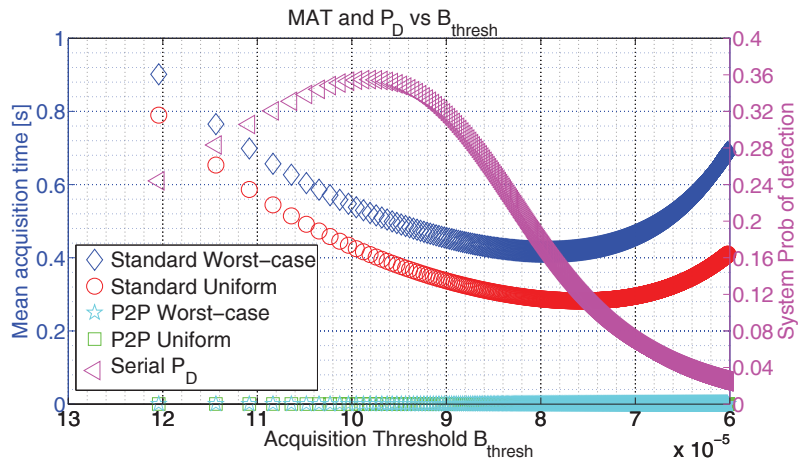
Figure A.8: Comparison of a standard serial acquisition engine to a P2P engine in terms of MAT vs acquisition threshold, with a reduced search space of $L = 12$ candidate cells in case of P2P aiding and a C/N_0 of 40 dB-Hz.
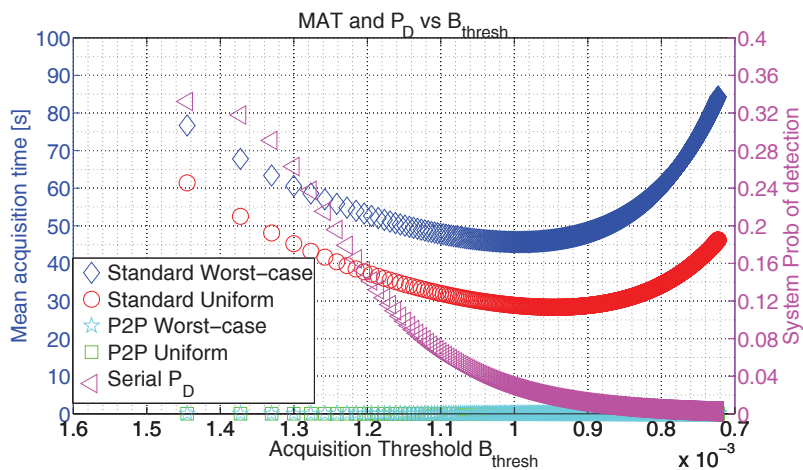
Figure A.9: Comparison of a standard serial acquisition engine to a P2P engine in terms of MAT vs acquisition threshold, with a reduced search space of $L = 12$ candidate cells in case of P2P aiding and a C/N_0 of 30 dB-Hz.

deviation σ_c (number of cells to be searched around the mean value c_e). Therefore, the acquisition strategy assumes a reduced search space of size L candidate cells, scanned in the order suggested by a truncated discrete normalized Gaussian PDF:

$$\pi_{i_j}^G = \frac{\frac{1}{\sqrt{2\pi}\sigma_c}e^{-\frac{(k_j-c_e)^2}{2\sigma_c^2}}}{\frac{1}{\sqrt{2\pi}\sigma_c}\sum_{c=c_e-\sigma_c}^{c=c_e+\sigma_c}e^{-\frac{(c-c_e)^2}{2\sigma_c^2}}} = \frac{1}{M}e^{-\frac{(k_j-c_e)^2}{2\sigma_c^2}}, \tag{A.19}$$

where M is a normalization factor, $k_j \in \{c_e - \sigma_c, \cdots, c_e + \sigma_c\}$ and i_j its corresponding cell number such that $i_j = k_j$ for $k_j \leq N_c$ and $i_j = k_j - N_c$ if $k_j > N_c$. The aiding can be biased inducing that the most likely cell to hold the signal is $c_e \neq N_c$ or can be unbiased $c_e = N_c$. On the other hand, σ_c is an integer number denoting the quality of P2P aiding in terms of number of cells to be searched to the left and right of the cell c_e. Both c_e and σ_c are function of the P2P aiding strategy. Moreover, c_j is a possible starting cell number suggested by the P2P aiding, from which the distance d_j can be computed, the number of cells distant from the H_1 cell. This distance d_j can be either positive or negative, because the cells to be searched are organized in a circular manner as seen in Table A.4. The cells in the left have cell numbers $N_c - 1, N_c - 2, \cdots, N_c/2$ and distance values $-1, -2, \cdots, -N_c/2$ while the cells on the right have cell numbers $1, 2, \cdots, N_c/2 - 1$ and distance values $1, 2, \cdots, N_c/2 - 1$. In Table A.4, the normal path c_j and an example of a P2P aiding search path are depicted, together with their corresponding distances d_j. The normal path can start from any cell from $\{1, ..., N_c\}$ and the search order is in one direction scanning subsequent neighboring cells. These cells are naturally ordered according to an increasing value of code delay and Doppler values. The P2P path on the other hand is characterized by a zig-zag search order and starts from any c_j numbered cell and scans cells $c_j - 1$, $c_j + 1$, $c_j - 2$, $c_j + 2$, etc... In the example shown in the table, it is assumed that the P2P aiding suggests values of $c_e = 98$ and $\sigma_c = 2$ assuming that $N_c = 100$ such that cell number $i_j = 100$ is the H_1 cell. It is intuitive to see that the distance d_j of a particular cell number i_j can be expressed as:

$$d_j = \begin{cases} i_j & \text{if } i_j < \lfloor N_c/2 \rfloor \\ i_j - N_c & \text{if } i_j \geq \lfloor N_c/2 \rfloor. \end{cases}$$

Table A.4: P2P search order considerations showing the number of scans p_j of an H_0 cell as a function of the cell number i_j.

Standard Path Index j	$\cdots$	$N_c - 1$	N_c	1	$\cdots$
Standard d_j	$\cdots$	-1	0	1	$\cdots$
P2P Index j	0	1	2	$\cdots$	$L - 1$
P2P Path c_j	98	97	99	96	100
P2P cell # i_j	96	97	98	99	100
P2P d_j	-4	-3	-2	-1	0
P2P p_j	8	6	4	2	0

In addition, the maximum number of scanned cells is given by L, which is typically less than N_c, as it is the size of the aiding vector $\{c_e - \sigma_c, \cdots, c_e + \sigma_c\}$. Indeed, $L = 2\sigma_c + 1$ and is always odd. Moreover, the number of scanned H_0 cells (no SIS present) prior to reaching the H_1 cell can be written as a function of d_j or even in terms of the cell number i_j:

$$p_j = \begin{cases} 2d_j - 1 & \text{if } d_j > 0 \\ -2d_j & \text{if } d_j \leq 0, \end{cases}$$

$$p_j = \begin{cases} 2i_j - 1 & \text{if } i_j < \lfloor N_c/2 \rfloor \\ 2(N_c - i_j) & \text{if } i_j \geq \lfloor N_c/2 \rfloor. \end{cases}$$

Obviously, p_j is the factor in the summation term (A.17) by which the transition time is multiplied. In this case, S is written as a function of the cell index j:

$$S = \sum_{j=0}^{L-1} \pi_{i_j}^G p_{i_j} T_0. \tag{A.20}$$

It can be noticed that this factor is expressed as an odd value for cell numbers lying on the right half-circle with respect to the H_1 cell, and as an even number for cell numbers lying in the left half-circle. The expression of the MAT becomes more intuitive when we consider that the PDF of the aiding cell is centered around $c_e = N_c$. In fact, Table A.5 shows that $p_{i_j} = j$ such that the summation term can be rewritten as:

$$S = \sum_{j=0}^{L-1} j \pi_{i_j}^G T_0. \tag{A.21}$$

230

Table A.5: P2P p_j of a simple case where cell aiding has a PDF centered around the true cell.

P2P Index j	0	1	2	3	4	$\cdots$	$L-1$
Simple P2P Path c_j	N_c	$N_c - 1$	1	$N_c - 2$	2	$\cdots$	$(L-1)/2$
P2P cell # i_j	N_c	1	$N_c - 1$	2	$N_c - 2$	$\cdots$	$N_c - (L-1)/2$
P2P d_j	0	1	-1	2	-2	$\cdots$	$(1-L)/2$
P2P p_j	0	1	2	3	4	$\cdots$	$L-1$

If L is replaced by N_c and the probabilities $\pi_{i_j}^G$ by $1/N_c$ in (A.21), a uniform probability search order is simulated for a standard acquisition engine, and the summation term S equates to:

$$S = \frac{1}{N_c} \sum_{j=0}^{N_c-1} jT_0 = \frac{1}{N_c} \frac{N_c(N_c - 1)}{2} T_0 = \frac{N_c - 1}{2} T_0, \tag{A.22}$$

which is in accordance with the expression (A.17) for a standard acquisition engine. Finally, it is worthwhile comparing the performance of the different probability search orders, i.e. uniform probability search order, Gaussian probability search order and worst-case search order. For the comparison to be fair, it is assumed that the P2P aiding includes the H_1 cell and that the Gaussian probability function is centered around it, i.e. $c_e = N_c$. Moreover, it is assumed that $\sigma_c = 6$ such that $L = 13$ candidate cells are scanned for all three strategies. Figure A.10 shows the performance in terms of MAT of a P2P serial search with the three possible search orders, assuming a C/N_0 of 30 dB-Hz. It is seen that the Gaussian probability distribution order demonstrates the best performance even if by a slight factor with respect to the uniform order. Moreover, it is interesting to study the ratio of the MAT relative to a uniform probability order with respect to a Gaussian search order:

$$
\begin{aligned}
R_{UG} &= \frac{\bar{T}_{AU}^{P2P}}{\bar{T}_{AG}^{P2P}} \\
&= \frac{\dfrac{1 - P_d}{P_d}(L-1)T_0 + \dfrac{T_c}{P_d} + \dfrac{L-1}{2}T_0}{\dfrac{1 - P_d}{P_d}(L-1)T_0 + \dfrac{T_c}{P_d} + \displaystyle\sum_{j=0}^{L-1} j\pi_{i_j}^G T_0}.
\end{aligned}
\tag{A.23}
$$

231
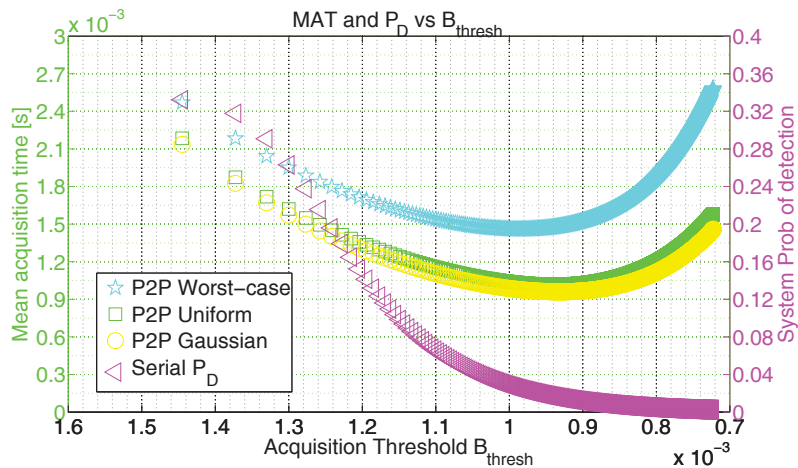
Figure A.10: Comparison of a uniform, worst-case and a Gaussian probability search orders in terms of MAT and P_D vs acquisition threshold for a P2P serial acquisition engine.

In fact, it is shown in Figure A.11 that in general, the constant component in (A.16) is greater than the S components for both a uniform and a Gaussian probability search orders. This is not true for a certain range of the acquisition threshold where the acquisition threshold is relatively low. Anyhow, as shown in Figure A.12, even if the ratio of the sums of both strategies is constant and in favour of the Gaussian probability order by a slight margin 1.11, the corresponding ratio of pMAT is even lower and approaches 1 for high acquisition threshold values. This is in accordance with Figure A.10 where the Gaussian probability search order demonstrates a slightly better performance in terms of MAT than the uniform probability order in a P2P acquisition engine.

A.3   Conclusion

The merit of P2P networks in decreasing the MAT is thoroughly explored in this appendix. The serial search TC criterion is used to derive the expression of MAT relative to standard and P2P acquisition engines. To that effect, an innovative tool is developed in the form of acquisition time and MAT diagrams which help derive, in an intuitive manner, the expression of the MAT depending on the search strategy. Furthermore, the terms contributing to the MAT are carefully analyzed and a reduced
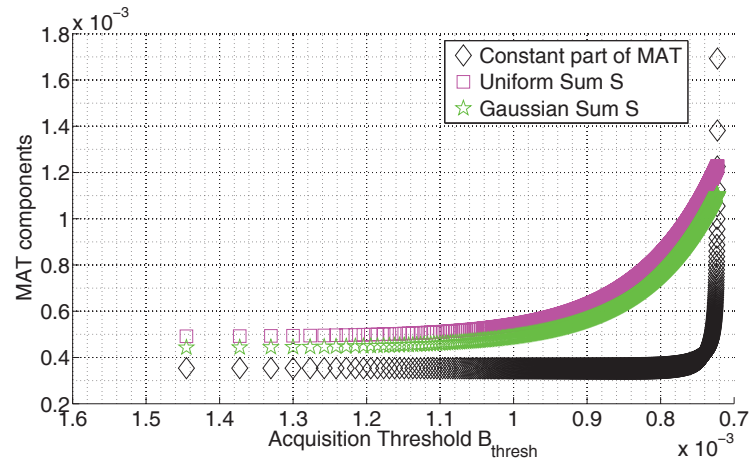
Figure A.11: Comparison of the constant component in the MAT to the sum S components (uniform and Gaussian) vs acquisition threshold for a P2P acquisition engine with a C/N_0 of 30 dB-Hz.

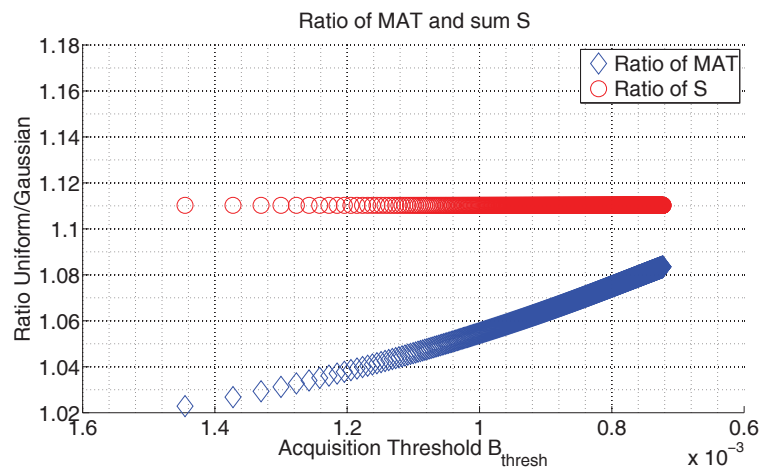**Figure A.12:** Ratio of the uniform and Gaussian sum components as well as their corresponding pMAT with a C/N_0 of 30 dB-Hz.

233

search space as well as a new search order is modelled based on a Gaussian probability distribution of P2P aiding errors.

Appendix B

Mean acquisition time of GNSS peer-to-peer networks

As previously mentioned, the acquisition engine is the most critical block within a GNSS receiver as all subsequent blocks in the receiver chain depend on it. To that end, the P2P architecture is studied again in this appendix, where nearby peers share an additional GNSS aiding information, that is the CNR together with estimates of the code delay, and Doppler frequency. As previously noted, this results in a reduction of the search space over which the CAF is evaluated but also helps to initialize the correct integration time a-priori. The performance improvement in terms of MAT as a result of the P2P setting is tested against the standard acquisition engine in a comprehensive way. Indeed, the MAT of a standard acquisition engine is compared to that of a P2P engine with a thorough investigation of several search strategies including the serial, MAX and MAX/TC with or without verification. The best strategy yielding the optimum MAT is chosen for each acquisition engine.

The innovative aspect in the MAT study presented in this appendix lies in considering the aforementioned three search strategies in light of the P2P context coupled with a verification procedure; a double-dwell time detection in the form of an M over N detector. The impact of this detector declaring the signal present if M out of N tests are positive is also examined by comparing it to a single-dwell time detector where the verification process is nonexistent. The use of a verification process is justified according to the penalty time and the optimum acquisition threshold. It is worth mentioning

that at the time of writing this thesis, almost all literature on the computation of the MAT was either focused on the standard serial search TC criterion [28], [29], a MAX criterion [30] or a hybrid MAX/TC criterion [31]. All these strategies do not show any particular interest in the potential aidings received by a P2P network as in [12] where simulations are performed to assess the MAT using a serial search in the context of a P2P setting.

In this section, closed form expressions of the MAT relative to the MAX and MAX/TC criterion with or without verification procedure are derived and used to perform significant comparisons of a standard acquisition engine with respect to various versions of a P2P acquisition engine. In these comparisons, maximum search strategies are adopted for a standard acquisition engine with a typically large search space, whereas a serial search strategy is most appropriate for the P2P acquisition where the search space is reduced significantly. Moreover, the analysis of the MAT is carried out under weak and strong signal conditions and the P2P architecture benefits are demonstrated using a combination of code delay, Doppler frequency aiding and CNR aiding.

B.1 Acquisition and probabilities

B.1.1 Acquisition systems

In the following, a serial P2P ACQ engine is used and compared to a standard acquisition engine which uses maximum search strategies. In a serial search, it is assumed that the CAF is evaluated or scanned in a starting cell and compared to an ACQ threshold. If the signal is declared present in the cell, the search process is stopped. If the signal is declared absent in that cell, the search continues by moving to the next cell, evaluating the CAF on that cell and applying the detection process cell after cell. For maximum search strategies, the CAF is evaluated in the whole search space in parallel and then the decision is made based on the maximum value of the CAF or the maximum value that passes the ACQ threshold. The MAT for all search strategies is computed assuming that the search continues indefinitely until the signal is declared present in a particular cell. In such a setting, the concept of probability of detection and false alarm is fundamental in evaluating any acquisition time.

B.1.2   Cell and system probabilities

Cell and system probabilities are essentially the major cornerstones in the study of the MAT. Indeed, system probabilities, cell probabilities or even both are used in the expression of the MAT depending on the search and detection strategy. Cell probabilities are typically used in a serial search but also in a MAX and MAX/TC search whenever coupled with a double-dwell time detector. While a single-dwell time detector performs no verification, a double-dwell time detector performs a verification procedure on a single cell where the received SIS is believed to be present.

B.1.2.1   Cell probabilities

Two hypotheses are defined over each cell, H_0 where the chosen cell is called an H_0 cell and does not correspond to the right code delay and Doppler frequency alignment of the received SIS ($P_{fa} + P_{cr} = 1$) and H_1 where the chosen cell is called an H_1 cell and does correspond to the right alignment ($P_d + P_{md} = 1$). P_{fa} is the cell false alarm probability, P_{cr} is the cell probability of correct rejection, P_d is the cell probability of detection and P_{md} is the cell missed detection probability. Coherent integrations are considered herein, and the CAF envelope is evaluated as $R = I^2 + Q^2$ (non-normalized summation of the in-phase and quadrature phase signal at the output of the correlators). The cell and system probabilities expressions can be found in [64]. Moreover, a double-dwell time detector is considered and represented by an M over N detector. The detection outcome being the result of a Bernoulli process with probabilities P_d and P_{fa}, the cell probabilities of detection and false alarm in verification mode can be written as:

$$P_{d,v} = \sum_{m=M}^{N} \binom{N}{m} P_d{}^m (1 - P_d)^{N-m} \tag{B.1}$$

and

$$P_{fa,v} = \sum_{m=M}^{N} \binom{N}{m} P_{fa}^m (1 - P_{fa})^{N-m} \tag{B.2}$$

B.1.2.2   System probabilities

System probabilities are used when assessing the MAT in the context of a MAX or a MAX/TC search but also in a serial search whenever coupled with a double-dwell time detector. In this case, two different hypotheses are defined. Hypothesis H_2 applies to

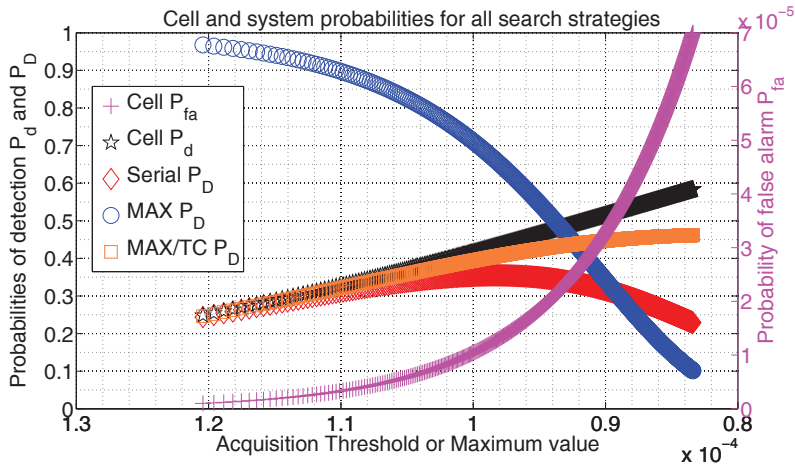## B. MEAN ACQUISITION TIME OF GNSS PEER-TO-PEER NETWORKS

Figure B.1: Cell and system probabilities vs ACQ threshold B for various search strategies and a C/N_0 equal to 40 dB-Hz

the case where the PRN code that is being tested is actually present in the received signal, and so the probability rule is $P_{FA}^p + P_{MD} + P_D = 1$ where P_{FA}^p is the system probability of false alarm in presence of the PRN code in question. This probability is also called system probability of error P_E. Hypothesis H_3 on the other hand, is defined when the PRN code that is being tested is absent in the received signal, and the system probability rule becomes $P_{FA}^a + P_{CR} = 1$ where P_{FA}^a is the system probability of false alarm in absence of the PRN code in question. System probabilities summarize the detection situation in an efficient way and as such the system P_D is plotted in conjunction with the MAT in the following figures. In fact, even if the MAT for a serial search depends on cell probabilities P_{fa} and P_d, it is the system P_D that summarizes the behaviour of both cell probabilities. The behaviour in terms of system P_D of all search strategies is summarized in Figure B.1 where all curves are plotted vs the ACQ threshold except the pure MAX search which is plotted against the possible maximum value in the CAF. It is intuitive to see that the system P_{MD} and P_{FA}^a do not depend on the search strategy as both entail the search of all cells in any case. However, P_D and $P_{FA}^p = P_E$ highly depend on the search and detection strategy [64] and are derived in terms of the acquisition threshold B, the number of cells N_c in the search space, and the two parameters α and σ relating to signal and noise power. For a serial as well as MAX/TC search strategy, where the verification is performed over a

single cell, the overall system probabilities are defined as the product of the system and cell probabilities, i.e. overall probability of detection is $P_{D,v}^{Tot} = P_D P_{d,v}$ and overall probability of error as $P_{E,v}^{Tot} = P_E P_{fa,v}$. However, the system probabilities are expressed differently for a pure MAX search strategy where the maximum is chosen without comparing it to a threshold. In fact, in this case, the P_{MD} is null ($P_D + P_E = 1$), and the verification process is performed by searching the whole search space all over again (instead of just a single cell) and verifying that the maximum corresponds to the same cell in consideration for at least M times:

$$P_{D,v}^{Tot} = P_D P_{D,v} = P_D \sum_{m=M}^{N} \binom{N}{m} P_D^m (1 - P_D)^{N-m} \tag{B.3}$$

and

$$P_{E,v}^{Tot} = P_E P_{E,v} = P_E \sum_{m=M}^{N} \binom{N}{m} P_E^m (1 - P_E)^{N-m}. \tag{B.4}$$

B.2 MAT analysis using different search strategies

In this section, the MAT is introduced considering different search strategies, from serial to pure MAX as well as MAX/TC coupled with a double-dwell time detector, i.e. the M over N detector as a verification process. In the literature, a robust procedure to compute the MAT is mainly based on the pgf. The whole procedure to derive the MAT is presented for a MAX/TC with single as well as double-dwell time verification and all search strategies are confronted amongst themselves. Moreover, MAT curves as a function of the acquisition threshold are used to justify the presence or absence of a verification procedure.

B.2.1 Serial search

The serial single-dwell time search strategy consists in evaluating the CAF in a specific cell and serially moving to the next cells in some specified direction and order until the H_1 cell is found, i.e. the cell which holds the correct PRN code, Doppler frequency and code delay. A double-dwell time detector on the other hand, applies a further verification procedure only on the cells where it is believed that the signal is present. This cell can be both an H_0 or an H_1 cell. A decision flow graph diagram has long been adopted in the literature as a procedure to determine the MAT for a serial search

B. MEAN ACQUISITION TIME OF GNSS PEER-TO-PEER NETWORKS

[28]. This method defines the gain functions that govern the transition from one cell to another, in order derive the system pgf $P_{ACQ}(z)$. The MAT is then given by the flow graph technique described as:

$$E[T_A] = \left| \frac{d}{dz} P_{ACQ}(z) \right|_{z=1}. \tag{B.5}$$

The time needed to test a single cell is denoted as T_c seconds, and is a function of the integration time T_i. Moreover, after a false acquisition, the system goes through a penalty time T_p in the tracking stage which is usually taken to be the tracking transient time (around 500 ms) of a successful tracking operation. In general, two options are considered for setting the starting cell; uniform probability where the probability to start from a specific cell is the same for all cells, and worst-case probability which is equivalent to scanning the H_1 cell in the last position [29]. A similar analysis is performed for a double-dwell time detector in [30] and the corresponding MAT is found in Table B.1 where T_v is the duration of the verification procedure. The expressions in Table B.1 are used to compute the MAT for a range of ACQ thresholds. The curves in Figure B.2 are obtained, which yield an interesting comparison of the performance of a single and double-dwell time detectors in terms of MAT. In fact, examining a single-dwell time detector, the behavior of both curves relative to a uniform and worst-case probability search orders are similar; the MAT decreases with increasing P_D, continues decreasing with decreasing P_D and then unexpectedly starts increasing. This is the point where the term $T_p P_{fa}$ starts weighing on the system with respect to T_c (see expression in Table B.1). It is worth mentioning that the curves are plotted assuming a range of increasing cell P_{fa} values, to which corresponds a decreasing acquisition threshold values and consequently an increasing and a decreasing system P_D as can be seen from Figure B.1. In fact, as the acquisition threshold is decreased, a higher P_{fa} is expected together with a lower system P_D. Consequently, in the absence of a penalty time due to wrong acquisition, a decreasing MAT is expected corresponding to an increasing P_d and a decreasing P_D and B. Hence, at times where $T_p P_{fa}$ is relatively low with respect to T_c, the MAT and P_D as well as B are directly proportional. The opposite is true for relatively high values of $T_p P_{fa}$ with respect to T_c, corresponding to $P_D < 0.1$ considered as the inflection point of the curve relative to the uniform probability search order with $T_p = 500$ ms. In this portion of the plot, the MAT of a single-dwell time detector and P_D are inversely proportional. This inflection point
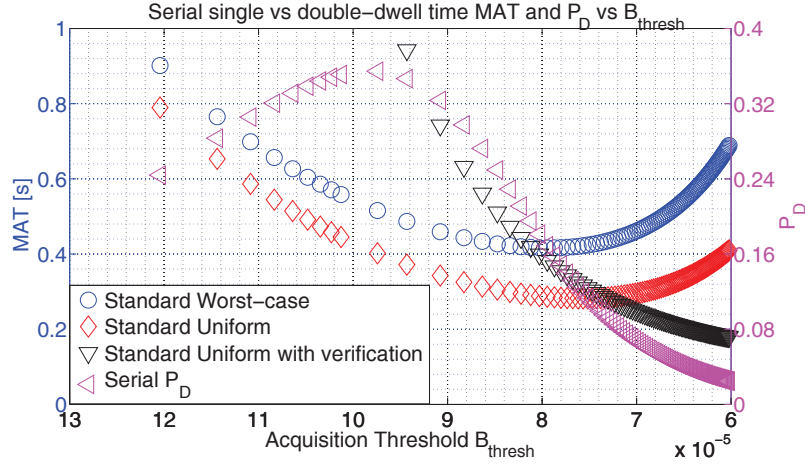
Figure B.2: MAT vs ACQ threshold indicating the range of the ACQ threshold for which a verification procedure is justified.

moves to the left as the penalty time increases. In this way, depending on the penalty time, the use of a double-dwell time detector can be justified or not over a single dwell time detector with no verification. In this case, the use of a double-dwell time detector is not justified for the optimum value of $B = B_{opt}$, i.e. the value of B yielding the minimum MAT. In fact, it can be seen that for $B = B_{opt}$ the curve with verification results in a slightly higher MAT value than that corresponding to a single-dwell time. Conversely, beyond the inflection point, the MAT of a double-dwell time detector and P_D are directly proportional. This is of course due to the fact that when adopting a verification process, even if the acquisition threshold is not set correctly, it is less likely that the CAF crosses the threshold over a wrong cell for several consecutive instances, and so the penalty time is avoided more often and does not weigh on the system for high P_{fa}. In fact, looking at Table B.1, the term $T_p P_{fa}$ becomes $T_p P_{fa} P_{fa,v}$, making it harder to be relatively bigger than T_c and $T_v P_{fa}$.

B.2.2 MAX search

The pure maximum or MAX search strategy is based on the evaluation of the whole search space and picking the cell which holds the maximum value of the CAF without comparing it to a threshold. This strategy is particularly useful in a P2P environment where an indication of the presence of a particular SIS by nearby peers is most likely

Table B.1: MAT of serial search strategies

Strategy	MAT
Serial **Worst-case**	$\dfrac{T_c}{P_d} + \dfrac{(N_c - 1)}{P_d}(T_c + T_p P_{fa})$
Serial **Uniform**	$\dfrac{T_c}{P_d} + \left(\dfrac{N_c - 1}{2}\right)\left(\dfrac{2 - P_d}{P_d}\right)(T_c + T_p P_{fa})$
Serial **uniform with** **verification**	$\dfrac{T_c + T_v P_d}{P_d P_{d,v}} + \left(\dfrac{N_c - 1}{2}\right) \cdot$ $\left(\dfrac{2 - P_d P_{d,v}}{P_d P_{d,v}}\right)(T_c + T_v P_{fa} + T_p P_{fa} P_{fav})$

to be true. In this case, there is no need to compare the maximum CAF value against a threshold. To derive an expression of the MAT, a similar approach as presented for the serial search can be followed, drawing a flow graph diagram and deriving the corresponding pgf [30] to deduce the MAT with (B.5). This is a fairly simple procedure for a single-dwell time detector, whereas the situation gets more complex for a double-dwell time detector. In fact, as previously mentioned in Section B.1.2.2, the verification process for a MAX approach consists in computing the whole search space at least N times, instead of just a single cell. Assuming that T_s is the time spent to evaluate the whole CAF, the pMAT for a MAX approach are reported in Table B.2 where $P_{MD,v} = 1 - P_D(1 - P_{D,v})$. As expected, the double-dwell time detector expression is simplified to that of the single-dwell detector when $P_{D,v}$ and $P_{E,v}$ are replaced by 1 and $T_v = 0$ for a single-dwell time detector.

B.2.3 MAX/TC search

Unlike the MAX search, the MAX/TC search picks the cell relative to the maximum of the CAF and compares its value to the acquisition threshold. In this case, the flow
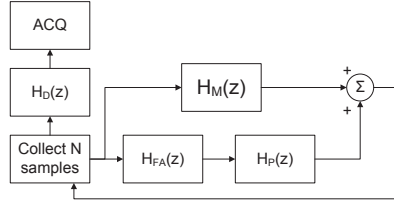
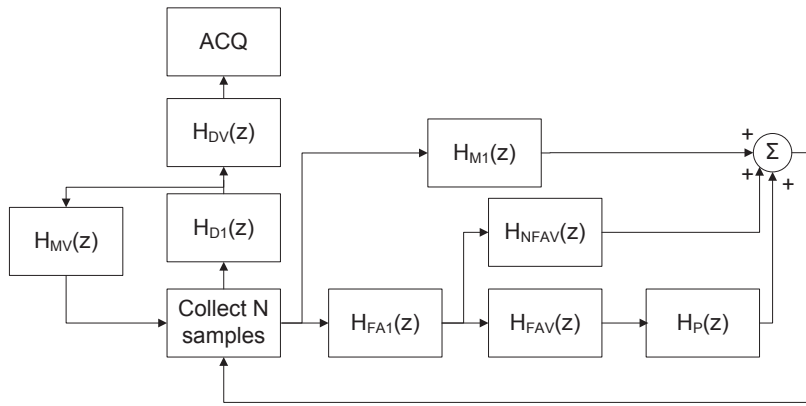**Figure B.3:** MAX/TC single-dwell time acquisition flow graph.

Figure B.4: MAX/TC double-dwell time acquisition flow graph.

graph diagram includes an additional gain function $H_M(z)$ representing the case of an immediate missed detection as seen in Figure B.3.

The gain functions here are $H_D(z) = P_D z^{T_s}$, $H_0(z) = H_{FA}(z) H_p(z) = P_E z^{(T_s+T_p)}$, $H_M(z) = P_{MD} z^{T_s}$ and $H_{0M}(z) = H_M(z) + H_{FA}(z) H_p(z)$ with a pgf of $P_{ACQ}(z) = H_D(z)/(1 - H_{0M}(z))$. As in the serial search, the verification procedure is applied when the SIS is declared present, such that the acquisition flow graph for the double-dwell time detector is represented in Figure B.4. In this case, the gain functions are written as $H_D(z) = H_{D1}(z)H_{DV}(z) = P_D P_{d,v} z^{(T_s+T_v)}$, $H_M(z) = H_{D1}(z)H_{MV}(z) = P_D(1 - P_{d,v}) z^{(T_s+T_v)}$, and $H_{0M}(z) = H_{M1}(z) + H_{FA1}(z)[H_{NFAV}(z) + H_{FAV}(z)H_p(z)] = P_{MD} z^{T_s} + P_E(1 - P_{fa,v}) z^{(T_s+T_v)} + P_E P_{fa,v} z^{(T_s+T_v+T_p)}$ and the pgf is equal to $P_{ACQ}(z) = H_D(z)/([1 - H_{0M}(z)][1 - H_M(z)])$. The MAT for the single-dwell time detector as reported in Table B.2 is obtained after substituting its pgf into (B.5). In a similar way,

Table B.2: MAT of MAX and MAX/TC search strategies

MAX	$\dfrac{T_s}{P_D} + \left(\dfrac{1 - P_D}{P_D}\right) T_p$
MAX/TC	$T_s + T_s \dfrac{P_{MD}}{P_D} + (T_s + T_p)\dfrac{P_E}{P_D}$
MAX with verification	$\dfrac{P_{D,v}}{P_{MD,v}}\left[\dfrac{T_s + T_v}{P_{MD,v}} + \dfrac{1 - P_D}{P_D}\left(T_s + T_v + T_p P_{E,v}\right)\right]$
MAX/TC with verification	(B.6)

the MAT of a double-dwell time detector is obtained:

$$\begin{aligned}
\bar{T}_A &= \frac{P_{d,v}}{P_D P_{MD,v}}\left[T_s P_{MD} + P_E(T_s + T_v + T_p P_{fa,v})\right] \\
&+ (T_s + T_v)\left(\frac{P_{d,v}}{P_{MD,v}} + \frac{P_D P_{d,v}(1 - P_{d,v})}{P_{MD,v}^2}\right)
\end{aligned} \tag{B.6}$$

Figure B.5 shows the MAT curves vs ACQ threshold relative to all three considered search strategies with a single-dwell time detector. In summary, for the minimum MAT values of each strategy, the MAX/TC together with the MAX strategy is the most performant strategy. The MAT values relative to both maximum search strategies are less than those of the serial search by almost two orders of magnitude and so maximum search strategies will be used in the next section as the optimum search strategy for a standard ACQ engine.

B.3 Performance comparison of standard and P2P acquisition engines

In this section, standard and special P2P acquisition engines are confronted in terms of MAT. To guarantee a fair comparison, a MAX or MAX/TC approach is selected for the standard ACQ engine whereas a serial search is opted for the P2P ACQ engine
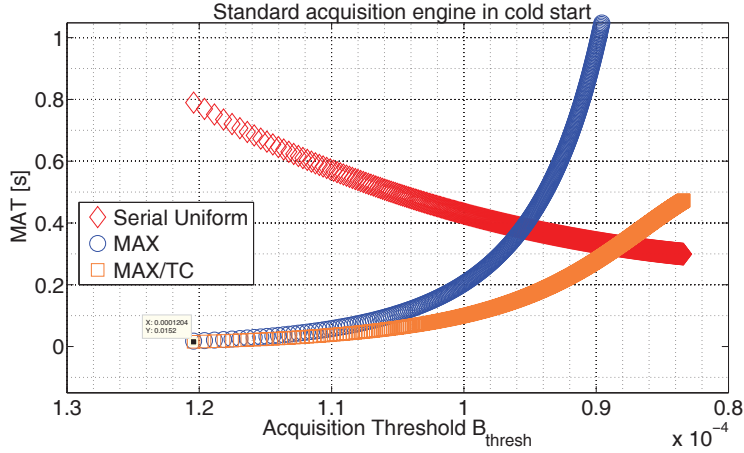
Figure B.5: Performance comparison of all three search strategies using a standard ACQ engine and a single-dwell time detector with a $C/N_0 = 40$ dB-Hz and a $T_i = 1$ ms.

such that the best possible search is adopted for each case. In fact, a serial search is usually the best choice for a P2P architecture where the search space is reduced to a few cells over which the CAF is computed. This is done by providing code delay and Doppler frequency aiding with a certain accuracy, depending on the topology and synchronization of the network [65]. Moreover, an innovative acquisition approach, particularly favorable for weak signal conditions, is explored in a P2P setting where the coherent integration time is set on the basis of the estimated C/N_0 value made available by the P2P network [65].

B.3.1 Standard MAX search vs P2P serial search

For a time and frequency synchronized network to less than a µs and less than a tenth of Hertz, the P2P architecture offers an aiding which can reduce the search space to a few chips and most likely a single Doppler step. The number of these candidate cells depends on the code delay and Doppler frequency step used in the acquisition engine. The code delay step is usually half a chip whereas the Doppler frequency step is set empirically to $\Delta f = 2/(3T_i)$. The MAT of a P2P network is computed using the same system probabilities as those computed for a standard ACQ engine. This is because although only L candidate cells are scanned in the P2P case, the remaining cells are nontheless existent and associated with a certain cell P_{fa} and P_d. The only difference in

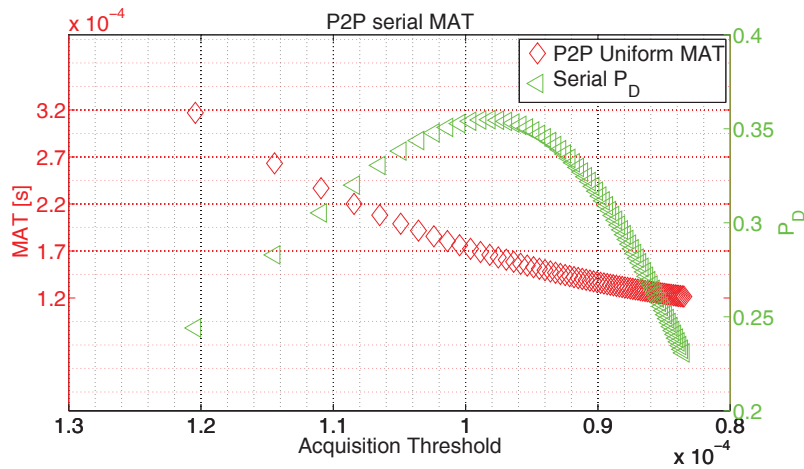## B. MEAN ACQUISITION TIME OF GNSS PEER-TO-PEER NETWORKS

Figure B.6: MAT and system P_D performance of a P2P engine using a serial search with a $C/N_0 = 40$ dB-Hz and a $T_i = 1$ ms.

the MAT is the scanning time, and to account for that, N_c is replaced by L the number of P2P candidate cells in the serial case, and T_s is replaced by the corresponding P2P reduced search space scanning time for the MAX and MAX/TC case. Assuming a C/N_0 equal to 40 dB-Hz, Figure B.7 compares the performance of a standard ACQ engine (shown individually in Figure B.6) using a MAX search to that of a P2P ACQ engine using a serial search. The plot also shows on the right vertical axis, the system P_D for each search strategy. First and foremost, the optimum MAT of a P2P serial search is one order of magnitude lower than that of a standard MAX search (0.17 ms compared to 17.5 ms). Moreover, the MAT curve of the MAX search grows exponentially with decreasing maximum CAF value compared to the decreasing MAT of the P2P serial search with decreasing acquisition threshold as shown in Figure B.6. In fact, when the maximum value of the CAF is not so high, the MAT of a MAX search increases drastically together with a decreasing system P_D. This suggests that the MAX search is not a controllable environment and can yield very bad results. Similarly, Figure B.8 compares the performance of a standard ACQ engine using a MAX/TC search to that of a P2P serial search engine. The superior performance conveyed by the P2P architecture is demonstrated in this figure as well.

246

Figure B.7: Performance of a P2P ACQ engine using a serial search compared to a standard ACQ engine using a MAX search with a $C/N_0 = 40$ dB-Hz and a $T_i = 1$ ms.
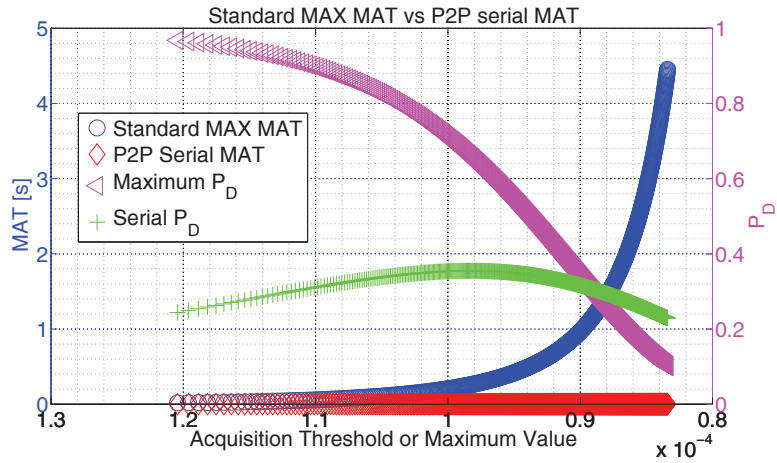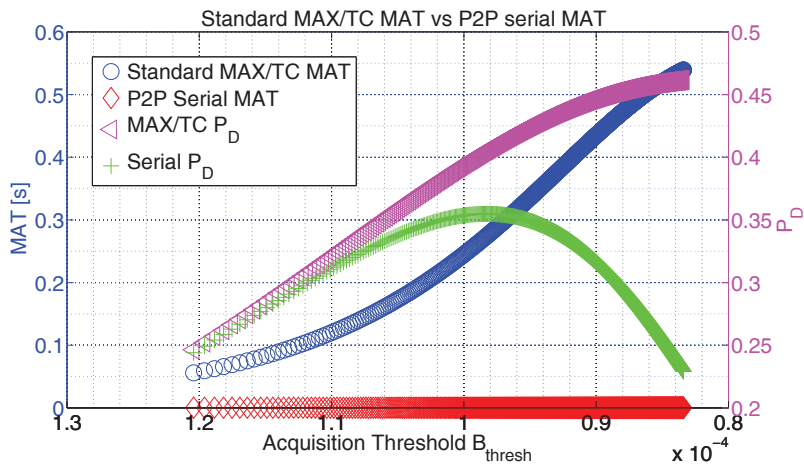

Figure B.8: Performance of a P2P ACQ engine using a serial search compared to a standard ACQ engine using a MAX/TC search with a $C/N_0 = 40$ dB-Hz and a $T_i = 1$ ms.

B.3.2   Standard MAX search vs CNR aided P2P serial search

A new P2P acquisition approach is analyzed herein, based on the C/N_0 aiding information shared by nearby peers. This approach consists in setting the integration time as a function of the weighted P2P CNR, the acquisition metric SNR_c, noncoherent accumulations L, and the receiver bandwidth B with the aim of decreasing the MAT [65]. Using the equation reported in [65], the coherent integration time with no noncoherent accumulations can be obtained. In fact, $T_i = 25$ ms for a $C/N_0 = 20$ dB-Hz, an acquisition metric of 4 dB, an IF bandwidth B of 1.023 MHz and a sampling frequency of 2.046 MHz. In order to assess the impact of the integration time setting according to the CNR, it is worth checking the MAT performance in weak signal conditions.
For a CNR of 20 dB-Hz and a typical $T_i = 1$ ms, the MAT of both strategies, standard MAX/TC and a P2P serial ACQ engine, significantly increases with a highly unreliable system P_D of the order of 10^{-5}. Using this motivation, for the same $C/N_0 = 20$ dB-Hz, Figure B.9 shows the extent by which the CNR aided P2P acquisition is more performant in terms of MAT than the usual P2P engine with no integration time setting. It is worth noting how this figure summarizes the relationship between the system P_D and the MAT. Indeed, as the system P_D relative to the usual P2P acquisition is much lower than that of the CNR aided P2P acquisition, its corresponding MAT is higher by an order of magnitude. Both curves show the same decreasing trend, which can be interpreted, following the same line of thought presented in Section B.2.1, i.e. the fact that $T_p P_{fa}$ is relatively small with respect to T_c.

B.4   Conclusion

The MAT of a serial, MAX and MAX/TC search strategies with or without verification have been analyzed herein, and closed form expressions have been derived using the acquisition flow graph technique. The performance improvement contributed by a P2P network in terms of MAT is thoroughly investigated by exploring two types of aiding, code delay and Doppler frequency aiding from one side and CNR from another. It is shown that together with the aiding available to reduce the search space, exploiting the CNR aiding to set an appropriate integration time, further reduces the MAT especially in weak signal conditions.

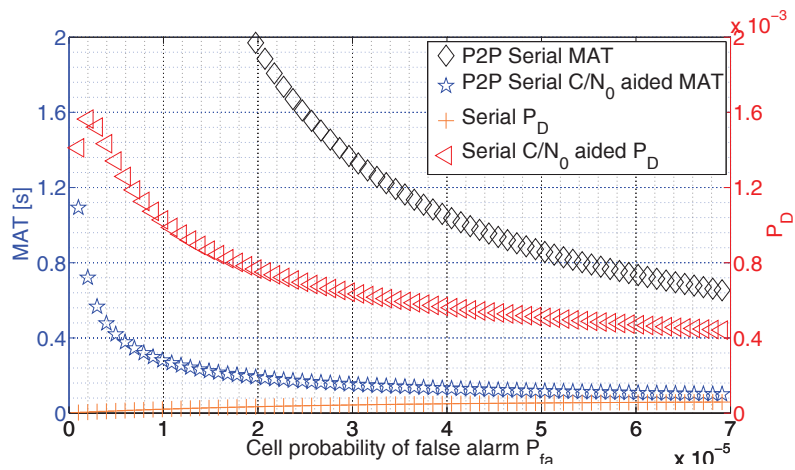**Figure B.9:** Performance of a P2P serial ACQ engine in both cases: $T_i = 1$ ms and an integration time set according to the P2P C/N_0 aiding, i.e. $T_i = 25$ ms with a $C/N_0 = 20$ dB-Hz.

B. MEAN ACQUISITION TIME OF GNSS PEER-TO-PEER NETWORKS

References

[1] J. Bao and Y. Tsui. *Fundamentals of Global Positioning System Receivers*. John Wiley & Sons, Hoboken, New Jersey, second edition, 2005. 1

[2] S. Gleason and D. Gebre-Egziabher. *GNSS applications and methods*. Artech House, Boston, Massachussets, 2009. 1, 4, 5, 36, 77, 80, 81

[3] F. Van Diggelen. **High Sensitivity: Indoor GPS**. In *A-GPS: Assisted GPS, GNSS, and SBAS*, pages 133–139. Artech House, 2009. 3, 26

[4] P.A. Roncagliolo and J.G. Garcia. **High Dynamics and False Lock Resistant GNSS Carrier Tracking Loops**. In *Proceedings of the 20th International Technical Meeting of the Satellite Division of The Institute of Navigation (ION GNSS 2007)*, pages 2364 – 2375, Fort Worth, TX, September 2007. 4, 49, 74, 100, 102

[5] P.L. Kazemi. *Development of New Filter and Tracking Schemes for Weak GPS Signal Tracking*. PhD thesis, Department of Geomatics Engineering, University of Calgary, Canada, May 2010. 4, 49, 96, 97, 100, 101, 102

[6] J.T. Curran. *Weak Signal Digital GNSS Tracking Algorithms*. PhD thesis, Department of Electrical and Electronic Engineering, National University of Ireland, Cork, Ireland, November 2010. 4, 25, 45, 55, 61, 62, 66, 72, 74

[7] P.W. Ward. **A Design Technique to Remove the Correlation Ambiguity in Binary Offset Carrier (BOC) Spread Spectrum Signals**. In *Proceedings of the 59th Annual Meeting of The Institute of Navigation and CIGTF 22nd Guidance Test Symposium*, pages 146–155, Albuquerque, NM, June 2003. 5, 81

[8] P.A. BELLO AND R.L. FANTE. **Code Tracking Performance for Novel Un-ambiguous M-Code Time Discriminators**. In *Proceedings of the 2005 National Technical Meeting of The Institute of Navigation*, pages 293 – 298, San Diego, CA, January 2005. 5, 81

[9] O. JULIEN. *Design of Galileo L1F receiver tracking loops*. PhD thesis, Department of Geomatics Engineering, University of Calgary, Canada, July 2005. 5, 68, 81, 176, 183

[10] M.S. HODGART, P.D. BLUNT, AND M. UNWIN. **Double estimator a new receiver principle for tracking BOC signals**. *Inside GNSS*, 2008. 5, 81, 86

[11] A. JOVANOVIC, C. MONGREDIEN, Y. TAWK, C. BOTTERON, AND P.A. FARINE. **Two-step Galileo E1 CBOC tracking algorithm: when reliability and robustness are keys!** *International Journal of Navigation and Observation*, **12**(135401):14, Jan. 2012. 5, 81, 82, 83

[12] N. KASSABIAN AND L. LO PRESTI. **Technique for MAT Analysis and Performance Assessment of P2P Acquisition Engines**. In *Position, Location and Navigation Symposium (PLANS) conference, Myrtle Beach, South California, US*, April 2012. 8, 236

[13] N. KASSABIAN AND L. LO PRESTI. **Mean acquisition time of GNSS peer-to-peer networks**. In *Localization and GNSS (ICL-GNSS), 2012 International Conference on*, June 2012. 8, 213

[14] G. FALCO, N. KASSABIAN, AND L. LO PRESTI. **First Joint GPS/IOV-PFM Galileo PVT estimation using carrier phase measurements**. In *European Navigation Conference*, April 2012. 8

[15] N. KASSABIAN, G. FALCO, AND L. LO PRESTI. **A flight in the Piedmont region for water surface detection and altimetry experimentation**. In *IEEE International Geoscience and Remote Sensing Symposium IGARSS*, July 2012. 9

[16] N. KASSABIAN AND Y. MORTON. **Galileo Tracking Performance Under Ionosphere Scintillation**. In *Fourth International Colloquium on Scientific and Fundamental Aspects of the Galileo Programme*, December 2013. 9

[17] N. Kassabian and Y. Morton. **Extended Integration Time for Galileo Tracking Robustness Under Ionosphere Scintillation**. In *IEEE/ION Position, Location and Navigation Symposium (PLANS) conference, Monterey, California, US*, May 2014. 9

[18] N. Kassabian and Y. Morton. **Assessment of Galileo OS Signals and Tracking Algorithms During Equatorial Ionosphere Scintillation**. unpublished. 9

[19] J.M. Juan Zornoza J. Sanz Subirana and M. Hernandez-Pajares. *GNSS data Processing, Vol. I: Fundamentals and Algorithms*. ESA Communications, Noordwijk, the Netherlands, 2013. 12, 13

[20] B.R. Rao, W. Kunysz, R. Fante, and K. McDonald. *GPS/GNSS Antennas*. Artech House, Incorporated, 2012. 12

[21] **European GNSS (Galileo) Open Service Signal In Space Interface Control Document (SIS ICD)**. Technical report, Brussels, February 2010. 16, 17, 18, 21, 22, 24, 30, 173

[22] T.E. Humphreys, M.L. Psiaki, J.C. Hinks, B.W. O'Hanlon, and P.M. Kintner Jr. **Simulating Ionosphere-Induced Scintillation for Testing GPS Receiver Phase Tracking Loops**. *IEEE Journal of Selected Topics in Signal Processing*, **3**(4), 2009. 24, 33

[23] A. J. Van Dierendonck. **GPS Receivers**. In W.P. Bradford and J.J. Spilker Jr., editors, *Global positioning systems: Theory and Applications Volume I*, pages 378–394. AIAA, 1996. 25, 27, 58

[24] V.F. Kroupa. *Phase Lock Loops and Frequency Synthesis*. John Wiley & Sons, Ltd, Chichester, UK, 2003. 26, 43, 46

[25] M.S. Sharawi, D.N. Aloi, and D.M. Akos. **GPS C/N_0 estimation in the presence of interference and limited quantization levels**. *Aerospace and Electronic Systems, IEEE Transactions on*, **43**(1):227–238, January 2007. 26

REFERENCES

[26] A. J. Van Dierendonck, J. Klobuchar, and Q. Hua. **Ionospheric Scintillation Monitoring Using Commercial Single Frequency C/A Code Receivers**. In *Proceedings of ION GPS-93*, pages 1333 – 1342, Salt Lake City, UT, September 1993. 33

[27] F. Niu. *Performance of GPS Signal Observables Detrending Methods for Ionosphere Scintillation Studies*. Master's thesis, Department of Electrical and Computer Engineering, Miami University, Oxford, Ohio, December 2012. 35

[28] J.K. Holmes. *Spread Spectrum Systems For GNSS And Wireless Communications*. Artech House, Boston, London, 2007. 39, 218, 236, 240

[29] A. Polydoros and C. Weber. **A Unified Approach to Serial Search Spread-Spectrum Code Acquisition - Part I: General Theory**. *IEEE Transactions on communications*, **32**(5):542–549, May,1984. 39, 219, 236, 240

[30] J.H.J. Iinatti. **On the threshold setting principles in code acquisition of DS-SS signals**. *IEEE journal on selected areas in communications*, **18**(1):62–72, January,2000. 39, 236, 240, 242

[31] G.E. Corazza. **On the MAX-TC Criterion for Code Acquisition and Its Application to DS-SSMA Systems**. *IEEE Transactions on communications*, **44**(9):1173–1182, September,1996. 39, 236

[32] A.G. Dempster N.C. Shivaramaiah and C. Rizos. **Exploiting the Secondary Codes to Improve Signal Acquisition Performance in Galileo Receivers**. In *Proceedings of the 21st International Technical Meeting of the Satellite Division of The Institute of Navigation (ION GNSS 2008)*, pages 1497 – 1506, Savannah, GA, September 2008. 40

[33] P.W. Ward. **Performance comparisons between FLL, PLL and a novel FLL-assisted-PLL carrier tracking loop under RF interference conditions**. In *Proceedings of the 11th International Technical Meeting of the Satellite Division of The Institute of Navigation (ION GPS 1998)*, pages 783–795, Nashville, TN, September 1998. 41

[34] A. RAZAVI, D. GEBRE-EGZIABHER, AND D.M. AKOS. **Carrier Loop Architectures for Tracking Weak GPS Signals**. *Aerospace and Electronic Systems, IEEE Transactions on*, **44**(2), April, 2008. 41

[35] F.M. GARDNER. *Phaselock Techniques*. John Wiley & Sons, Inc., Hoboken, NJ, USA, third edition, 2005. 46, 96, 98

[36] S.A. STEPHENS AND J.B. THOMAS. **Controlled-root formulation for digital phase-locked loops**. *Aerospace and Electronic Systems, IEEE Transactions on*, **31**(1):78–95, Jan. 1995. 49, 96

[37] E.D. KAPLAN, editor. *Understanding GPS: Principles and Applications*. Artech House, Boston, London, 1996. 49, 55, 58, 59, 68, 69, 72, 77, 96, 97, 99

[38] S.C. GUPTA. **On optimum digital phase-locked loops**. *Communication Technology, IEEE Transactions on*, **16**(2):340–344, April 1968. 49, 96, 100, 101

[39] A.J. VITERBI. *Principles of Coherent Communication*. MacGraw-Hill, New York, 1966. 56

[40] W. HAGMANN AND J. HABERMANN. **On the phase error distribution of an open loop phase estimator**. In *Communications, 1988. ICC '88. Digital Technology - Spanning the Universe. Conference Record., IEEE International Conference on*, pages 1031–1037 vol.2, Philadelphia, PA, USA, June 1988. 62

[41] R.L. FANTE. **Unambiguous Tracker for GPS Binary-Offset-Carrier Signals**. In *Proceedings of the 59th Annual Meeting of The Institute of Navigation and CIGTF 22nd Guidance Test Symposium*, pages 141–145, Albuquerque, NM, June 2003. 81

[42] K. BORRE, D.M. AKOS, N. BERTELSEN, P. RINDER, AND S.H. JENSEN. *A Software-defined GPS and Galileo Receiver. A Single-frequency Approach*. Applied and Numerical Harmonic Analysis. Boston, MA: Birkhuser, 2007. 96, 98

[43] W. DUNHAM. *Journey through genius: the great theorems of mathematics*. Wiley, New York, 1990. 116

REFERENCES

[44] A.V. Oppenheim and S.W. Alan with S.H. Nawab. *Signals and Systems, 2nd edition.* Prentice Hall Inc., New Jersey, 1983. 117

[45] K. Ogata. *Modern Control Engineering.* Prentice Hall Inc., Upper Saddle River, New Jersey, third edition, 2003. 133

[46] J.W. Betz. **Design and Performance of Code Tracking for the GPS M Code Signal**. In *Proceedings of the 13th International Technical Meeting of the Satellite Division of The Institute of Navigation (ION GPS 2000)*, pages 2140 – 2150, Salt Palace Convention Center, Salt Lake City, UT, September 2000. 173

[47] P.W. Ward, J.W. Betz, and C.J. Hegarty. **GPS satellite signal acquisition and tracking**. In E.D. Kaplan, editor, *Understanding GPS: Principles and Applications*, pages 119–208. Artech House, 1996. 176, 225

[48] J.W. Betz and K.R. Kolodziejski. **Generalized Theory of Code Tracking with an Early-Late Discriminator Part I: Lower Bound and Coherent Processing**. *Aerospace and Electronic Systems, IEEE Transactions on*, **45**(4):1538–1556, 2009. 182

[49] J.W. Betz and K.R. Kolodziejski. **Generalized Theory of Code Tracking with an Early-Late Discriminator Part II: Noncoherent Processing and Numerical Results**. *Aerospace and Electronic Systems, IEEE Transactions on*, **45**(4):1557–1564, 2009. 182

[50] X. Mao and Y. Morton. **GNSS Receiver Carrier Tracking Loop Impact on Ionosphere Scintillation Signal C/N0 and Carrier Phase Estimation**. In *Proceedings of ION GNSS+*, Nashville, TN, September 2013. 196

[51] M. Martin-Neira. **A passive reflectometry and interferometry system (PARIS): application to ocean altimetry**. *ESA Journal*, (17):331–355, 1993. 203

[52] A.K. Fung, C. Zuffada, and C. Y. Hsieh. **Incoherent Bistatic Scattering from the Sea Surface at L-Band**. *IEEE Transactions on Geoscience and Remote Sensing*, **39**(5):1006–1012, May 2001. 203

[53] C. ZUFFADA, T. ELFOUHAILY, AND S. LOWE. **Deriving Near-Surface Wind Vector With Ocean Reflected GPS Signals: Simulations And Measurements**. *submitted for publication in Remote Sensing of the Environment*, March 2001. 203

[54] S.T. LOWE, C. ZUFFADA, Y. CHAO, P. KROGER, J.L. LABRECQUE, AND L.E. YOUNG. **5-cm-Precision aircraft ocean altimetry using GPS reflections**. *Geophysical research letters*, **29**(10):13–1, 2002. 203

[55] R. N. TREUHAFT, S. T. LOWE, C. ZUFFADA, AND Y. CHAO. **2-cm GPS altimetry over Crater Lake**. *Geophysical research letters*, **28**(23):4343–4346, 2001. 203

[56] R. HATCH. **Dynamic Differential GPS at the Centimeter Level**. In *Proceedings of the Fourth International Geodetic Symposium on Satellite Positioning, Las Cruces, NM*, April 1986. 203

[57] P.J.G. TEUNISSEN. **The least-squares ambiguity decorrelation adjustment: a method for fast GPS integer ambiguity estimation**. *Journal of Geodesy*, **70**(1-2):65–82, November 1995. 203

[58] A. HELM. **Ground-based GPS altimetry with the L1 OpenGPS receiver using carrier phase-delay observations of reflected GPS signals**. Scientific technical report STR08/10, Potsdam : Deutsches GeoForschungsZentrum GFZ, October 2008. 204

[59] D. MASTERS, P. AXELRAD, AND S. KATZBERG. **Initial results of land-reflected GPS bistatic radar measurements in SMEX02**. *Elsevier Inc. Remote Sensing of Environment*, **92**:507–520, May 2004. 204

[60] S. ESTERHUIZEN. *The Design, Construction, and Testing of a Modular GPS Bistatic Radar Software Receiver for Small Platforms*. Master's thesis, Department of Electrical and Computer Engineering, 2006. 204

[61] P. MISRA AND P. ENGE. *Global Positioning System: Signals, Measurements, and Performance*. Ganga-Jamuna Press, second edition, 2006. 205

REFERENCES

[62] M. Caparrini, L. Ruffini, and G. Ruffini. **PARFAIT: GNSS-R coastal altimetry**. In *Workshop on Oceanography with GNSS Reflections, Barcelona, Spain*, November 2003. 205

[63] S. Gleason, S. Lowe, and V. Zavorotny. **GNSS Applications and Methods**. In S. Gleason and D.G. Egziabher, editors, *Remote sensing using bistatic GNSS reflections*, pages 399–436. Artech House, Nordwood, MA, 2009. 206

[64] D. Borio, L. Camoriano, and L. Lo Presti. **Impact of GPS Acquisition on Decision Probabilities**. *Aerospace and Electronic Systems, IEEE Transactions on*, **44**(3), July, 2008. 215, 216, 237, 238

[65] D. Margaria, N. Kassabian, L. Lo Presti, and J. Samson. **A New Peer-to-Peer Aided Acquisition Approach Exploiting C/N0 aiding**. In *5th ESA Workshop on Satellite Navigation Technologies, ESTEC, Noordwijk, The Netherlands*, 8-10 December 2010. 224, 245, 248